Ion-Drag Electrohydrodynamic Micropumps

A Numerical and Experimental Study
Of
Ion-Drag Electrohydrodynamic Micropumps

By

Syed Mohammed Hasnain, BEng. Hons.

A Thesis

Submitted to the School of Graduate Studies

in Partial Fulfillment of the Requirements

for the Degree

Masters of Applied Science

McMaster University

MASTER of APPLIED SCIENCE (2010)
(Mechanical Engineering)

McMaster University
Hamilton, Ontario

TITLE: A Numerical and Experimental Study of Ion-Drag Electrohydrodynamic Micropumps

AUTHOR: Syed Mohammed Hasnain, BEng. Hons. (University College London, UK)

SUPERVISORS: Dr. Chan Y. Ching and Dr. Ravi Selvanagapathy

NUMBER OF PAGES: xi, 139

Abstract

The objectives of this work are (i) to develop a numerical model for electrohydrodynamic micropumps, (ii) to investigate the effect of using a conductive agent in the working fluid to enhance the pump performance and (iii) to investigate the use of pulse voltage on EHD micropumps.

A numerical model was developed that incorporates a charge model at the emitter electrode that is coherent to the electric field. The model results were found to be in good agreement with previous experimental results. A parametric study was performed to investigate the effect of the channel height and multi-stage spacing on the pump performance. Reducing the channel height reduced the flow rate but increased the pressure head, while increasing the multi-stage spacing improved the pump performance.

The effect of using conductive agents in the working fluid was investigated using Ferrocene in HFE-7100. The Ferrocene was found to significantly improve the pump performance. However, at high voltages, the pressure could not be sustained for long periods of time. The effect of an applied pulse voltage on the performance of the micropumps was studied. A maximum pressure 3512 Pa was achieved at an applied pulse voltage between 500 V to 800V, pulse repetition rate of 5 Hz, and duty cycle of 60%.

Acknowledgement:

I would first like to express my gratefulness to God Al-Mighty for making me amongst the privileged to pursue further education. I would like to thank my supervisor and co-supervisor, Dr. Chan Y. Ching and Dr. Ravi Selvanagapathy, not only for their guidance and support throughout this research project, but also for giving me the opportunity to learn from them.

I would like to also thank Dr. Jen-Shih Chang for sharing his expertise in the Electrohydrodynamic field. I would also like to thank Doris Stefanovic, Zhillin Peng, and Graham Pearson for helping me develop crucial microfabrication skills for my experimental investigations.

I am also grateful to my friends and colleagues in Center of Advanced Micro-Electro Fluidics (CAMEF), and Thermal Management Research Laboratory (TMRL) for their support, and for creating an enjoyable environment to work in.

I would like to express my gratitude to Asmaa Maloul for her continuous support in achieving my goals, and her undivided belief that I can excel them. Without her support completing my research would not be possible. I would also like to thank my family. In particular I would like to thank my parents, for their love, patience, support; making my journeys easier at times of great difficulties, and also giving me the strength to not give up.

I would like to dedicate this work to my friend and father, Syed Qamar Hasnain Naqvi, the biggest believer in me and the biggest investor in my life and happiness.

Table of Contents:

List of Figures:

List of Tables:

Chapter 1: Introduction

The rapid development of micro and nano fabrication techniques has provided the technology to develop complex microelectronic circuits. This is most evident in computer processors where on a single die billions of micro-transistors can be placed. However, this has resulted in high heat flux densities, and one key challenge for this sector is to dissipate this energy to maintain the die temperature below its design point (Borkar, 1999). Conventional cooling mechanisms used at the macro-scale are not able to provide adequate heat removal at the micro-scale (Raj, 2005). Therefore, there is a need to develop novel micro-scale thermal management solutions. Microchannel heat sinks have shown significant potential, and have been shown to remove up to 1 kW/cm^2 (Jiang et. al, 2001). The main difficulty in implementing microchannel heat sinks is the lack of a micropump that can be integrated within the electronic package.

Micropumps have applications in diverse fields such as in micromixers, chemical analysis systems, and in biomedical applications (Becker et. al, 1997; Nguyen, 2008; Woolley et. al., 1996). They can be broadly classified into two categories: (i) displacement and (ii) dynamic (Laser and Santiago, 2004). In the displacement type, a periodically moving surface is the source of the pressure generation. In most reciprocating displacement micropumps a diaphragm with fixed edges provides the motion for the working fluid. Typical materials for diaphragms at the micro-scale are silicon, glass, and metals (Gerlach and Wurmus, 1995; Rapp et. al., 1994; Yun et. al., 2002). The second category is dynamic where the driving force is provided without the use of any moving part or surface. Examples of these are Magnetohydrodynamic (MHD) and Electrohydrodynamic (EHD) micropumps where magnetic or electric fields are used to generate a body force within the flow domain. An EHD micropump holds several advantages over other existing technologies since it has no moving parts and the fluid flow can be controlled through the applied electric potential. Ion-drag EHD micropumps typically comprise of a series of electrode pairs embedded into the bottom wall of a microchannel. A high voltage is applied to the electrode pairs which results in the injection of charges into the fluid domain. The charges then cause certain fluid particles local to the electric field to be ionized and move in the direction of the electric field. The friction caused by the motion of these ionized particles and neutral particles cause a bulk fluid motion, known as the ion-drag effect.

1.1 Research Objectives

The overall objective of this research is to investigate the mechanisms in Ion-Drag EHD and develop more robust micropumps. Some of the key issues that limit the performance of EHD micropumps are taken into consideration. The limitations of existing design configurations are evaluated. The specific objectives of this research are:

i. To develop a numerical model for EHD micropumps that can be used to optimize the pump configuration.
ii. To investigate the use of conductive agent doped into working fluids for the micropumps.
iii. To investigate the effects of an applied pulse voltage on the performance of EHD micropumps.

1.2 Outline of Thesis

The thesis is divided into six chapters, including the introduction. The background literature on EHD pumps is provided in Chapter 2. This includes a review of the governing equations, and also recent technological development of the pump. The numerical model development is presented in Chapter 3. The model validation and parametric studies are also included in this chapter. A mathematical model is introduced to predict current based on the magnitude and gradient of the electric field at the electrodes. The microfabrication process for the micropumps is discussed in Chapter 4, along with the selection of the conductive agent for the working fluid. The experimental results are presented and discussed in Chapter 5. Finally, the conclusions that are drawn from the numerical and experimental work along with recommendations for future work are presented in Chapter 6.

Chapter 2: EHD Background

2.1 Introduction

Electrohydrodynamics (EHD) refers to the study of the interaction between electrically charged species and fluid flow. Polarized charges present in the fluid medium experience a force due to the applied electric field. This force is then transmitted to neutral liquid molecules. However, the motion of these charges also has an effect on the electric field, which in turn affects the liquid body force. This makes electrohydrodynamic pumping a complex phenomenon to understand as both fluid flow and the electrostatics are dependent on each other. EHD pumping can be placed into three categories, distinguished by the way charges are introduced into the fluid medium. The three categories are induction, conduction, and injection. This chapter reviews the underlying mechanism for each category, with the main focus being on injection EHD. A literature review is presented in the latter part of this chapter, describing the existing work in this field.

EHD pumping technique is attractive as it does not require any mechanical parts to generate a flow. EHD has particular uniqueness as not only does it use electric fields to control fluid motion, but essentially any non-polar fluids (i.e. alcohol, air, etc.) can be used as dielectrics and it is applicable to multi-phase flows.

The principle mechanism underlying EHD induction is when charges are introduced into an inhomogeneous liquid and the body force is transmitted through the charge interaction with the electric field (Hardt, 2007). Non-uniform properties in the working fluid can arise due to a temperature gradient. Conductivity of the liquid is affected by temperature as ionic mobility is inversely proportional to viscosity. Temperature also affects the disassociation rate of neutral molecules which would cause electrical permittivity gradients to be present in the fluid. Usually travelling waves provide a temperature gradient through joule heating. However, recently micropumps with externally applied temperature gradients of up to -2 K/μm to 2 K/μm have been realized (Felten et. al., 2006). Figure 2.1 shows a schematic of a EHD induction micropump with a travelling potential wave and a externally applied temperature field (T_X).

Conduction EHD phenomena is found to exist in weak electric field regime (less than 10^7 V m^{-1}). The introduction of current into the domain depends on the rate of dissociation and recombination of molecules that subsequently produce ions:

$$A^+B^- \underset{K_r}{\overset{K_d}{\Leftrightarrow}} A^+ + B^-$$

where A^+,B^-, $K_{d,}$ and K_{r} represent the positive ions, negative ions, disassociation rate, and recombination rate respectively. As the electric field exceeds a certain threshold (10^5 V/m), a layer is formed near the electrode where the dissociation rate becomes faster than the recombination rate. The layers are charged and are of opposite polarity to the layer found at the adjacent electrodes. The force that is generated from these layers produces the fluid motion. Even though the presence of these charged layers is very local and the bulk of the fluid remains neutral, different electrode designs have been investigated to enhance the body force transmitted to the fluid. One design of conduction EHD pump that was investigated is shown in figure 2.2 (Jeong and Seyed-Yagoobi, 2002). It can be seen that the voltage source electrode is placed into the fluid domain and certain distance from the ground electrode. Hence the electrical body force is transmitted from the centre of the domain to the remaining bulk of the fluid.

Injection or Ion-Drag EHD pumping exists in regimes where a high electric field is imposed on the fluid. When a potential is initially applied between electrode pairs, impurities that maybe present get polarized and move toward the electrodes. This process is short due to the particles becoming neutralized as they approach the electrodes. Charges are then injected into the fluid domain through a corona source, which is primarily at the sharp edges of the electrodes. These charges are unipolar and ionize some of the fluid molecules.

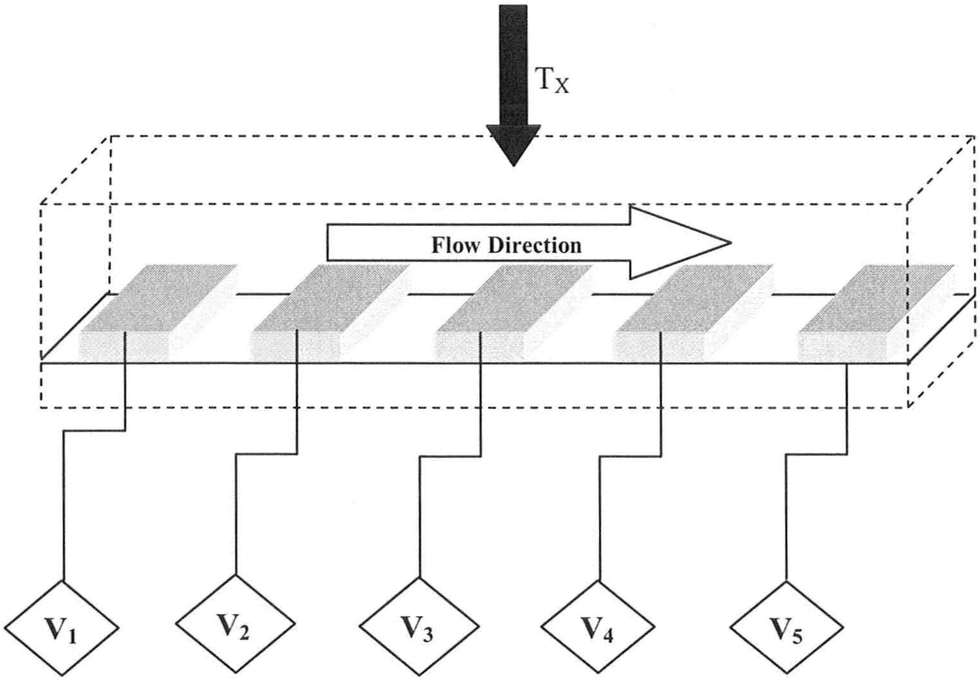

Figure 2.1: Schematic of typical induction EHD pumping at microscale with travelling electrical wave and externally applied temperature field.

Depending on the polarity of the charged molecules they can subsequently move along or against the direction of the electric field and have frictional effect with the remaining fluid molecules. This in turn causes the motion of fluid and the process is known as the Ion-Drag Effect. Figure 2.3 illustrates the charge injection process for a single electrode pair.

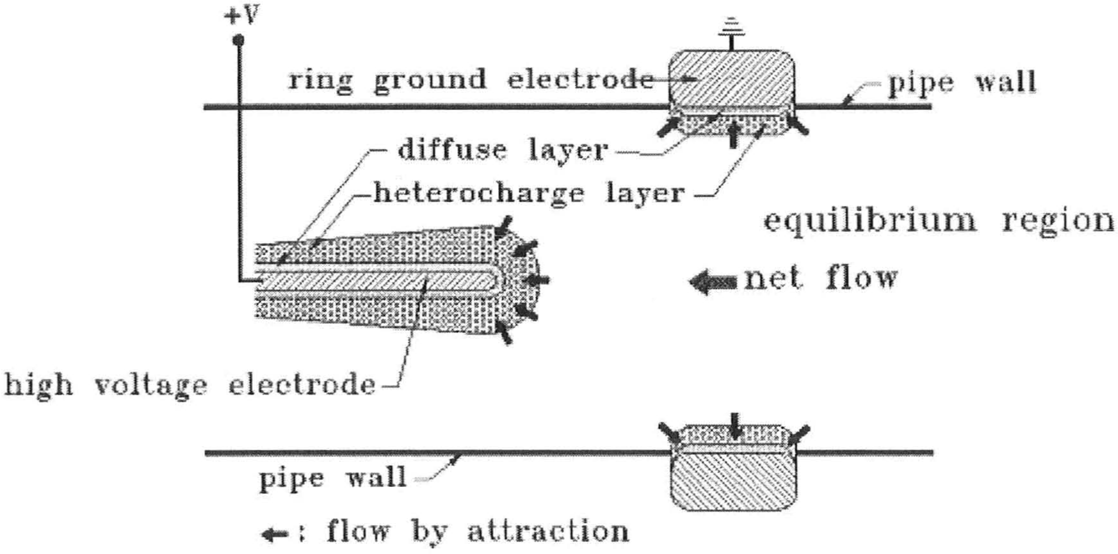

Figure 2.2: Schematic of EHD conduction pump electrode design by Jeong and Yagoobi (2002).

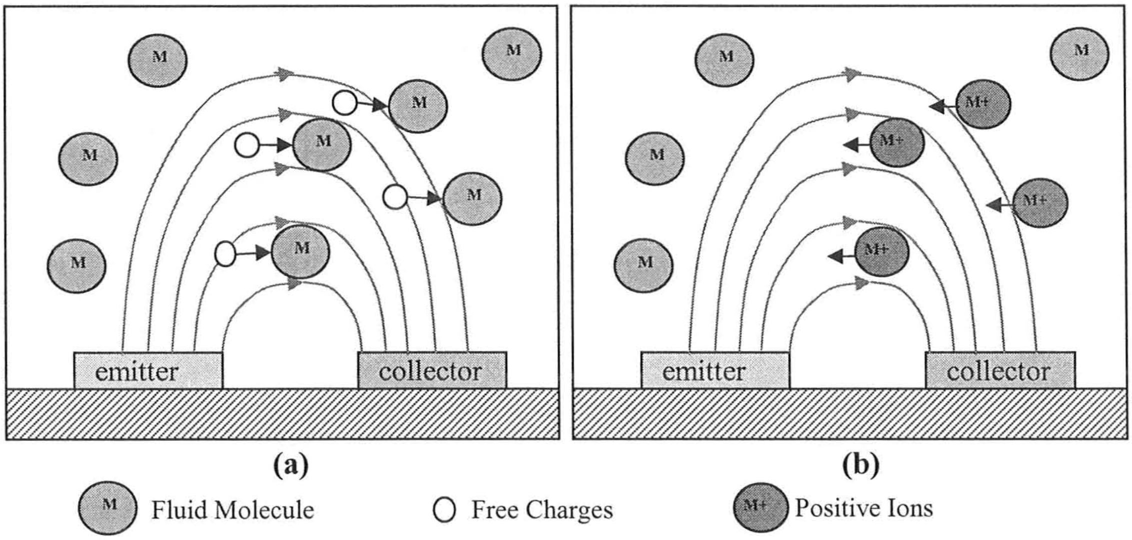

Figure 2.3: Illustration of the Ion-Drag EHD mechanism of (a) Charge Injection (b) Motion of the ionized molecules.

2.2 Governing Equations for Electrohydrodynamics

The governing equations for EHD injection pumping are presented here. The electrostatic and charge equations are presented first through which the electric body force is generated. The body force is incorporated in the fluid governing equation.

The Maxwell equation relation of the curl of a magnetic field (*B*) to the electric field (*E*) and current flux (*J*) is given by:

$$\nabla \times B = \mu_0 J + \mu_0 \varepsilon_0 \frac{\partial E}{\partial t} \qquad \text{[Eq. 2.1]}$$

where μ_0 and ε_0 represents permeability (magnetic constant) and permittivity (electric constant) in free space. There are two distinct limits in the confines of speed of light (*c*) to determine the mechanism of a system. One is known as electroquasistatics where $E > cB$ and the other is called magnetoquasistatics where $E<cB$. To determine the significance of these limits in EHD, the equation is rewritten as (Chang et. al., 1995):

$$\nabla \times B = \mu_0 \sigma E + \mu_0 \varepsilon_0 \frac{\partial E}{\partial t} \qquad \text{[Eq. 2.2]}$$

this is based on the assumption that the working fluid is operating in the ohmic regime where $J=\sigma E$, where σ represents the conductivity of the fluid. Since magnetic fields are determined by motion of charges, then $B \sim \sigma \mu_0 E l$, where l is the characteristic length of the pump. Considering typical systems condition it was found that $E/cB \sim 1/\sigma$. EHD flow deals with fluid of low conductivity (i.e. $\sigma \rightarrow 0$), hence it falls under the electroquasistatics regime. However in the case of Magnetohydrodynamic (MHD) flows it will be considered as magnetostatics as it uses highly conductive fluid to induce the Lorentz force to cause motion.

Neglecting the magnetic field, Maxwell's equation takes the form of Gauss's Law:

$$\nabla . E = \frac{\rho_e}{\varepsilon} \qquad \text{[Eq. 2.3]}$$

where, ρ_e represents charge density and ε is the product of permittivity of free space and the relative permittivity of the working fluid.

Figure 2.4 shows the typical Current-Voltage characteristic that is observed in EHD micropumps. Region I is defined as the Ohmic regime where current increases in a linear manner to the applied voltage. The production of current in this region is mainly caused by the disassociation of impurities and is generally found to occur at low voltages. Region II exists when the applied electric field exceeds 10^5 V/m. In this region ions cannot be generated as fast through disassociation as compared to the rate they are neutralized at the electrode. Hence saturation is observed in the current. Region III is defined as the point where charge injection becomes the dominant source of current production. An exponential rise is observed in the current with increase in voltage. However, as the electric field approaches a magnitude of the order of 10^8 V/m breakdown might occur. Breakdown is also found dependant, on the type of fluid, geometric configuration, and the presence of impurities. The conservation of charge is defined as:

$$\frac{\partial \rho_e}{\partial t} + \nabla.J = \mathbf{0} \qquad \text{[Eq. 2.4]}$$

At low voltages, in the Ohmic regime, the source of charges is primarily through conduction EHD. In this region current flux is defined as:

$$J = \sigma E + \rho_e u \qquad \text{[Eq. 2.5]}$$

where u is the fluid velocity. The first term is due to conduction and the second term is due to convection. At high electric fields, charge injection at the solid-liquid interface becomes the key driving source for the charge motion. If the medium is considered to be highly insulating (i.e. $\sigma \approx 0$), and assuming only unipolar charges are injected then current flux can be defined as:

$$J = \mu_e \rho_e E + \rho_e u - D\nabla.\rho_e \qquad \text{[Eq. 2.6]}$$

where, $\mu_{e,}$ D are known as the ionic mobility, and molecular diffusion coefficient respectively. The three terms in equation 2.6 represent the migration, convection and diffusion of charges.

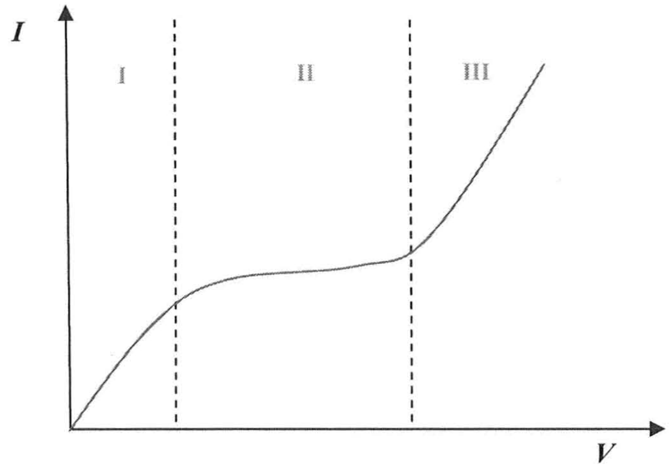

Figure 2.4: Current-Voltage Characteristics in EHD micropumps

The fluid motion is governed by the conservation of mass and momentum and is given by:

$$\frac{\partial \rho}{\partial t} + \nabla . u = 0 \qquad \text{[Eq. 2.8]}$$

$$\rho\left(\frac{\partial \mathbf{u}}{\partial t} + \mathbf{u}.\nabla \mathbf{u}\right) = -\nabla p + \mu \nabla^2 \mathbf{u} + \mathbf{F_e} \qquad \text{[Eq. 2.9]}$$

where, ρ, t, u, p, μ represent the fluid density, time, fluid velocity, pressure, and dynamic viscosity respectively. However, since we are considering only fluid motion at steady state the first term of both equations can be neglected. In equation 2.9, $\boldsymbol{F_e}$ represents the fluid body force that is generated by the electric field and charge density. This term is comprised of three components (Stratton, 1941):

$$\mathbf{F_e} = \rho_e E - \frac{1}{2}E^2\nabla\varepsilon + \frac{1}{2}\nabla\left[E^2\rho\left(\frac{\partial\varepsilon}{\partial\rho}\right)_T\right] \qquad \text{[Eq. 2.10]}$$

The first term represents the electrophoretic force or the Coulomb force. Charges that are introduced into the domain experience a force due to the interaction with the electric field and move along the field lines. Since ρ_e represents the net charge density (i.e. negative and positive), $\rho_e E$ represents the net force acting on the fluid.

The second term is known as dielectrophoretic force and can be expanded as:

$$\frac{1}{2}E^2\nabla\varepsilon = \frac{1}{2}E^2\left(\left(\frac{\partial\varepsilon}{\partial\rho}\right)_T\nabla\rho + \left(\frac{\partial\varepsilon}{\partial T}\right)_\rho\nabla T\right) \qquad \text{[Eq. 2.11]}$$

this force needs to be taken into consideration if electrical permittivity gradients exist in the working fluid. A permittivity gradient would only be present if the working fluid had inhomogeneous properties such as in a two-phase flow or if there is a temperature gradient.

To determine the importance of dieletrophertic force in comparison to the electrophoretic force in the Ion-Drag micropump case the EHD (E_{HD}) and Masuda (Md) numbers are calculated as:

$$E_{HD} = \frac{I_o L^3}{\rho \upsilon^2 \mu_e A} \qquad \text{[Eq. 2.12]}$$

$$Md = \frac{\varepsilon_o E_o{}^2 T_o \left({}^{\partial \varepsilon_r}\!\big/_{\partial T} \right)_\rho L^2}{2\rho \upsilon^2} \qquad \text{[Eq. 2.13]}$$

where, I_o, L, υ, A, T_o, ε_r, and ε_o represent outlet current, characteristic length, kinematic viscosity, surface area of electrode, outlet temperature, relative permittivity, and permittivity of free space. The EHD number represents the Coulomb force over the square of Reynolds number while the Masuda number is the dielectrophoretic force over the square of the Reynolds number. Based on previous experimental works (Kazemi, 2009a; Benetis, 2005) EHD number was found to be 3 orders of magnitude higher than the Masuda number. Therefore, dielectrophoresis is negligible for the Ion-Drag case.

The third term is known as electrostrictive force and is defined as:

$$\frac{1}{2}\nabla\left[E^2 \rho \left(\frac{\partial \varepsilon}{\partial \rho}\right)_T\right] = \nabla\left(\frac{E^2(\varepsilon-\varepsilon_0)(\varepsilon+2\varepsilon_0)}{6\varepsilon_0}\right) \qquad \text{[Eq. 2.14]}$$

this term is important when the fluid being considered is compressible.

2.3 Literature Survey

The concept of pumping dielectric liquids by applying electric fields was proposed as early as the 19th century (Chattock and Walker, 1901). However, the work was theoretical and it wasn't until late 1950's that EHD pumping characteristic was demonstrated (Stuetzer, 1959). Stuetzer developed different models for plane, spherical, and cylindrical electrode configurations that was based upon the "corona wind" theory presented by Chattock. The pressure generation was found proportional to the applied current and inversely proportional to the ion mobility. He observed current and voltage characteristics of the pumps and achieved a maximum pressure of 2 kPa with a needle-cylinder electrode configuration and castor oil as the working fluid.

The work of Stuetzer was further substantiated by Pickard (1963) who derived a correlation between the electric field and pressure generation. Pickard used two flat parallel plane electrodes and under assumption of electrophoresis being the main driving force in single-phase fluid the relation that was found was:

$$P = \frac{9}{8} . \varepsilon . E_o{}^2$$

where E_o is the average electric field between the electrodes. This correlation was found to hold true for both the static and dynamic cases in the experimental investigation.

Melcher (1981) investigated the ion-drag pumping phenomena using continuum electromechanics. He developed the non-dimensionless form of the governing equations for EHD mechanism, and introduced the parameters that affect the efficiency and pressure generation of the pump. The Electric Reynolds number:

$$\mathrm{Re}_e = \frac{\varepsilon u}{\sigma L}$$

where, ε,u,σ, and L represent permittivity, velocity, conductivity, and characteristic length represents a ratio between charge convection by flow and charge relaxation through ohmic conduction.

Crowley et. al.(1990) and Crowley (1980) investigated into the effect of liquid properties such as fluid viscosity, dielectric constant, and ionic mobility on EHD pump performance. A high dielectric constant and low viscosity was found to be important to obtain optimal flow rates. The efficiency of the pump was shown to be improved by using a fluid with low ionic mobility. However, when considering Walden's rule (Bockris and Reddy, 1998) both maximum flow rate and efficiency cannot be achieved simultaneously, as viscosity and mobility are inversely proportional to each other.

The effect of electrode geometry on the pumping performance was investigated by Asano and Yatsuzuka.(1999). A needle-cylinder configuration for ion-drag pumping was used and the work showed the radius of curvature for the needle heads affects the breakdown voltage of the pump. It was found that the performance of the pump improved when the size of the needle was reduced. They also found that there is an optimum number of needles for the pressure generation but this depends also on the diameter of the collector. A maximum pressure head of 2900 Pa was acheived for an applied voltage of 29 kV using Silicone oil as the working fluid. Benetis (2005) experimentally investigated a saw-tooth configuration electrodes and the electrode shape had significant effect on the pump performance. The flow performance with the saw-tooth electrode was better than using planar electrodes. A static pressure of 390 Pa was achieved at 400V using HFE-7100 as the working fluid.

Richter and Sandmaier (1990) were the first to fabricate EHD micropumps that was based on the charge injection principal. They used grid-type electrodes fabricated from silicon with an area of 9 mm^2. The spacing between the electrodes was 350 μm while the silicon had a thickness 35 μm and grid structures had diameter of 30 μm. The fabrication process comprised of photolithography, and chemical etchants. A pressure of 2480 Pa was achieved for an applied electric potential of 700V. The working fluids that were used in this work were acetone, propane, and ethanol.

Ahn and Kim (1998) developed the first ion-drag EHD micropump with planar electrodes on a glass substrate. They used an inter-electrode spacing 100 μm and a multi-stage spacing of 200 μm with 30 stages. A maximum flow rate of 50μm/min was achieved with the pressure and flow rate were proportional to the square of the applied voltage. The effect of inter-electrode and multi-stage spacing on EHD micropumps have also been investigated by Benetis (2005), and Foroughi et al.(2005). Benetis found that smaller inter-electrode spacing gives a better flow rate and pressure generation, as the electric field strength is much stronger for the same applied voltage. However, breakdown occurs at lower potentials when compared to configurations with larger inter-electrode spacing. Increasing the multi-stage spacing causes a reduction in the pressure head due to the decrease in the number of stages to accommodate the pump within the same spatial limits. However, flow rate is improved upon as the adverse interaction between the neighboring electrode pairs is reduced.

Darabi et. al. (2002) also investigated into the effect different electrode shapes have in ion-drag EHD micropumps. He incorporated tooth shape emitter electrodes as well as solder bumps as collectors. In contrast to planar electrode, it was found that the non-planar electrode design improved the pump performance for the same given spacing. The tooth shape electrode achieved a pressure of 500 Pa for an applied voltage of 1000V. The bump electrode achieved the same pressure but at an applied voltage of 500V. Kazemi (2009a) introduced asymmetric electrode configurations where the emitter width was half the width of the collector. A significant enhancement in the EHD performance was achieved with this configuration. Furthermore, Kazemi investigated the effect of 3D electrode configuration by implementing nickel micropillars (2009b). Parameters that were investigated were the inter-elecrode spacing and the span-wise spacing between each micropillar. Using micropillar electrodes showed pressure generation of 2240 Pa with an applied voltage 800V. The working fluid in this case was HFE-7100.

Yang et. al (2004) investigated the durability of EHD micropumps by using Indium-Tin Oxide (ITO) as the electrodes. ITO does not have significant electrolysis effects as Cr/Au due to high oxidation resistance at low voltages, which would cause the electrodes to age. The gap spacing for the electrodes was 80 μm for 20 stages. A maximum flow rate of 356 nl/min was obtained for an applied voltage of 61 V. The effect of the fluid on the durability of the pumps was investigated by Benetis (2005), Bologa et. al (1993), and Malakhov (1999). Bologa et. al. tested the life cycle on Ion-Drag EHD pump with filtered and unfiltered kerosene, transformer oil, and polymethlysiloxane-5 (PMS-5). Filtered liquids showed a gradual deterioration in the pump performance after 200 hours of operation, while non-filtrated liquids showed an immediate deterioration in the perferomance. Malakhov (1999) tested for environmental influences on the pumping performance, using kerosene as the working fluid. It was found that when the experiment was conducted in a controlled environment the pressure head and current was stable. However when exposed to atmospheric conditions, and particulates that are present in air, degradation of the pump performance was substantial as the sedimentations on the electrodes was enhanced. Benetis (2005) conducted a 300 hours service test on different pump configurations. In this duration he observed that the collector electrodes deteriorated and the time for deterioration varied from 1 to 10 hours and depended on the applied voltage. However, in one test significant pressure and current loss was observed after 4 hours while the electrodes were still intact. This suggested that the deterioration could be due to degradation in the working fluid.

The correlation between EHD pump performance to the number of electrode stages was characterized by Castaneda and Yagoobi (1992). Experiments were performed with Doedecylybenzine, Conoco O. S. 260-P industrial oil, kerosene, Texaco 0600 oil. It was found that the pressure generation and current had a linear correlation to the number of stages. The pump configuration was axisymmetrical and comprised of thirteen electrode stages. The inter-electrode and multi-stage spacing used were 8 mm and 15 mm. A maximum flow rate and pressure achieved was 15 cm/s and 40 Pa respectively. The maximum current that was attained was 14 μA.

More recently Chen et. al. (2007) developed Ion-Drag EHD micropumps on a flexible substrate. The substrate material was Paralyene-C which is light-weight, transparent, and mechanically strong (Young's Modulus and Tensile Strength of 400 Kpsi and 10,000 psi), and also biocompatible making the technology attractive for biomedical applications. Saw-tooth electrode configurations were developed onto the substrate through the lift-off fabrication process. The number of stages that were used was 75 and 200, while the inter-electrode and multi-stage spacing was 20 μm and 80 μm. A maximum pressure head 490 Pa was achieved with an applied voltage of 30 Volts while a maximum flow rate of 190 mm/min was observed at 20 volts using Isoproponal (IPA).

The effect of a pulsed voltage on the EHD performance has been investigated by Vasilvech and Rychkov (2006). A three electrode configuration was used where the anode-voltage source was placed in between two ground plates. The spacing between the two ground plates is 4 mm. Voltage amplitudes from 0 to 30 kV were tested and with a frequency of up to 2 kHz. It was found that using smaller amplitudes for the pulse gave optimum pressure at frequency of 400 Hz. When compared to DC voltage it was found that the same pressure head could be achieved at lower voltages through pulsing. Also it was found that up to 400 Hz the efficiency of the pumps reaches a peak level. After 400 Hz the efficiency of the pump declines. The maximum pressure head that was generated in this set up was 1600 Pa and the working liquid was purified transformer oil.

The EHD phenomena has also been used for the pumping of gas. Tsubone et. al. (2008) used air as the working fluid in a non-parallel plate wire configuration. Two configuration were investigated which comprised of a converging, or a diverging exit nozzle. The ground electrodes had a spacing of 8.75 mm from the wire electrode. Applied electric potentials of both negative and positive polarity were tested from 0 to 14 kV. Using voltages of negative polarity showed to give a better discharge current. A maximum velocity of 1.9 m/s and a maximum flow rate of 44 l/min were achieved.

Attempts have also been made into developing numerical models of the EHD mechanism. One of the earliest models was developed by Pasechnik and Ufatov (1989). The model is developed for flat electrodes embedded into a non-conducting wall, and the working fluid being was transformer oil. In this model the electrostrictive force is considered to be primary source for the liquid motion. This is solved for by employing the Green's function. Dernovskii et. al. (2007) developed a numerical model for a wire-plane electrode system. In this model the electrophoretic force is taken into account, and the charges were considered to be frozen into liquid and assumed to follow the streamlines of the fluid flow. This assumption was found to be satisfactory as the electrical Reynolds number was well above 10, which shows charge transport by fluid flow would be more significant. It was found that under the wire electrode, a reduced pressure zone was present while in front of the charged stream it is significantly higher, which results in the formation of a recirculation zone. Darabi and Rhodes(2006) developed a model for Ion-Drag EHD micropumps using a commercial finite element code. In this model, HFE-7100 is used as the working fluid and charge continuity is also accounted for. However, the charge boundary condition at the surface of the electrode is given a specific value since the charge injection process is not well understood at the solid-liquid interface. The domain of the model is a 2D segment of the pump and consists of a single-stage electrode with periodic boundary condition employed to account for the interaction between the neighboring stages. The effect of the channel height, and multi-stage spacing was investigated. It was found that increasing the height causes reduction in the generated static pressure but an increase in the flow rate. This is due to frictional losses being reduced with the increased height hence requiring lower pressure to drive the flow. Increasing the multi-stage gap showed an increase in flow rate up to an optimum level while showing a reduction in pressure generated. The increase in flow was found to be because of reduction in the adverse interaction between the stages and the reduction in pressure was considered to be because of the decrease in the number of stages.

Numerical modeling of the EHD phenomena has also been performed for Gas (Zhao and Adamiak, 2004). The model used a pin-plate configuration and accounts for charge injection due to Corona effects. The charge on the electrodes is derived through Peek's Law, which allows the minimum potential gradient to be determined to achieve

Corona onset. Once this is found the current is assumed to be proportional to the square of the applied voltage, above the Corona value. The minimum applied voltage to achieve onset was found to be 4.625 kV. Other models developed for Gas EHD problems differ primarily in the way charge boundary condition is satisfied, for example using Thompsons (Chang et. al., 2009), or Cooperman's analytic solution (Yamamoto and Sparks, 1986).

Table 2.1 provides a summary of the development of EHD pumps.

Reference	**Electrode Design**	**Electrode Spacing**	**No. of Electrodes/ Electrode Double Spacing**	**Fluid**				**Applied Voltage**	**Max. Pressure Head/Flow Rate**
				Type	**Density (kg/m^3)**	**Ionic Mobility ($m^2/V.s$)**	**Viscosity (mPa.s)**		
Stuetzer (1959)	Spherical and Cylindrical	0.6-10 mm	1/N.A	Kerosense/ Silicon Oil	860/1040	3E-07/35E-07	1.9/130	≤30 kV	2kPa/N.A
Pickard (1963)	Planar	2.5-15 mm	1/N.A	Acetone	780	6.80E-08	0.29	≤10 kV	2 kPa/17 $cm.s^{-1}$
Asano et al. (1999)	Needle-Cylinder	2-8 mm	1 /N.A	Silicon Oil	1040	3.5E-06	130	≤30 kV	2.8 kPa/N.A
Benetis (2005)	Saw-Tooth	10-50 μm	100/20-200 μm	HFE-7100	1480	1.31E-08	0.651	≤500 V	390 Pa/15 $ml.min^{-1}$
Ritcher and Sandamier (1990)	Grid-Type	350 μm	1/N.A	Ethanol	790	1.70E-08	1.20	≤700 V	2.48 kPa/N.A
Ahn and Kim (1998)	Planar	100 μm	30/200 μm	Ethanol	790	1.70E-08	1.20	≤100 V	200 Pa/ 50 $\mu l.min^{-1}$

Table 2.1: Experimental development of Injection EHD pumping

Reference	Electrode Design	Electrode Spacing	No. of Electrodes/ Multi-stage Spacing	Fluid				Applied Voltage	Max. Pressure Head/Flow Rate
				Type	Density (kg/m^3)	Ionic Mobility (m^2/V.s)	Viscosity (mPa.s)		
Darabi et. al. (2002)	Saw-Tooth and Solder bump	50-100 μm	50-95/100-200 μm	HFE-7100	1480	1.31E-08	0.651	≤1 kV	500 Pa/N.A
Kazemi (2009)	Asymmetric and 3D micropillars	40-120μm	100/80-240 μm	HFE-7100	1480	1.31E-08	0.651	≤1 kV	2.48 kPa/N.A
Yang et. al. (2004)	Planar	80 μm	20/80 μm	Ethanol	790	1.70E-08	1.20	≤61 V	N.A/356 nl.min^{-1}
Chen et. al. (2007)	Saw-Tooth	20 μm	80 μm	IPA	786	N.A	1.96	≤30 V	490 Pa/190 mm.min^{-1}
Vasilvech and Rychkov (2006)	Needle-Ring	4 mm	1 /N.A	Purified Transformer Oil	876	N.A	115	≤30 kV	1.6 kPa/N.A
Tsubone et. al. (2008)	Plate-Wire	8.75 mm	1/ N.A	Air	1.2 (Room Temp.)	1.95E-04 (Room Temp.)	0.0178 (Room Temp.)	≤14 kV	N.A/44 l.min^{-1}

Table 2.1: Experimental development of Injection EHD pumping

Conduction pumps

Although conduction EHD has yet to be developed at the micro-scale, it has been established in the macro-scale. One of the earlier works in conduction EHD was reported by Jeong and Yagoobi (2002). The pump configuration comprised of a 1,3, and 5 stages electrodes, with ring-shaped electrodes as ground. The high voltage electrode source consisted of three designs. The designs tested were 3- needles, hollow tube, and multi-tubes. It was found that a multi-tube electrode shape gave a better pressure head than the other designs. The pressure generation with a single pair was found to be 586 Pa for an applied voltage of 20 kV. However better current production was seen from the hollow tube electrodes. Increasing the number electrode pairs proved to improve the pressure and current generation. Durability of the Conduction EHD pump was also tested for applied voltages 10 kV, 15 kV, and 20 kV for 8 hours. It was found that for all the applied voltages the steady- state current was the same and did not degrade significantly. However, the displacement current was seen to be higher for 20 kV. The pressure head was also found to be significantly higher at 20 kV. Pressure was also seen to be consistent for the time duration for all the applied voltages.

Atten and Yagoobi (1999) investigated two types of configurations; one comprising of ring electrodes and the other is needle electrodes. The working fluid was n-hexane and R-123. It was found that using ring-electrodes gave a 5 times the pressure head and double the current than using needle electrodes. It was also found that R-123 gave a better performance than n-hexane.

Feng and Yagoobi (2004) developed an analytical model for conduction EHD. Expressions were developed to capture the profiles of the negative and positive charges in the vicinity of the electrodes. The expressions were based upon the assumption of the thickness of the heterocharge layer. The model was then compared to experimental data retrieved from testing a three pair configuration with perforated disc with holes and ring ground electrodes using R-123. The results were validated for no-flow conditions for applied voltage of 17 kV with reasonable agreement between experimental and model results.

A numerical model for conduction EHD was developed for thin-film liquid in the presence of evaporation (Yazdani and Yagoobi, 2009). The numerical technique employed was based on a finite volume technique. The working fluid that is used for the case is R-123. The research looks at key dimensionless numbers and compares the performance to pressure driven flow for a specific heat flux. It was found that reducing the Peclet number results in a greater rate of evaporation. Other dimensionless numbers that were found to have influence of the heat transfer rate were the EHD number and the Mobility ratio.

Induction EHD:

Induction EHD at the microscale has been realized since the early 90's. Fuhr et. al. (1992) developed an Induction EHD pump with 13 electrodes, with a spacing of 30 μm and a height ranging from 100 to 500 μm. The travelling wave is produced by superimposing four rectangular pulses with a phase delay of 90^0. The amplitudes and frequency that were tested ranged from 20 to 50V and 10 kHz to 30 MHz respectively. Using water as the working fluid it was found that the velocity is proportional to the square of the applied voltage peak. A maximum flow rate of 600 μm/s was acheived for an applied voltage peak of 50V.

Müller et. al. (1993) studied the influence of conductivity on the pumping performance negating convection by introducing microgravity using a MikroBa 5 test system. A 13 electrode configuration was used with a spacing of 35 μm with a height of 50 μm. Square- wave voltages are applied with a phase delay of 90^0, frequency of 1 MHz, and amplitude ranging from 32.5 V to 15 V. Distilled water was used as the working fluid with dissolved KCL to enhance the conductivity. The microgravity period was set to 55 seconds. In this work the flow speed was found to be proportional to the applied voltage by a power of 2.5. The pump restricted the maximum operating voltage to be around 40-45V due to turbulent flow development. Suggested reasons for this is using a high frequency on a working fluid with low conductivity which could have electrolysis effect at higher voltages. A maximum flow speed of 200 μm/s was achieved.

Felten et. al. (2006) developed micro-scale induction EHD that employ temperature fields to create inhomogeneities in the working fluid. Joule heating was considered along with applying external temperature fields using Peltier elements, to generate permittivity gradients. The pump comprised of two glass plates separated by polymer spacers. Both top and bottom glass plates had 12 planar electrodes with a width and spacing of 10 μm between adjacent neighbors. Rectangular waveform voltages of 5-10 V amplitude were used with a phase-shift of 90^0. It was found that using external temperature field enhanced the delivery rate of the pumps. A maximum flow rate of 80 μm/s was achieved with a voltage peak of 8 V and a temperatures difference of 50 K.

2.4 Summary

In this chapter the governing equations are presented for EHD pumping mechanism. The processes through which charges are introduced are defined in three different ways which are (1) Conduction (2) Induction and (3) Injection, are discussed. Electrical equations are presented in terms of Maxwell's Equations, which defines the electric field, and the conservation of charge equations. An understanding of the two Galilean Electromagnetism limits is also presented. The EHD phenomena, which uses fluids with strong dielectric properties is considered to exist in the electroquasistatic regime. The fluid dynamic conservation equations are presented, with the inclusion of the electrical body force. The three different components of the electrical body force are electrophoresis, dielectrophoresis, and electrostrictive. Finally a literature survey is presented, which reviews the technological development of Injection EHD. Induction and Conduction EHD are also briefly reviewd. Some limitations that are associated with the EHD mechanisms are also presented.

Chapter 3: Numerical model and simulations

3.1 Introduction

A mathematical model is presented here for EHD micropumps. The micropump consists of a 100μm high microchannel with planar electrodes placed along the bottom wall. Figure 3.1(a) gives an illustration of an EHD micropump in 3D. The governing equations for the electric field, charge conservation, and fluid flow are solved for simultaneously using a commercially available finite element code (COMSOL Multiphysics). Four different micropump layout that were experimentally investigated by Kazemi et. al. (2009a) is used to develop the numerical model. The geometric parameters are summarized in Table 3.1. Two fundamental electrode configurations were considered: (a) planar symmetric where the widths of the emitter and collector electrodes were the same and (b) planar asymmetric where the width of the collector is half that of the emitter. The pumps are designated S and A to denote the symmetric and asymmetric cases, and the number following denotes the inter-electrode spacing in micrometers. The fluid domain used for the model is a 2D cross-section for the corresponding configurations as the high aspect ratio allows the effect of walls along width of the pump to be neglected.

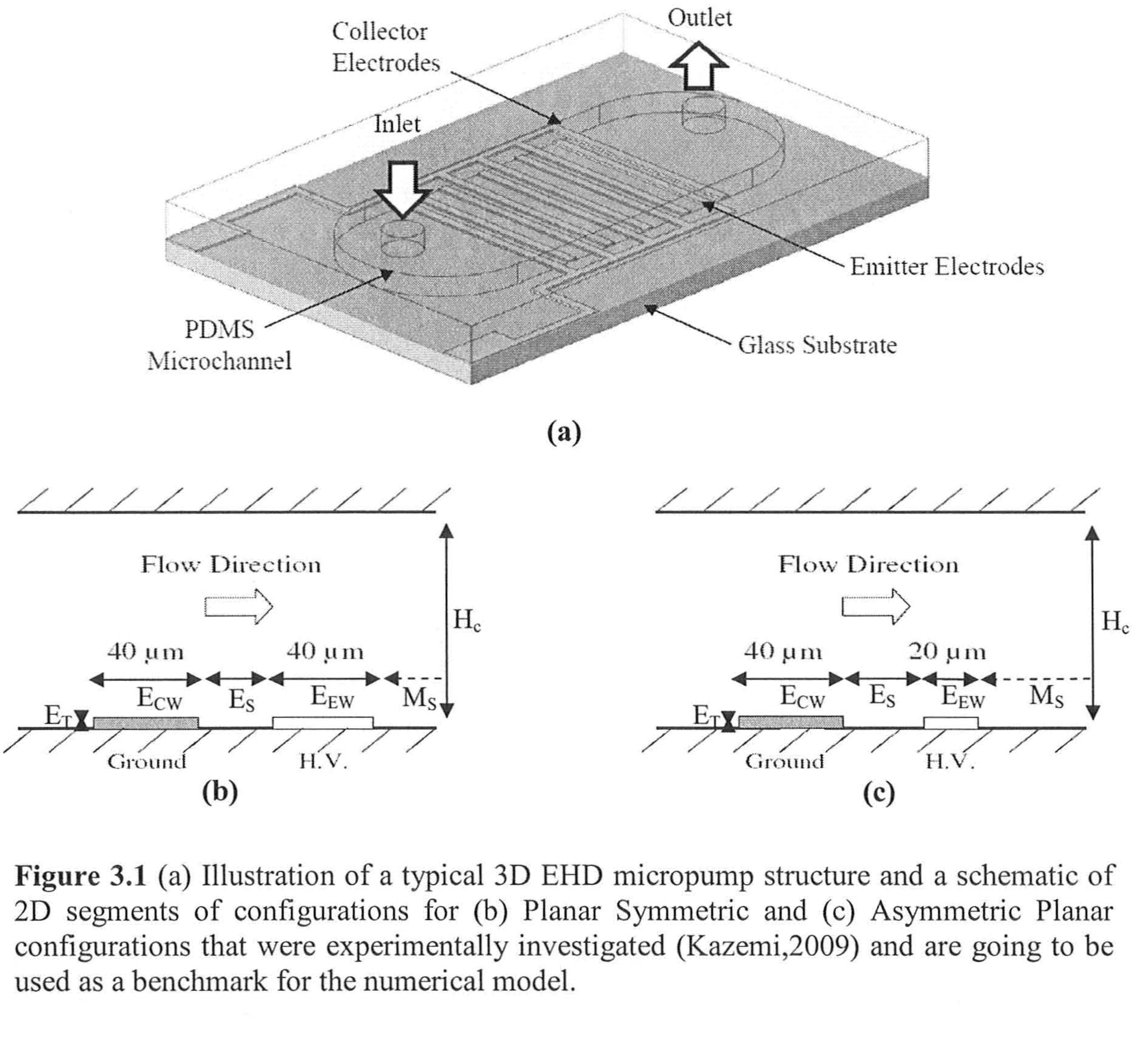

(a)

(b)

(c)

Figure 3.1 (a) Illustration of a typical 3D EHD micropump structure and a schematic of 2D segments of configurations for (b) Planar Symmetric and (c) Asymmetric Planar configurations that were experimentally investigated (Kazemi,2009) and are going to be used as a benchmark for the numerical model.

Pump	**H_C (μm)**	**E_T (μm)**	**E_{EW} (μm)**	**E_{CW} (μm)**	**E_S (μm)**	**M_S (μm)**
S-80	100	0.25	40	40	80	160
S-120	100	0.25	40	40	120	240
A-80	100	0.25	20	40	80	160
A-120	100	0.25	20	40	120	240

Table 3.1: Structural configuration of EHD micropumps that were simulated. The experimental data for comparison for these configuration were obtained from Kazemi (2009).

Schematic of the domain are shown in figure 3.1 (b) and 3.1 (c) with key parameters such as the channel height (H_C), inter-electrode spacing (E_S), electrode width ($\mathrm{E_{CW}}$ and E_{EW}), electrode thickness (E_T), and multi-stage spacing (M_S) which in this instance represents the distance between the neighboring stages.

3.2 Governing Equations and Boundary Conditions:

The equations used to model the EHD phenomena are discussed in this section, along with boundary conditions. The main difficulty is specifying the charge boundary conditions at the emitter and collector electrodes. It is well known that the charge injection process through corona discharge depends on the gradient of the electric field. Thus, a model for the charge distribution is introduced that is coherent with the electric field. Previous models (Darabi and Rhodes 2006; Dernovskii et. al., 2007) that have been developed only consider charges at the electrode to be uniform. However, it is well known that charge injection through corona onset would primarily occur at the sharp corners of the electrodes (Fowler, 1928). The model is validated using the experimental data of Kazemi (2009a).

As discussed in chapter 2, the governing equations for the fluid motion are:

$$\frac{\partial \rho}{\partial t} + \nabla . \mathbf{u} = 0 \qquad \text{[Eq. 3.1]}$$

$$\rho\left(\frac{\partial \mathbf{u}}{\partial t}+\mathbf{u}.\nabla\mathbf{u}\right)=-\nabla p+\mu\nabla^{2}\mathbf{u}+\mathbf{F_e} \qquad \text{[Eq. 3.2]}$$

where, $\mathbf{F_e}$ represents the electrical body force that is generated by the electric field and charge density. The dominant driving force of the liquid is the Coulomb force in an ion-drag pump. The dielectrophoretic and electrostrictive forces, which were mentioned in chapter 2, are neglected. The electrostrictive force can also be neglected as the fluid being considered is incompressible. Dielectrophoresis can be neglected as the fluid is assumed to be operating in single-phase and isotropic conditions. Therefore, no permittivity gradients should exist. In order to determine the Coulomb force within the flow domain, the charge density and electric field distribution needs to be determined:

$$\mathbf{F_e}=\rho_e E \qquad \text{[Eq. 3.3]}$$

The relation between the electric field and charge density is governed by Gauss Law:

$$\nabla.E=\frac{\rho_e}{\varepsilon_r\varepsilon_o} \qquad \text{[Eq. 3.4]}$$

In the absence of magnetic fields, the electric field is related to the electric potential through:

$$E=-\nabla V \qquad \text{[Eq. 3.5]}$$

Substitution of equation 3.5 into 3.4 yields:

$$\nabla^2 V = -\frac{\rho_e}{\varepsilon_r \varepsilon_o} \qquad \text{[Eq. 3.6]}$$

The conservation of charges introduced into the domain is governed by

$$\frac{\partial \rho_e}{\partial t} + \nabla . J = 0 \qquad \text{[Eq. 3.7]}$$

where, J represents the current flux density:

$$J = \mu_e \rho_e E + \rho_e \mathbf{u} - D\nabla \rho_e \qquad \text{[Eq. 3.8]}$$

The first component represents the motion of charges through migration and is considered to be the main driving source of charges in the EHD phenomenon. Under the unipolar charge assumption, this component represents the motion of free ions due to charge injection through the electrodes and is responsible for the ion-drag effect in micropumps. The other components represent electrical conduction of charges, convective, and diffusion charge motion. The convective component is important when it compares in magnitude to the migration term. Initially, this term is neglected to simplify the modeling problem. The assumption is that the flow that is achieved at this scale is laminar (i.e. Re $\leq$400). Based on the pump configuration found in Table 1 and the working fluid properties, which is mentioned in the latter part of this paper, an average flow speed is estimated to be in the order of 10^{-4} m.s^{-1} for Reynolds number of 400. The charge injection process begins at electric fields at the order of 10^{7} V.m^{-1} while the mobility is in the order of 10^{-8} m^{2}.V^{-1}.s^{-1}. Therefore comparing the product of the mobility and electric field to the flow speed it can be seen that the convective term can be neglected. The diffusion component can also be considered negligible due to the high electric field gradients that are present in the domain. The current flux density is related to the current as shown in equation 3.9.

$$I = \int J.dA \qquad \text{[Eq. 3.9]}$$

Replacing the current flux density with only the migration charge current component from equation 8, and assuming a constant ionic mobility yields

$$I = \mu_e \int \rho_e E.dA \qquad \text{[Eq. 3.10]}$$

For the present case, the following are assumed:

1) The charges injected into the domain are unipolar since the applied voltage is steady and of the same polarity.
2) The electrical, physical and chemical properties of the fluid are constant.
3) The surface of the emitter electrode is the only source of charge injection.
4) The flow is considered to be incompressible and in steady-state.
5) The only driving force of the liquid is electrophoresis (i.e. gravitational and other electrical body forces are assumed small compared to this term).

In order to solve the three different sets of equations, three corresponding sets of boundary conditions are required. Of these, the most ill-defined are the boundary conditions for the charge density at the collector and emitter as these are not known a priori. It is, however, known that the charge injection through corona discharge depends on the electric field at the surface. Thus, a field model is developed here for the charge boundary conditions at the electrodes. Three different cases were considered where the local current flux density is assumed proportional to (i) the gradient of the electric field, (ii) the square of the electric field and (ii) the cube of the electric field at the electrode surface. The technique is illustrated below for the case where the local charge density is assumed proportional to the gradient of the electric field at the surface. Firstly, the electric field distribution is estimated by assuming no free charges exist within the domain and solving the Laplace form of Gauss's Law for a given electric potential.

$$\nabla . E = 0 \qquad \text{[Eq. 3.11]}$$

Figure 3.2 shows the typical profile of the electric field at the surface of the emitter electrode. The datum point for the displacement is taken from the left corner of the electrode. The local electric field gradient at the surface is determined from the local electric field (e_n) along the surface at each node (y_n) and the adjacent node (y_{n+1}) normal to the surface (e_{n+1}) as

$$\frac{\partial e}{\partial y} = \frac{e_{n+1} - e_n}{y_{n+1} - y_n} \qquad \text{[Eq. 3.12]}$$

The local current flux (J_n) along the surface is estimated from the known value of total current as:

$$J_n = \left(\frac{I_{\exp}}{AN} \right) \left(\frac{\partial e / \partial y}{E_a / W} \right) \qquad \text{[Eq. 3.13]}$$

where E_a is given by

$$E_a = \frac{W}{A}\int \frac{\partial e}{\partial y}.dA \qquad \text{[Eq. 3.14]}$$

so that the total current is recovered when J_n is integrated over the electrode surface and multiplied by the number of electrodes. Once J_n is determined for each node along the surface, the charge density distribution along the electrode surface (e_n) is determined from

$$J_n = \mu_e \rho_n e_n \qquad \text{[Eq. 3.15]}$$

The corresponding equations for the cases where the local current flux density is assumed proportional to the square and cube of the electric field at the surface are summarized in Table 3.2. The remaining surfaces are set as insulating boundaries. For the electric field equations, the electric potential is specified for the emitter, the collector is grounded and the other surfaces are set as insulating. Periodic conditions are used for the charge density and the electric field at the inlet and outlet of the domain to model the multiple electrode stages. For the fluid flow, the boundary conditions at the inlet and outlet are set to either a no pressure or a no flow condition. This is done in order to determine the maximum pressure or flow rate generation. The remaining surfaces are set as no-slip. The working fluid considered here is Methoxynonafluorobutane (HFE-7100) by $3M^{®}$, with density and viscosity of 1480 kg/m^3 and 6.51 x 10^{-4} Pa.s, and dielectric constant and ionic mobility of 7.39 and 1.31 x 10^{-8} $m^2/V.s$

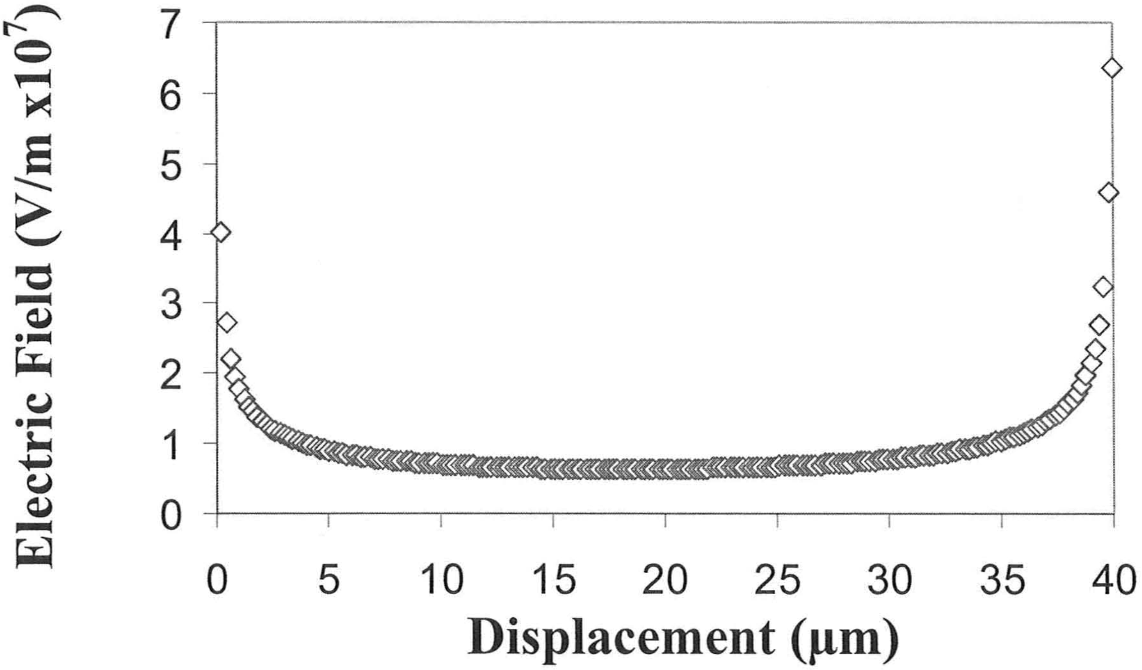

Figure 3.2: Electric field along surface of emitter electrode of S-80 at 600V.

A mesh independence study was performed for the numerical model using the electric field gradient relation for three different mesh structures of 2647, 7852, and 11043 elements. The mesh consists of unstructured triangular elements that are finer, closer to the electrode surface to account for the higher field gradients there. The mesh independent results for S-80 under a no flow and no pressure condition at 400V are shown in Figure 3.3. The mean pressure and flow rate for the grid structures were 10.5 Pa and 0.01093 ml/min, with a standard deviation less than 3% and 5% of the mean values, indicating grid independence.

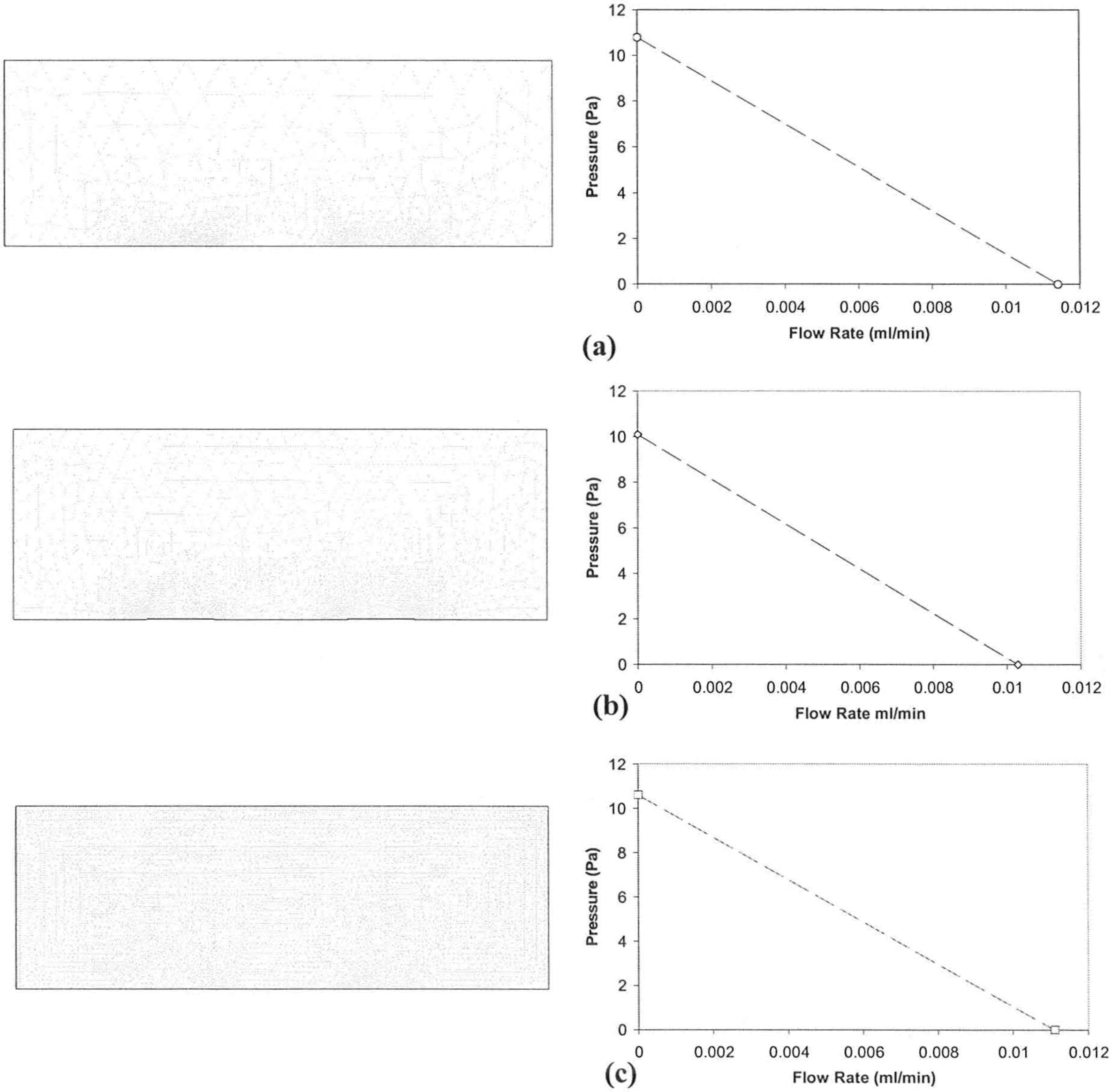

Figure 3.3: Mesh Quality with no flow and no pressure condition for (a) 2647 elements (b) 7852 elements (c) 11043 elements

$\mathbf{E^2}$	$\mathbf{E^3}$
$J_n = \frac{I_{\exp}}{AN}$	$J_n = \frac{I_{\exp}}{AN}$
$J_n = \left(\frac{I_{\exp}}{AN}\right)\left(\frac{e_n^2}{E_a^2}\right)$	$J_n = \left(\frac{I_{\exp}}{AN}\right)\left(\frac{e_n^3}{E_a^3}\right)$
$I_{\exp} = N.\int \frac{I_{\exp}}{AN}\left(\frac{e_n^2}{E_a^2}\right) dA$	$I_{\exp} = N.\int \frac{I_{\exp}}{AN}\left(\frac{e_n^3}{E_a^3}\right) dA$
$I_{\exp} = \frac{I_{\exp}}{AE_a^2}\int e_n^2\, dA$	$I_{\exp} = \frac{I_{\exp}}{AE_a^3}\int e_n^3\, dA$
$E_a^2 = \frac{1}{A}\int e_n^2\, dA$	$E_a^3 = \frac{1}{A}\int e_n^3\, dA$

Table 3.2: Equations used to determine charge distribution along the emitter based upon E^2, E^3.

To ensure the periodic boundary conditions imposed at the inlet and outlet accurately simulated the multi-stage effect, the simulations were repeated within a domain that had 6 stages of electrode pairs and compared (figure 3.4 (a)) to the single electrode pair case. The flow field and the pressure distribution under a no flow condition for S-80 at 400 V are shown in Figure 3.4 (b) and (c). The flow field within each stage is similar to that in the simulations for the single stage (Fig. 3.4b), and the pressure varies linearly across the six stages (Fig. 3.4c). The pressure gradient for the six stage case is 280 Pa/m and is in good agreement with the single stage value of 300 Pa/m. The small discrepancy is likely due to numerical errors caused by the coarseness of the elements which could not be refined further due to computational limitations. This indicates that the total pressure generation over several stages can be accurately estimated through the simulations of a single stage, thus saving considerable computational time and resources.

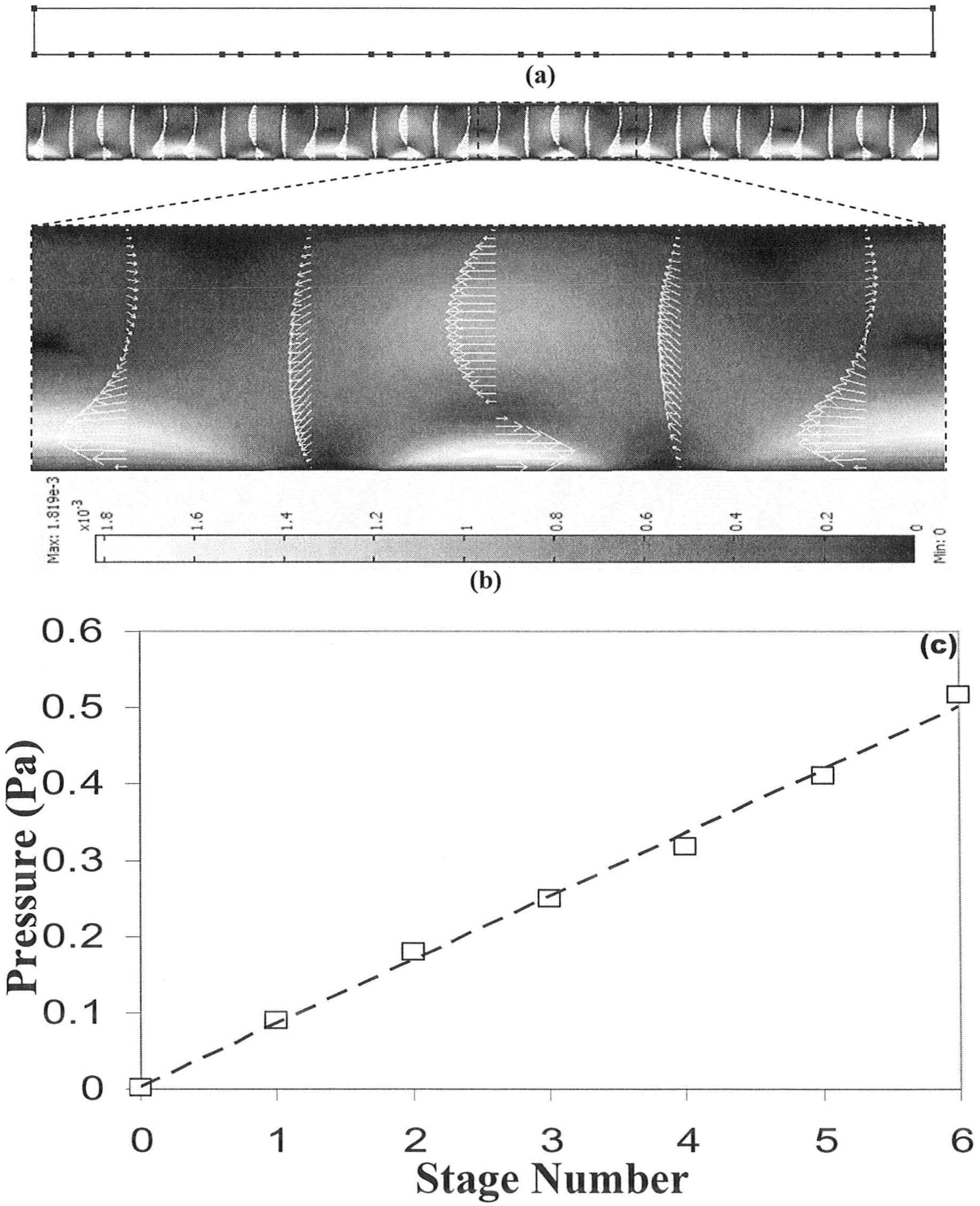

Figure 3.4: 6 stage S-80 micropump where (a) is the vertices of the domain (b) is the flow field and (c) is the pressure accumulation at the end of each stage at 400 V.

3.3 Experimental Validation

The simulation results for the pressure generated under a no-flow condition are compared to the experimental results of Kazemi et. al.(2009a). Figure 3.5 shows back pressure for the pump configurations S-80, S-120, A-80 and A-120. For the planar configurations, using the gradient model for charge at the surface is found to be in good agreement with experimental data (figure 3.5 (a) and (b)). The other relations tend to predict well at lower voltages but do not show the exponential increase in the pressure generation at the higher voltages. For the asymmetric configuration none of the three relations for charge gives results that are in good agreement with the experimental findings (figure 3.5 (c) and (d)). However, the gradient relation does capture the same trend that is seen in the pressure generation, showing the substantial increase in pressure with voltage compared to the other cases. A reason for this can be that asymmetry in the electric field lines are not found in the numerical model which would occur in reality. The asymmetric field lines will cause a greater fluid and electric field interaction hence increasing the body force for the fluid motion. Also the model is setup in a one-way coupling technique where the charge motion does not influence the electric field. In reality both entities are dependent on each other. However, due to lack of understanding of the charge injection process a two-way coupling technique is difficult to implement and causes instabilities in the convergence of the numerical model.

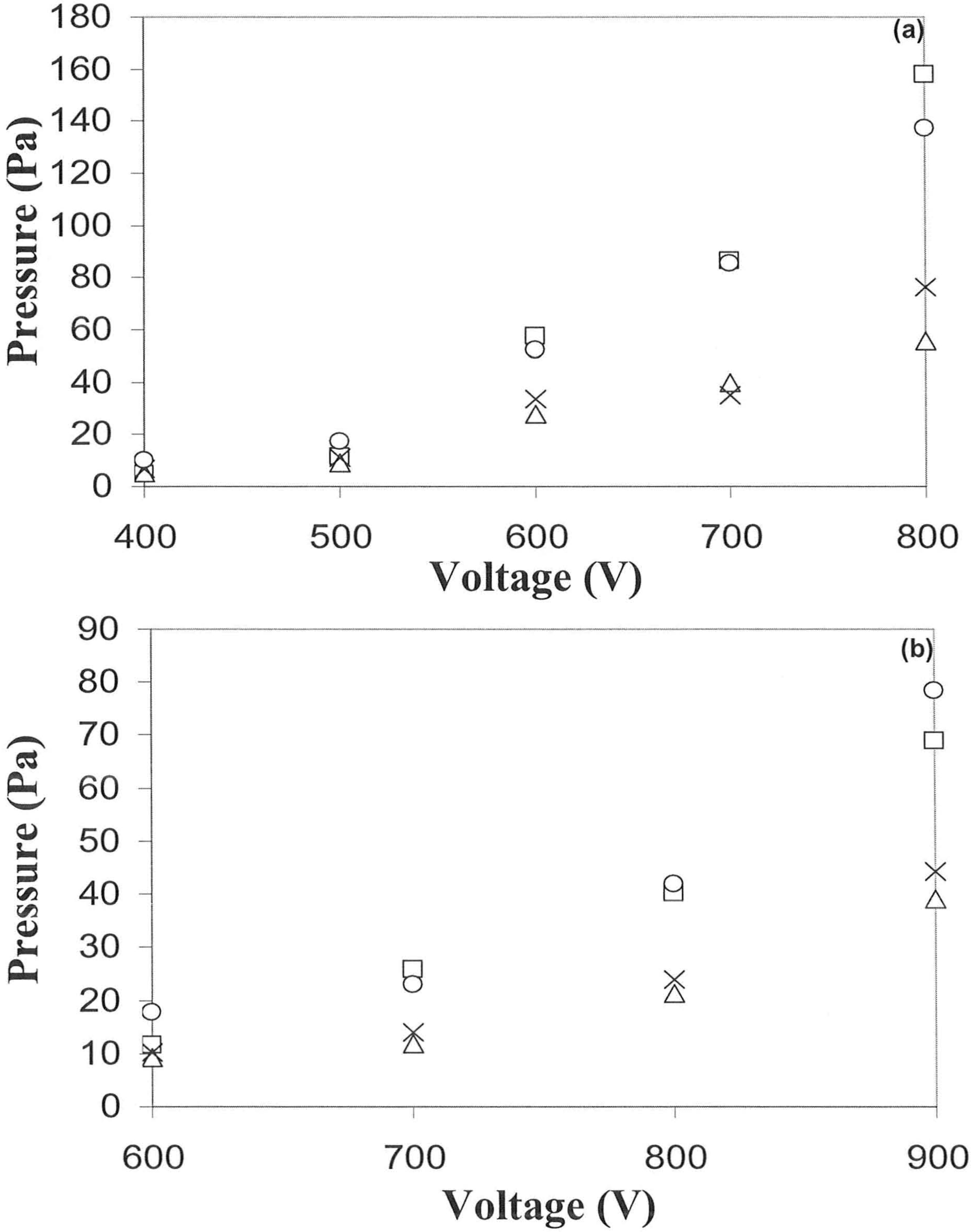
(a)
Pressure (Pa)
180
160
140
120
100
80
60
40
20
0
400
500
600
700
800
Voltage (V)
(b)
Pressure (Pa)
90
80
70
60
50
40
30
20
10
0
600
700
800
900
Voltage (V)

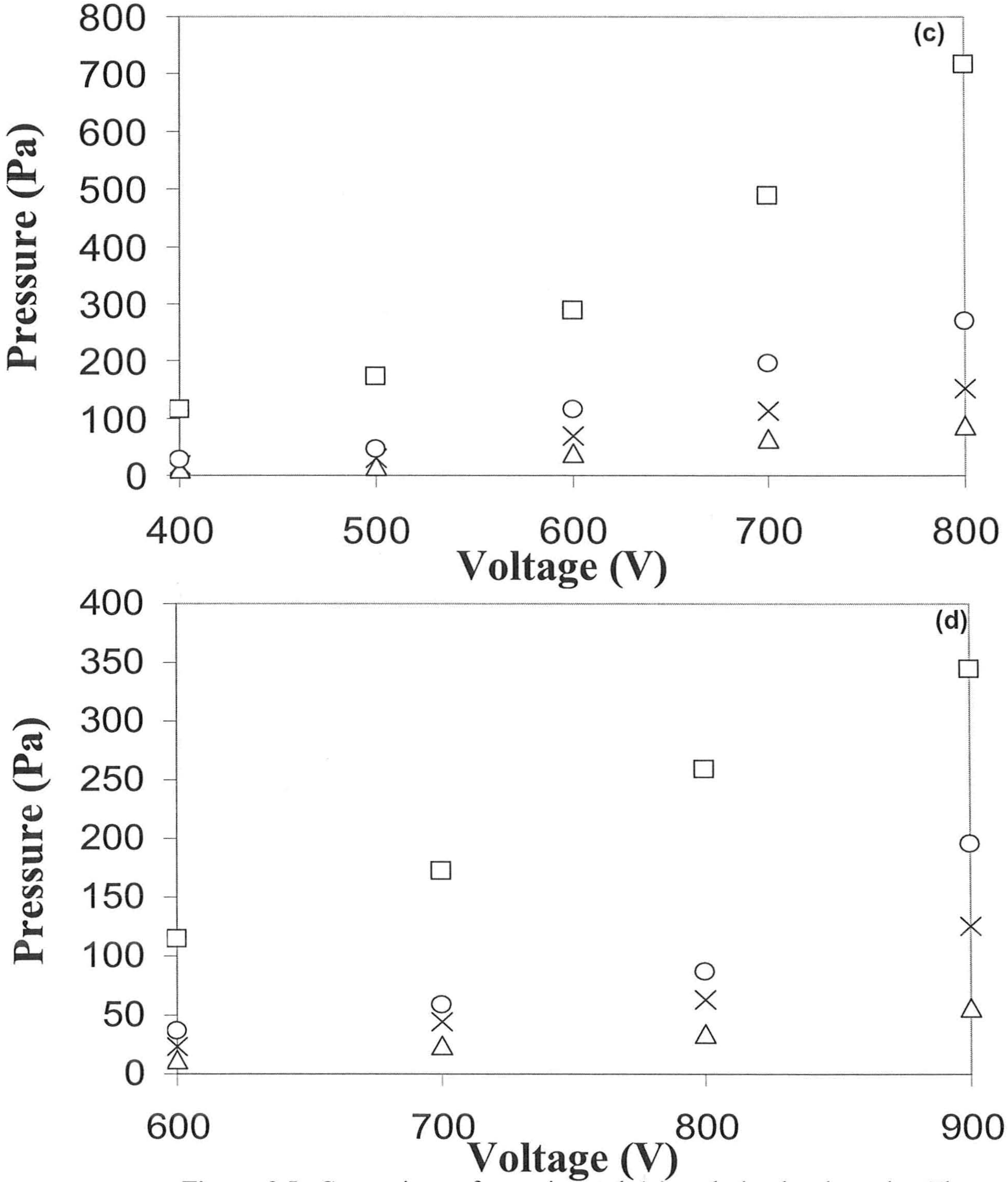

Figure 3.5: Comparison of experimental (□) and simulated results. The simulation was carried out with charge injection at the emitter dependent on local E^2 (Δ), E^3 (×), ∇E (○) distributions for (a) S-80 (b) S-120 (c) A-80 and (d) A-120.

Representative surface plots of the electric field distribution, charge motion, and flow field for S-80 at 400 V are shown in figure 3.6 based on the gradient relation. In figure 3.6 (b) the charge injection is primarily seen to occur at the edges of the electrodes. This is expected as corona discharge primarily occurs at sharp edges where electric field gradients are a maximum. Figure 3.6 (c) shows the flow field that is generated by the Coulomb force. The velocity is seen to be greatest corresponding to the electric field and charge density. In figure 3.6 (c) three recirculation zones can also be seen. This is because along the surface of the electrodes the charge injection and electric field lines are primarily in the y-direction, hence generating a body force upward. Also the interaction between opposing fluid direction, caused by the adverse interaction between neighboring stages, creates a net upward fluid motion.

The experiments were performed only for the no flow and no pressure conditions. This provides only the two extreme points on the operating curve of the micropumps. The numerical model developed here was used to generate the pump curves for the four configurations by performing simulations at different outlet pressures, and are shown in figure 3.7. Representative flow field plots under a no pressure condition at 600V is shown in figure 3.8. It was found that increasing the inter-electrode spacing causes a reduction in the pressure generation and in the flow rate. However, in figure 3.8 (a) and (b) it can be seen that increasing the spacing reduces the recirculation zones. This is also evident in the comparisons of asymmetric cases of A-80 and A-120 (figure 3.8 (c) and (d)). This is due to the electric field line and charge injection becoming more significant in the

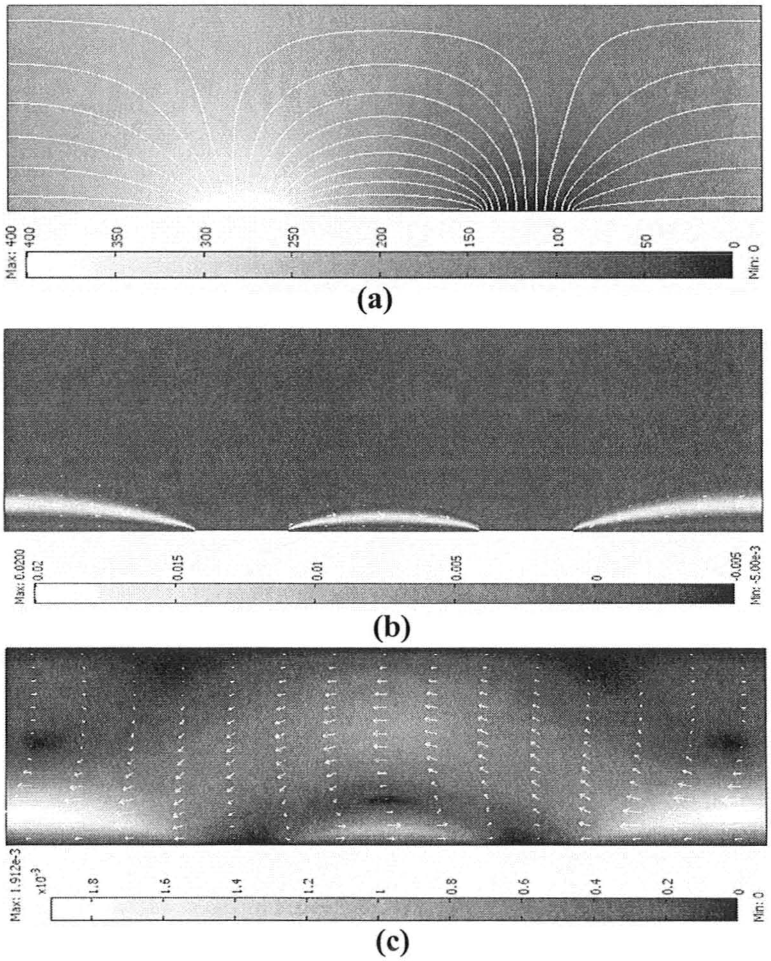

Figure 3.6: Plots of S-80 showing (a) Electric field (b) Charge density (c) Flow field at 400 V.

x-direction. Furthermore, comparing the asymmetric plots to the symmetric such as S-80 to A-80 (3.8 (a) and (c)) and S-120 to A-120 (3.8 (b) and (d)) the recirculation zones are reduced. This could be due to the electric field distribution in the y-direction being more concentrated in a finite region. Hence, the electrophoretic force in the y-direction is only concentrated on a finite region above the emitter and the charge density concentration is also more at the corner with respect to the surface of the electrode since the ratio of the local current flux coming from the surface to the corner is a lot smaller.

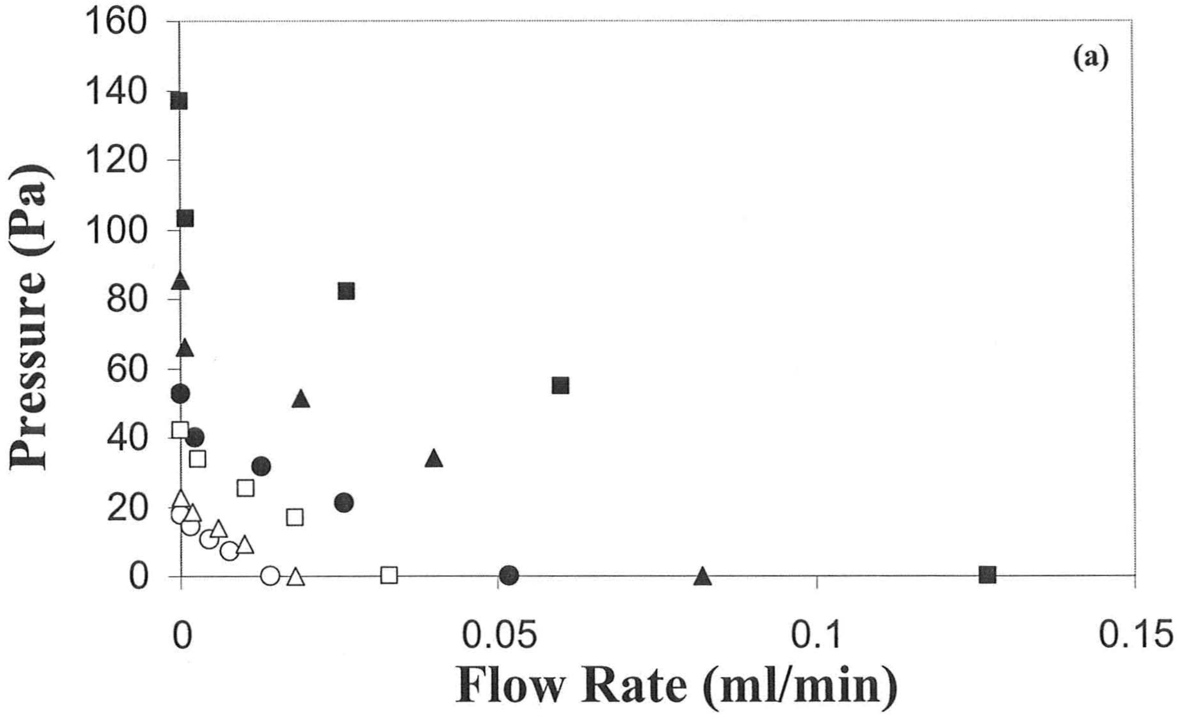

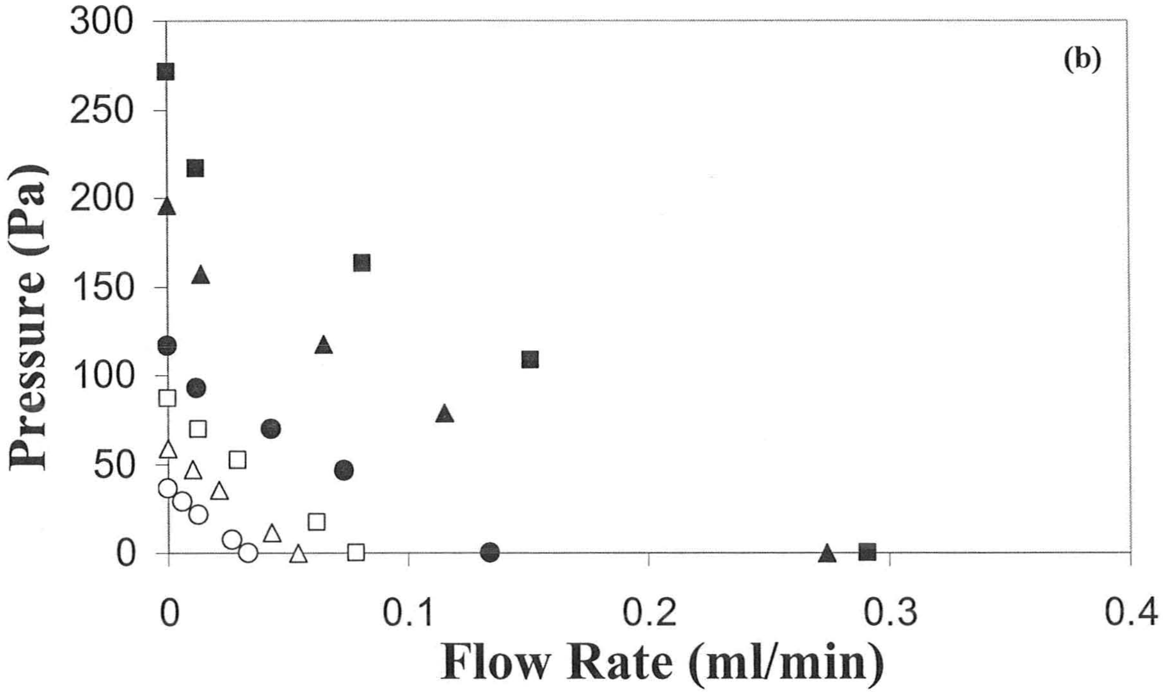

Figure 3.7: Pump curves obtained at various operating voltages for pump configurations (a) S-80 (filled) and S-120 (open) and (b) A-80 (filled) and A-120 (open) at ○ 600V, Δ 700V, and □ 800V.

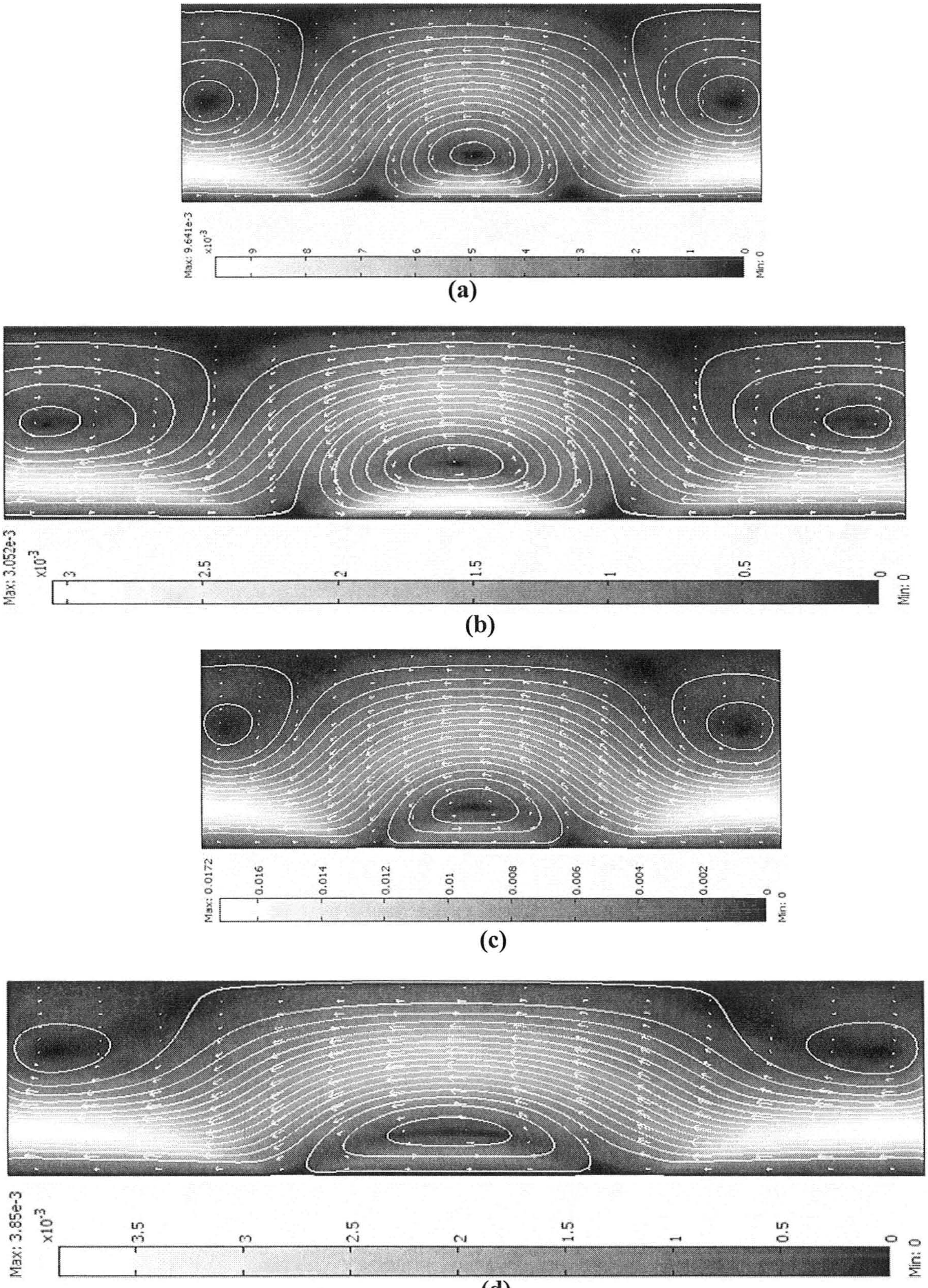

Figure 3.8: Flow field plots at 600 V for (a) S-80 (b) S-120 (c) A-80 (d) A-120

3.4 Parametric studies

The model developed here was also used to investigate the height of the channel and the multi-stage spacing on the EHD pump performance. However, a key problem when performing such parametric studies is that the current-voltage characteristics are not known a priori when a certain geometric parameter is changed. For this study an empirical model was developed to estimate the current-voltage characteristics. In order to estimate the current for the different parametric configurations, a correlation between the local charge density at the electrode and the corresponding magnitude and gradient of the electric field at the surface was developed through a multiple-variable regression technique. The empirical correlation can be represented as

$$\rho_n = A e_n^{\,B} \left(\frac{\partial e}{\partial y} \right)^C + D \qquad \text{[Eq. 3.13]}$$

where *A, B, C,* and *D* are constants determined from the regression, and the values are given in Table 3.3 for the different pump configurations. The correlation is shown for S-80 in Figure 3.9. The current values estimated by integrating the local charge density over the electrode surface are compared to the experimental values in Figures 3.10 (a) and 3.10 (b). There is good agreement between the estimated and experimental values, indicating that the relation obtained at one particular voltage can be used to estimate the current at other applied voltages for a given pump configuration.

Constants	**S-80**	**S-120**	**A-80**	**A-120**
A	2.24×10^{-20}	3.41×10^{-19}	2.49×10^{-17}	3.52×10^{-20}
B	1.59	1.76	1.07	1.81
C	0.45	0.25	0.52	0.28
D	-4.00×10^{-4}	-2.09×10^{-4}	-3.34×10^{-4}	-2.46×10^{-4}

Table 3.3: Arbitrary constants for S-80, S-120, A-80, and A-120

The parametric studies were performed for channel heights of 50, 100, 120 and 150 microns, and inter-electrode to multi-stage spacing ratios of 1:2, 1:3, and 1:4 while keeping the inter-electrode spacing at 80. The electric field gradient was first determined at 600 V by solving the Laplace equation (equation 3.11). This was then compared to the electric field gradients of S-80 at applied electric potentials from 100V to 1000V. Since in each of the study the electrode dimension remains the same, it can be assumed that if the new pump configurations have a similar field distribution to S-80 then the charge distribution will be the same as the charge injection is dependent on it. To illustrate the accuracy of the comparison, the electric field for 50 micron channel height and S-80 is compared and shown in figure 3.11. It was found that when the 50 microns height configuration was compared with electric field of S-80 at 525 V, the R-square value for the trend line was 0.9972. Therefore, the assumption made is acceptable and the equation derived for S-80 can be used to determine the charge for the parametric study. For the 120 microns, and 150 micron channel height it was found that the relation remains the same as 100 micron channel height which was used in S-80.

The pump curves for the different channel heights at 600V are shown in figure 3.12. Reducing the height causes a higher pressure generation.

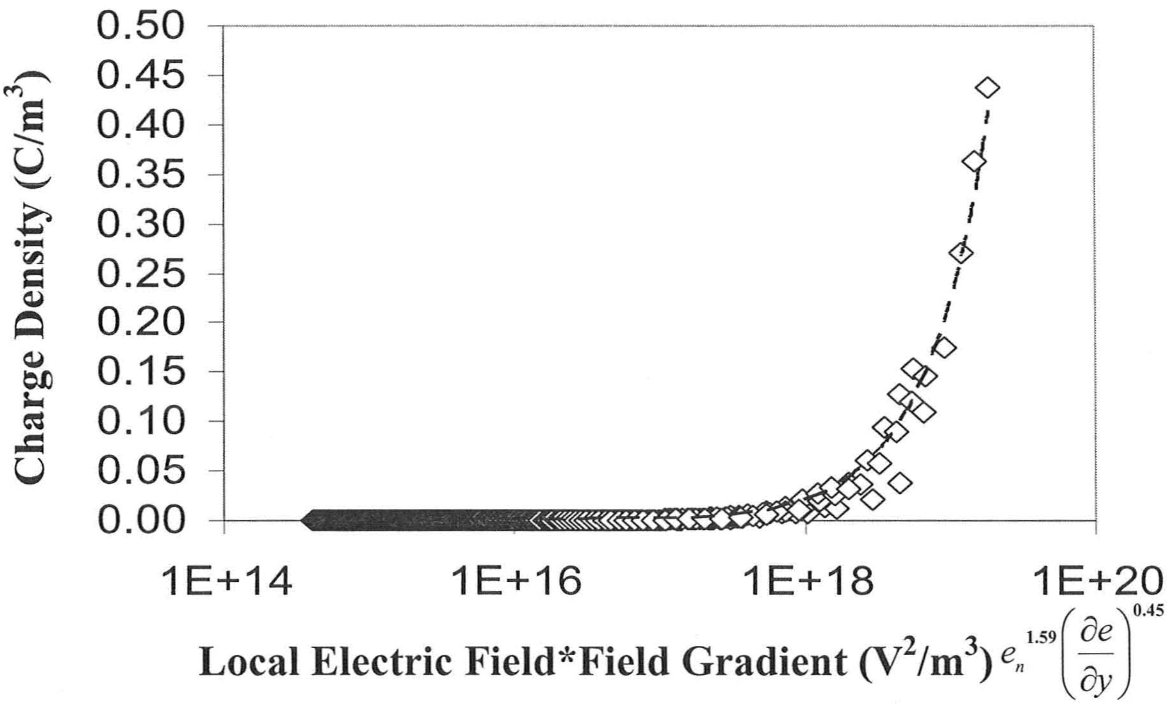

Figure 3.9: Local charge density and electric field relation along surface of electrode for S-80.

However, increasing the height will cause a greater flow rate. Reducing the height causes a greater wall shear stress; hence a higher pressure is required to achieve flow. Since the resistive force on the flow is so high the net flow is much lower. Increasing the height reduces the wall shear stress. Hence, a lower pressure generation is required to overcome the resistive force and a higher flow rate is achieved for that pressure. However, by increasing the height of the channel the recirculation zones are much more significant as the Coulomb force is, relative to other heights, more significant in the y-direction to the electric fields being more present there. The plots for the flow field for these heights can be found in figure 3.13 (a) to (d) for 50, 100, 120 and 150 microns height.

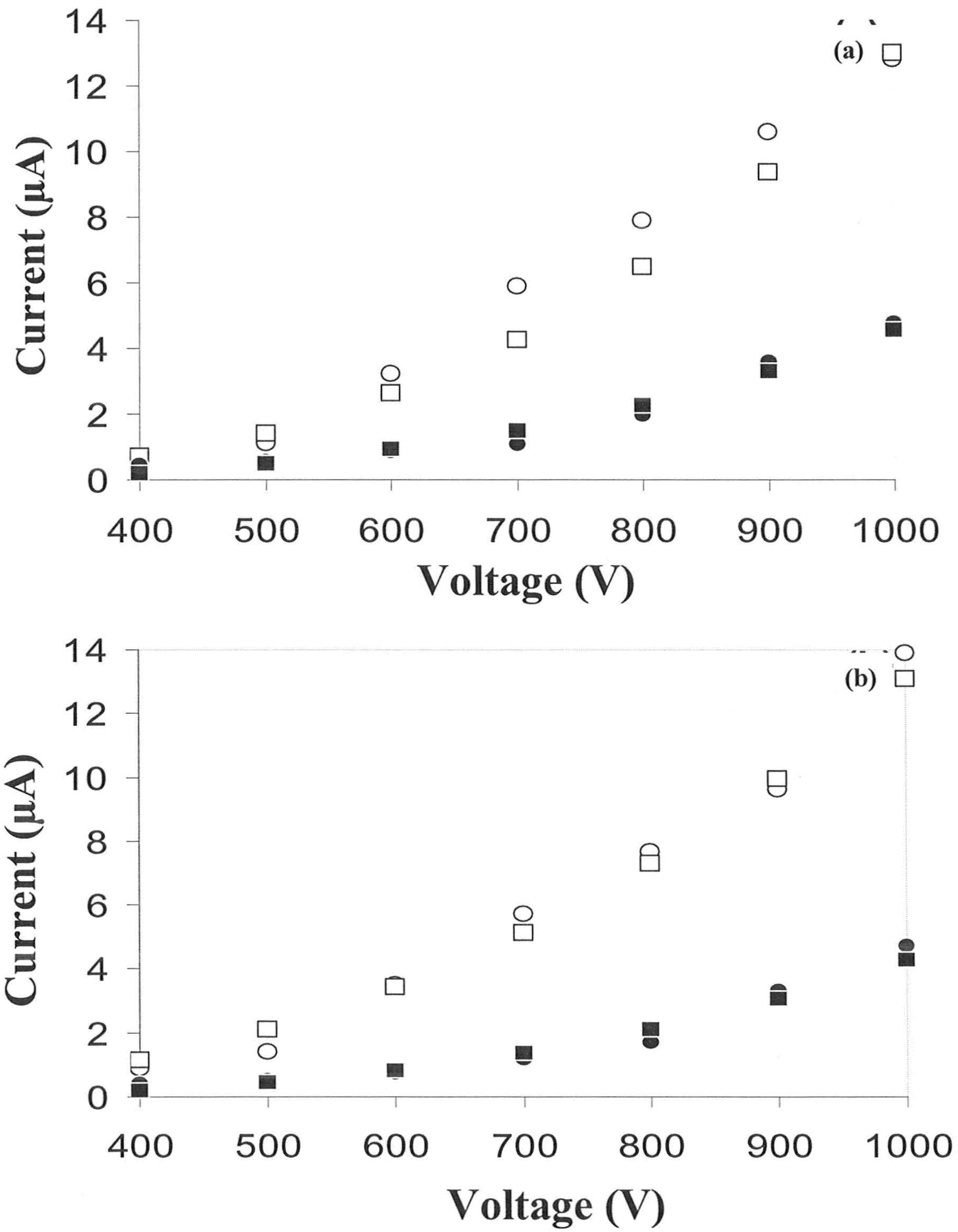

Figure 3.10: Comparison of experimental current (○) to approximated current (□) for (a) S-80 (open) (b) S-120 (filled) (c) A-80 (open) (d) A-120 (filled).

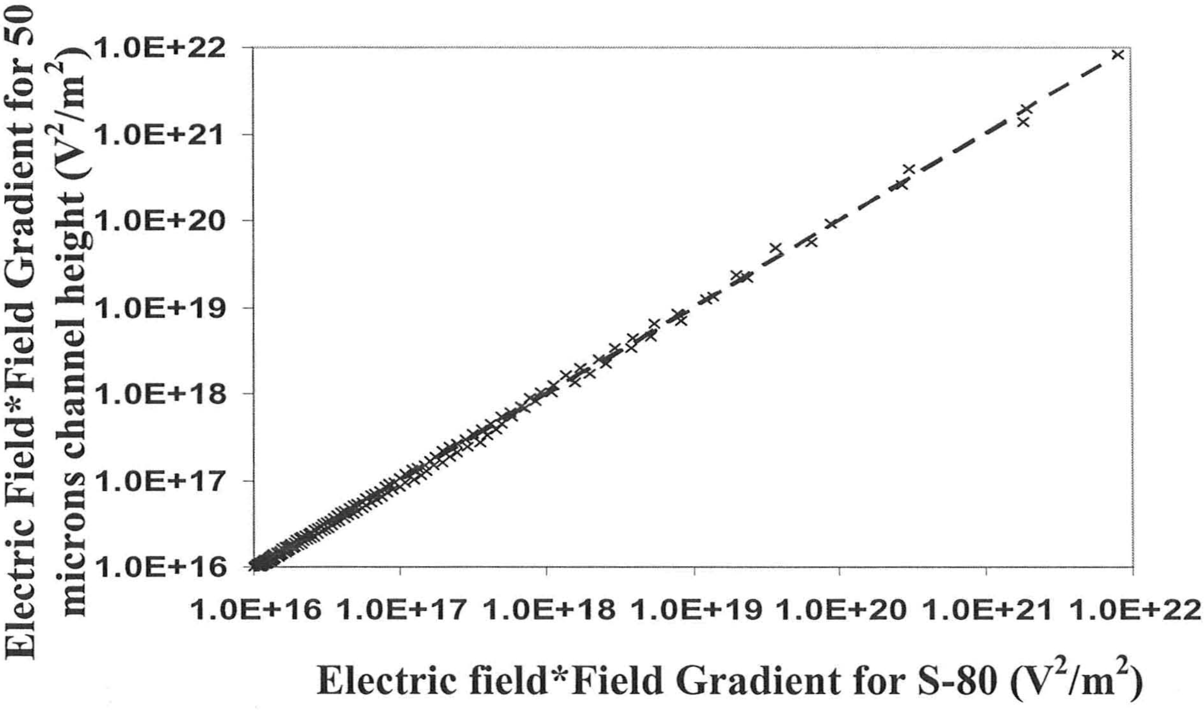

Figure 3.11: Trend line of data for 50 micron channel height configuration at 600V (---) channel height vs. S-80 at 525V (x).

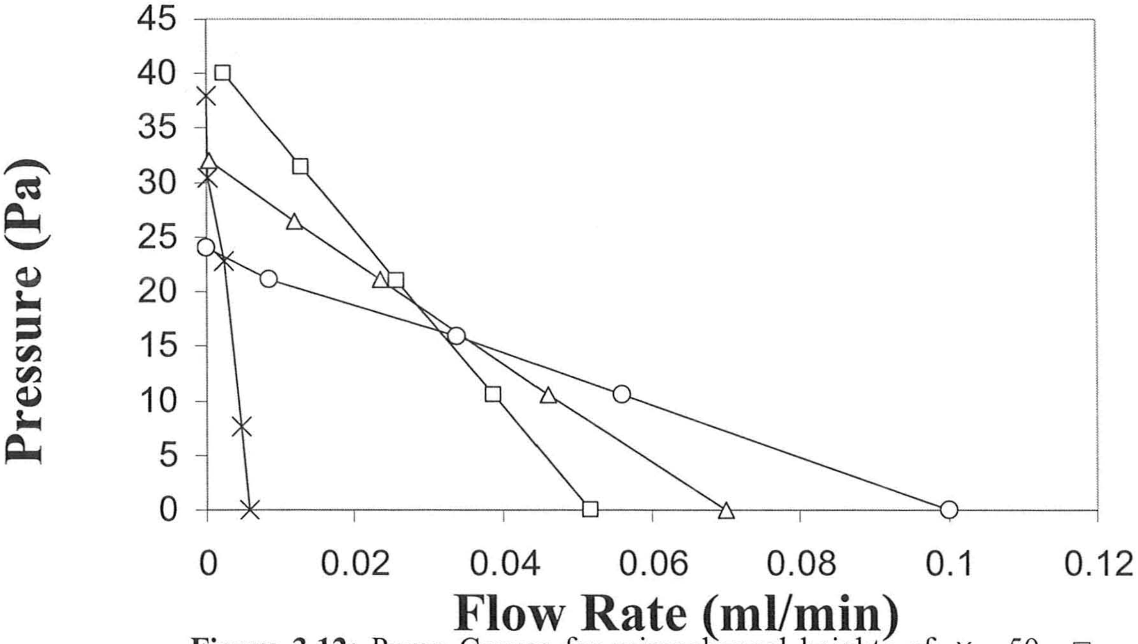

Figure 3.12: Pump Curves for microchannel heights of -x - 50, -□- 100, -Δ- 120, and -○- 150 at 600 V.

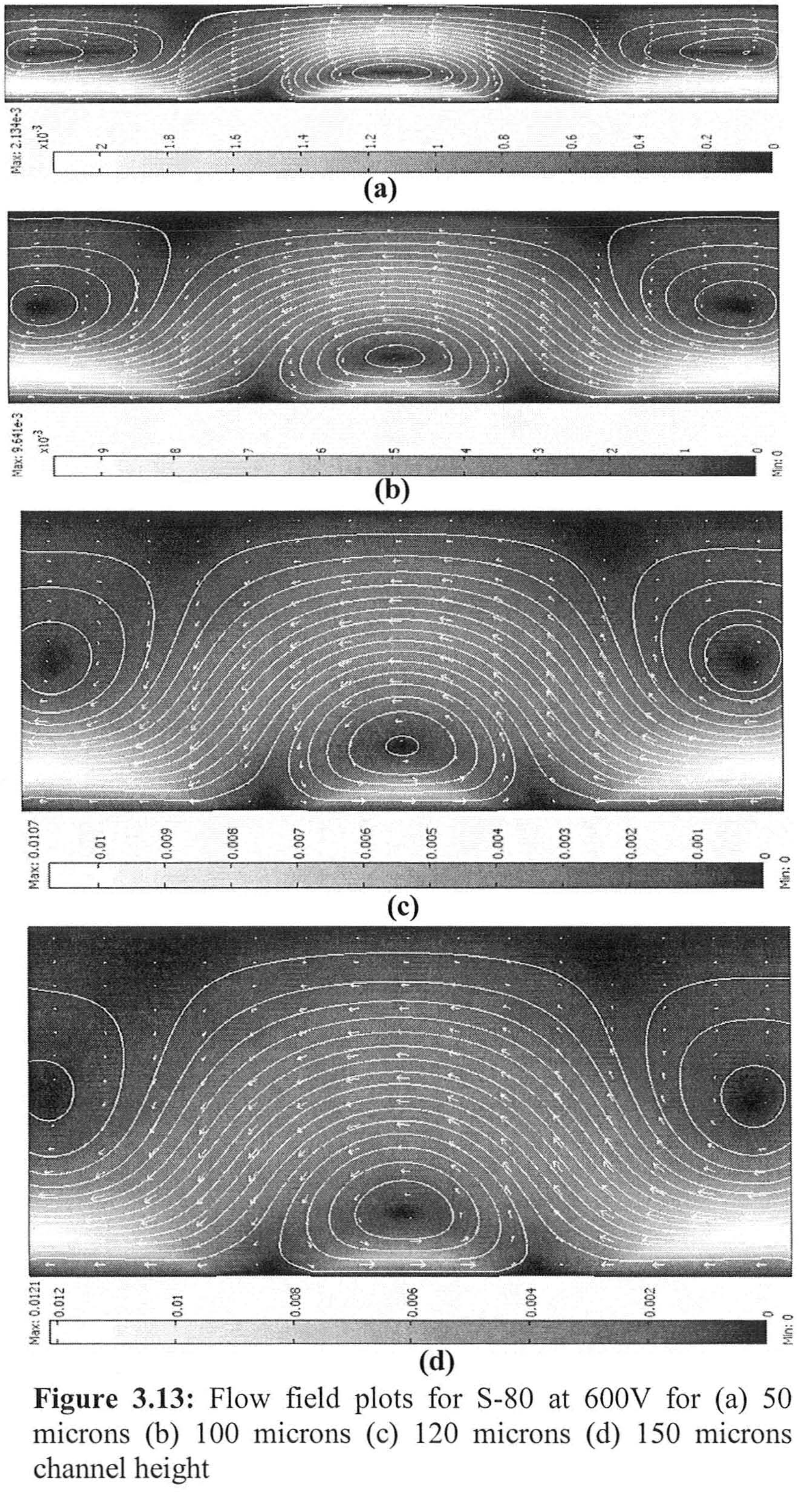

Figure 3.13: Flow field plots for S-80 at 600V for (a) 50 microns (b) 100 microns (c) 120 microns (d) 150 microns channel height

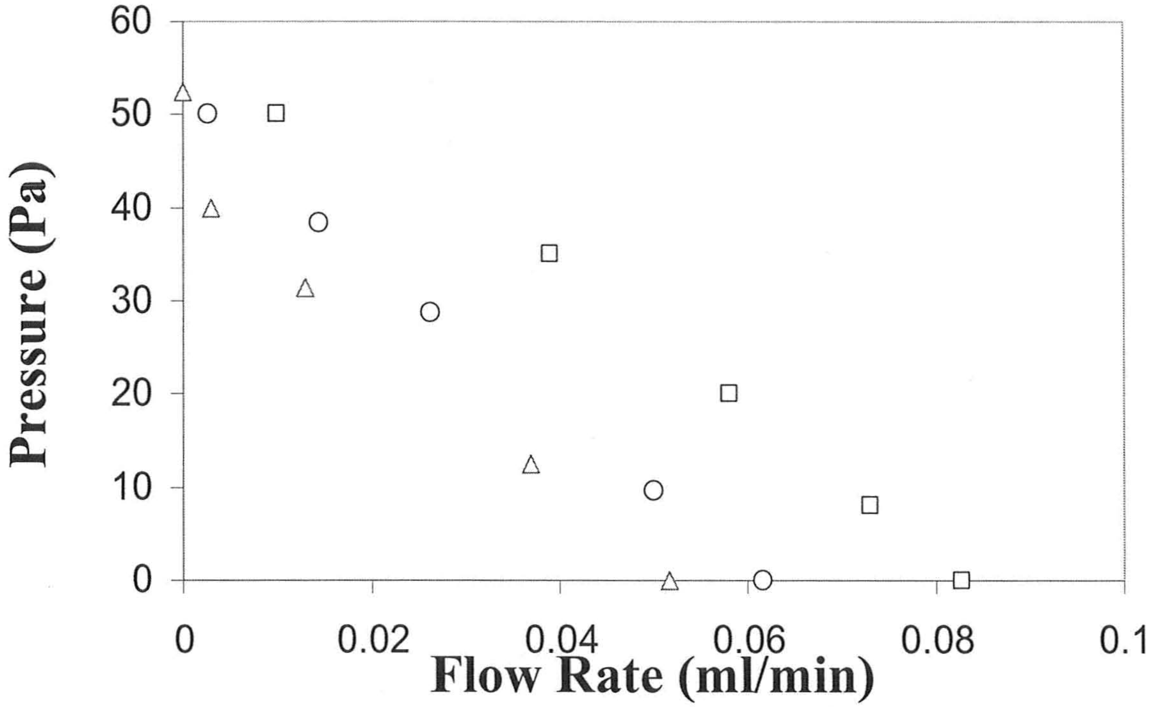

Figure 3.14: S-80 at 600V pump curves for Δ 1:2, ○ 1:3, and □ 1:4 multi-stage to inter-electrode spacing.

The effect of the ratio of the multi-stage spacing to the inter-electrode spacing on the pump performance is shown in Figure 3.14. It was found that increasing the multi-stage spacing caused a reduction in the pressure head. This is because increasing the multi- stage spacing results in a spatial increase in the pump size. Therefore, in order to fit the pump in the same spacing the number of stages is reduced. However, increasing their spacing reduces the adverse interaction between the neighboring stages. This results in an increase in the flow rate. Furthermore, increasing the spacing reduces the recirculation zone as the electric field interaction between the neighboring stages is stretched in the x-direction. Figure 3.15(a) to (c) shows the flow field plots for 1 to 2, 1 to 3, and 1 to 4 respectively.

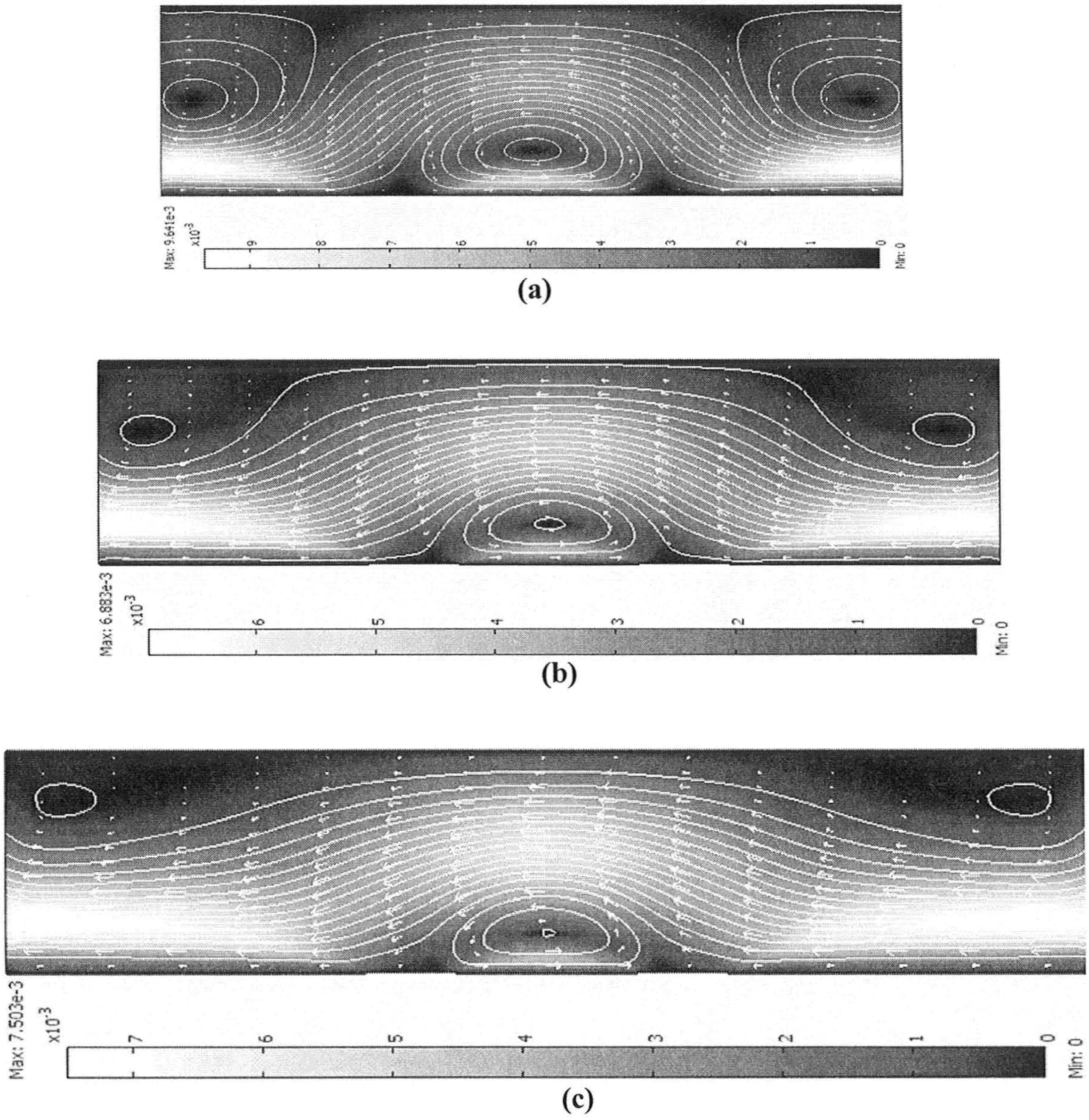

(a)

(b)

(c)

Figure 3.15: Plots for S-80 600 V for (a) 1:2 (b) 1:3 (c) 1:4 multi-stage to inter-electrode spacing.

3.5 Summary

A numerical model was developed for EHD ion drag micropumps that takes into account the effect of the electric field on the charge distribution. In particular, the local charge distribution at the emitter electrode is assumed proportional to the electric field gradient and estimated from a known current value. Simulations were performed for EHD micropumps that consisted of a series of electrode pairs embedded along the bottom wall of a microchannel. The simulation results for the pressure generation were in good agreement with existing experimental results (Kazemi, 2009a). The model was used to generate head-flow characteristic curves for the pumps. Generally the head-flow showed a linear correlation to the pressure condition set at the outlet. It was also seen that increasing the inter-electrode spacing had an adverse effect on the pumping performance.

Chapter 4: Design, Microfabrication Process, and Fluid Selection

4.1 Introduction

Over the past few years the rapid progression in microfabrication technology has allowed the development of miniaturized features at the microscale. With this advancement, diverse applications of micro-electro-mechanical systems (MEMS) have been realized. These technologies allow micro devices to be produced with precision and at a relatively low cost. Advancements have been made in ion-drag EHD pumping over the past several years in terms of its miniaturization and performance. However, several issues related to this pumping technique still exist. One particular problem is the variation in its performance due to degradation of the electrodes, or the fluid. This can result in a very short life cycle of the pump, which can be of a few hours (Benetis, 2005).

One aim of this research is to investigate the use of dopants in the working fluid to enhance the performance and stability of an EHD micropump. This will reduce the dependency of charge injection from the solid-liquid interface to create the ion-drag effect. Another technique to enhance the stability and performance is to use a pulse voltage instead of DC voltage. This will allow large electric potentials to be applied for short periods of time.

4.2 Pump Configuration

For this study, an asymmetric planar electrode design was selected. Here, the emitter width is half of the collector width. The reason for selecting this electrode geometry is that it was shown to have a better performance than a symmetric electrode configuration (Kazemi et. al, 2009a). The asymmetric electrode geometry creates an asymmetric electric field, which causes a greater interaction between the fluid and electric field, resulting in a higher electrophoretic force being exerted on the fluid. Electrode configurations that have been designed and tested in the past, aside from planar electrodes, include (1) Three-dimensional micropillar structures (Kazemi et. al., 2009b) and (2) Grid-type electrode (Richter and Sandmaier 1990).

In the three-dimensional micropillar structure, the electrodes protrude into the flow domain. The height of the electrode is typically as high as the channel height, thus charge injection occurs over most of the flow domain, instead of it being local to the vicinity of the planar electrodes. A schematic of a microchannel with micropillars is shown in figure 4.1. However, challenges in using 3D electrode structures is in the fabrication, as getting consistent size structures is very difficult and time consuming. If the micropillars are underdeveloped it could result in two problems. One is where the pillar is in contact with the top surface of the channel. This can cause strain on the channel enclosure and its seal. The other problem is mushroom shape electrode structure. This can result in a micropillars coming into contact with its adjacent neighbors. Figure 4.2 (a) and (b) illustrate the problem seen in developing micropillar structures. Degradation of the electrodes can also be a problem as materials that are used to form micropillars (i.e. Nickel) typically have low oxidation resistance so that there is good adhesion with electrode surface.

In a grid type electrode configuration, the emitter and collector comprise of two plates with symmetric grids of certain diameter. The electrodes are placed perpendicular to the flow direction to allow electric field and fluid interaction. An example of an EHD pump with a grid-electrode configuration is shown figure 4.3. A grid-type electrode configuration is well suited for channels that are in cm scales. This is because the pump performance depends on the number of grids on the surface of the plates which is known as the grid density. The grid density is limited by the thickness of the substrate, the surface roughness, and the etching process itself, while in planar micropumps the feature size is subjected to the mask feature size which can be of several microns.

For this investigation, an asymmetric planar electrode configuration was used. Some important parameters that are considered when designing micropumps are the inter-electrode spacing (E_S), emitter width (E_{EW}), collector width (E_{CW}), multi-stage spacing (M_S), electrode thickness (E_T), channel height (H_C), and channel width (W_C).

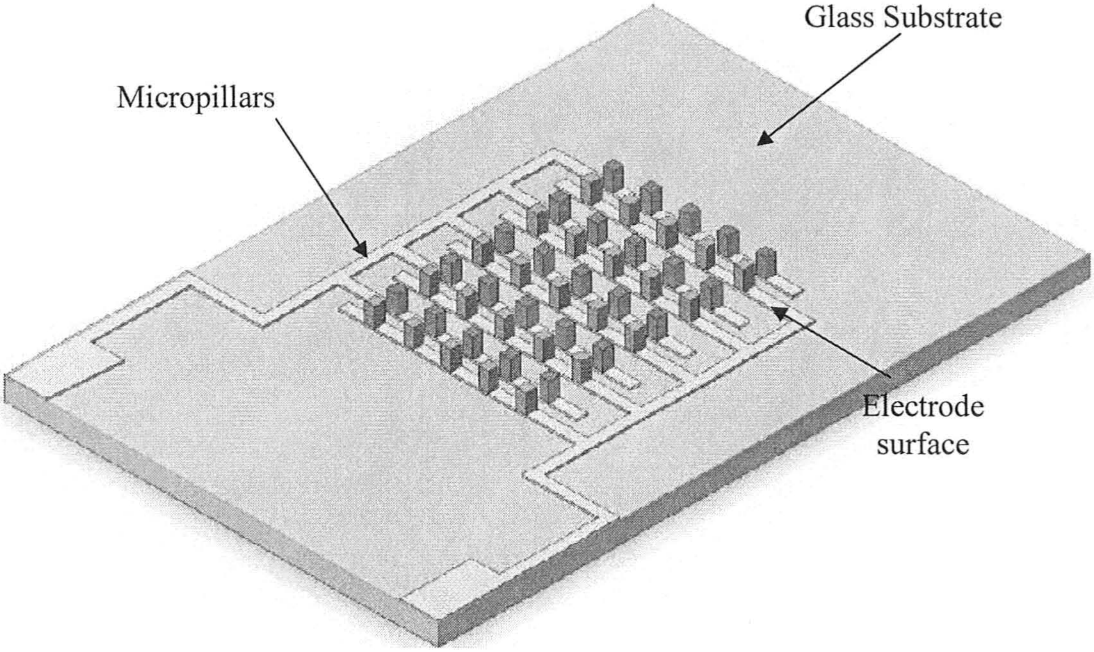

Figure 4.1: 3D illustration of EHD micropump with micropillar structures (Kazemi et. al., 2009b).

An illustration of the parameters in context to the micropump design is shown in figure 4.4. A summary of the micropump configurations is given in table 4.1. The pumps are labeled with the prefix 'A-,' to indicate that they are of asymmetric planar configuration while the number at the end represents the inter-electrode spacing. The number of stages that were selected for the micropumps was 100, which was considered an appropriate for size of the substrate that electrodes are developed on and for the range of dimensions that was used for the pumps.

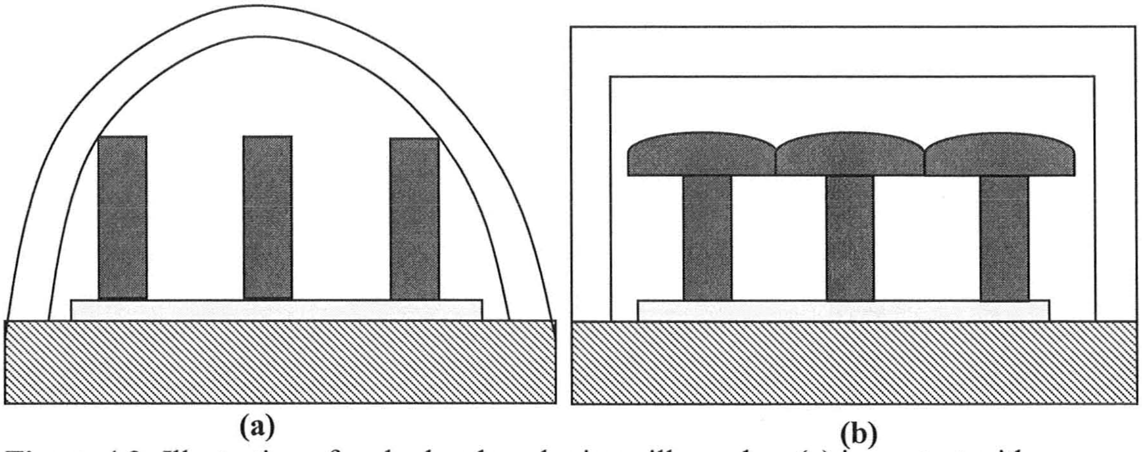

Figure 4.2: Illustration of underdeveloped micropillars when (a) in contact with microchannel surface (b) mushroom-shape is form.

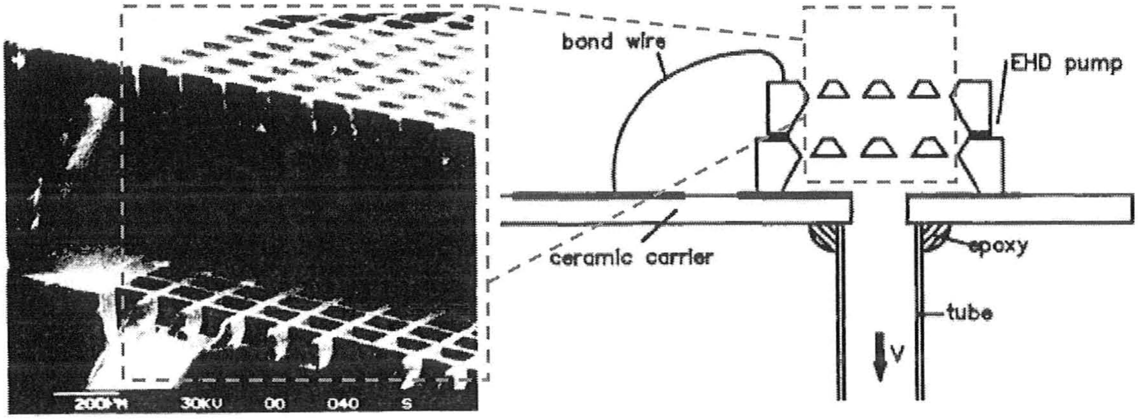

Figure 4.3: Example of EHD pump with grid-electrode configuration employed by Ritcher and Sandmaier (1990).

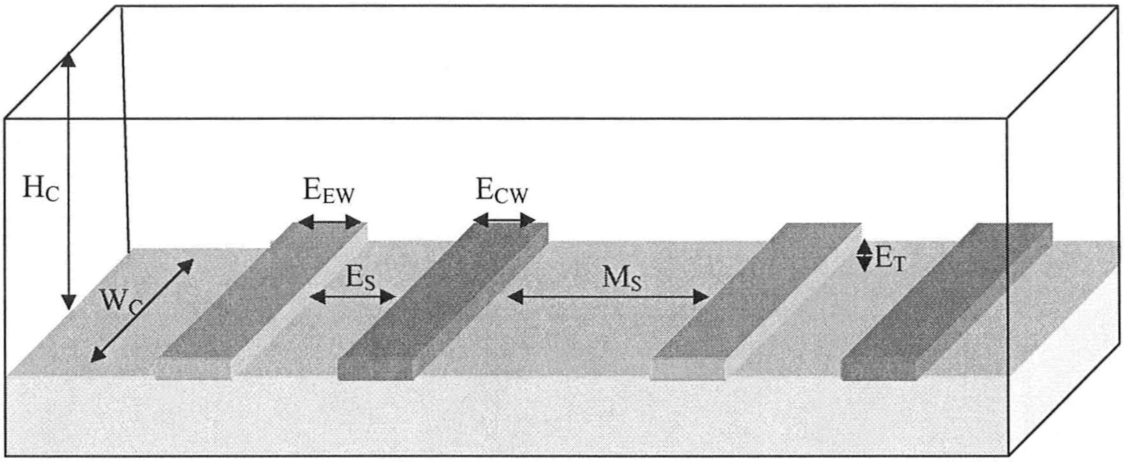

Figure 4.4: Illustration of parameters in EHD micropump configuration.

Pump	**W_C (mm)**	**H_C (µm)**	**E_T (µm)**	**E_{EW} (µm)**	**E_{CW} (µm)**	**E_S (µm)**	**M_S (µm)**
A-40	5	100	0.25	20	40	40	80
A-80	5	100	0.25	20	40	80	160
A-120	5	100	0.25	20	40	120	240

Table 4.1: Summary of pump configuration used for experiments

4.3 Material Selection

The substrate material for the electrodes for the micropump was selected based upon electrical properties, cost, and availability. Ideally the material should be electrically insulating so that the emitter and collector electrodes are isolated. In this instance, Pyrex Glass wafers of 7.62 cm (3 inch) diameter and 500 microns thickness was used as the substrate. The wafer has a low surface roughness, which allows more precise fabrication.

In order to select the appropriate material for the electrodes the work function must be determined. The work function provides a guideline for the ability of the material to inject charge. Fowler (1928) derived the equation to determine the work function as:

$$J(E) = \mathbf{1.545 \times 10^{-6}} \frac{\beta^2 E^2}{\varphi} \mathbf{exp(-6.83 \times 10^{-7}} \frac{\varphi^{3/2}}{\beta E}\mathbf{)} \qquad \text{[Eq. 4.1]}$$

where J represents the current density, E is the electric field strength, β is a field enhancement factor related to the electrode geometry, and φ (eV) represents the work function of the material. Table 4.2 provides a list of work function of several metals. Since current density is inversely related to the work function of the material, aluminum would offer the most charge injection. However, aluminum is susceptible to electrochemical corrosion which will cause a quicker degradation of the pump.

Metal	Au	Al	Cr	Cu	Nb	Ni	Pt
Work Function (eV)	5.1	4.28	4.5	4.7	4.3	5.15	5.65

Table 4.2: Work function of various metals

The metal is deposited onto the substrate through electron-beam evaporation technology. This system allows precise control over growth rate and film thickness in the angstrom scale. Based upon the availability of metals in this system, the work function, and resistance to electrochemical corrosion, Gold was considered to be the most appropriate metal. A thin layer of Chromium has to be deposited first to act as an adhesion between Gold and glass.

4.4 Microfabrication Process

The fabrication of the EHD micropumps can be divided into three steps: (1) electrode fabrication, (2) microchannel development and (3) integration of microchannel and electrodes. The process flow of the electrode fabrication is shown figure 4.5. Initially a 100 Å of Chromium followed by a 2400 Å Gold layer is deposited on the substrate (Figure 4.5 (a)). The Chromium is deposited as an adhesive layer between the Gold layer and the glass substrate. Next, S1808 (from Microchem Corp.) photoresist is spun onto the sample at 4000 rpm for 30 seconds (Figure 4.5 (b). The photoresist is of positive type with a low viscosity. Therefore, at such spinning conditions a relatively uniform thickness is achieved. The sample is then soft baked at 110^0C for 2 minutes to remove any solvent present and to improve the adhesion between the photoresist and sample. The photoresist is exposed to Ultraviolet light at desired regions with the aid of a mask (Figure 4.6) at 30 mJ/cm^2.

The substrate is then submerged into a solution of 1 part photoresist developer 351 (Microchem Corp.) and 5 part de-ionized water (DI water). This removes the exposed photoresist and requires 45-60 seconds. At completion the sample is removed and dipped into DI water for a brief period to remove any residue initially and then rinsed in DI water again for 5 minutes. The sample is then dried off by applying nitrogen and then hard baked at 130^0C for 2 minutes. This allows further cross-linking to occur between the photoresist molecules and gives further adhesion to substrate (figure 4.5 (c)).

After hard-baking the photoresist etching of the metal layers is performed. The gold layer is first etched using a Nickel- compatible Gold etchant by Sigma Aldrich. This chemical gives an etch rate of about 40-50Å/s and hence about 48-58 seconds is required to remove the unwanted gold (figure 4.5 (d)). Once the gold layer is removed the sample is dipped and then rinsed with DI water for 5 minutes. The etchant that is used for Chromium is also manufactured by Sigma Aldrich. However, the etch rate is very fast with respect to the thickness of the chromium layer (40 Å/s). In order to reduce the rate the etchant is diluted with DI water in a ratio 1 to 4 to give an etch time of 30-45 seconds. Once the chromium is removed the sample is once again dipped and then rinsed with DI water and then dried out with nitrogen (figure 4.5(e)).

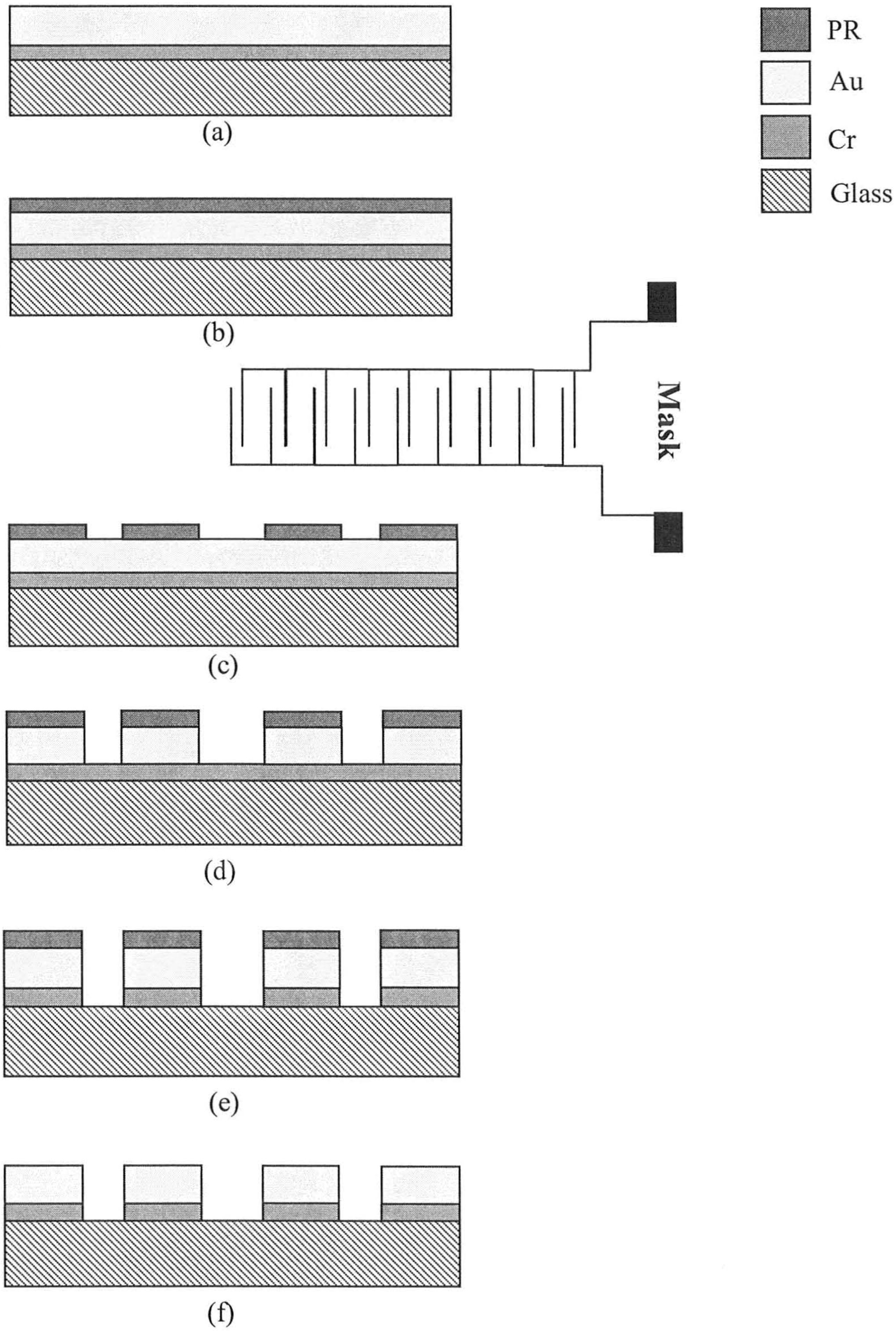

Figure 4.5: Process flow for electrode fabrication

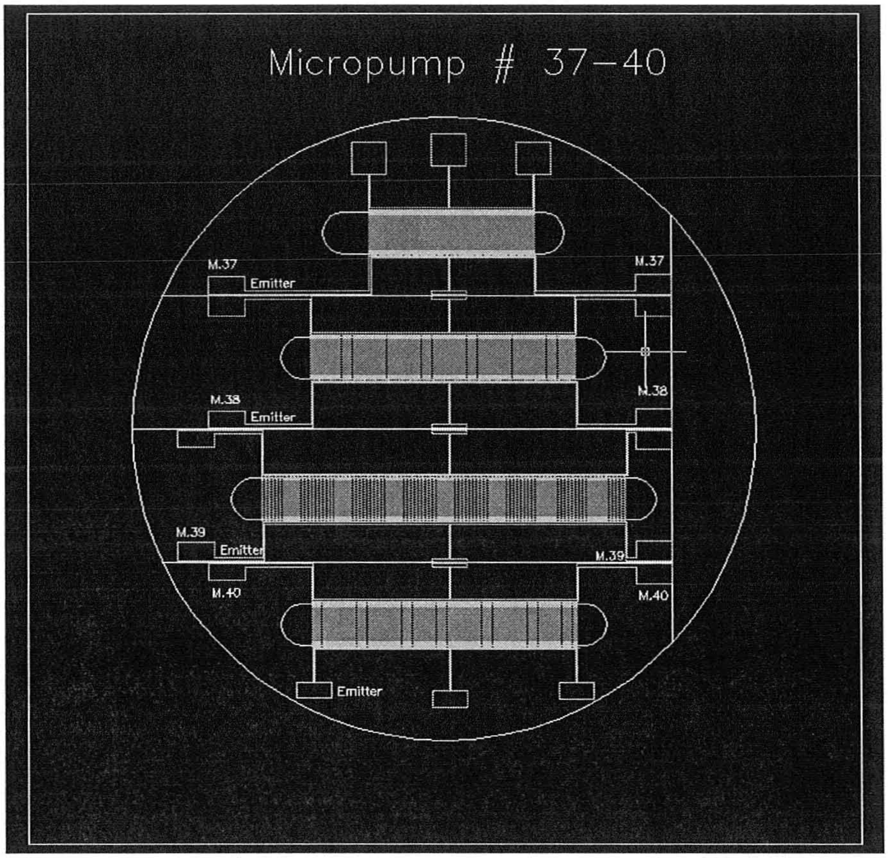

Figure 4.6: Mask drawing used in photolithography process.

Finally the photoresist is removed by rinsing and sonicating in acetone for 5 minutes. This step is then repeated again with methanol. The substrate is then dipped and rinsed in DI water for 5 min, followed up by drying it with nitrogen. If photoresist residue still exists on the sample it is plasma oxidized at 50 W for 30 minutes. Figure 4.7 shows a sample of the A-40 pump.

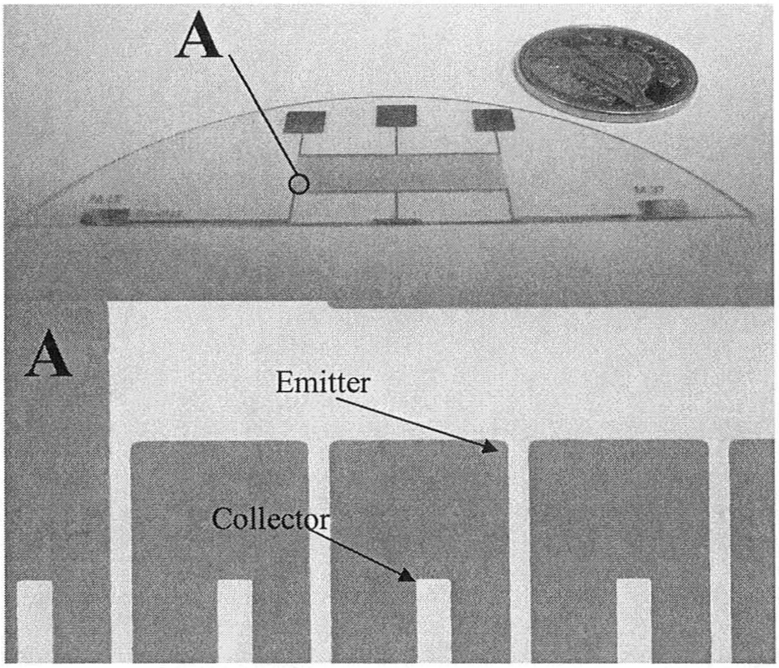

Figure 4.7: Sample of the A-40 pump

The microchannel for the micropump is fabricated from Polydimethylsiloxane (PDMS). PDMS is a polymeric organosilicon compound, and holds several advantages in the packaging process of the device. It comes in a liquid form and can be cast over a mould to produce the channel. Hence the size and shape of the channel is limited to the mould itself. It is also optically clear allowing the fluid to be observed. The mould can be used repeatedly, making this process relatively cheap and efficient. The mould is created using SU-8 100 photoresist by Microchem Corp. A 7.62 cm mechanical grade single-side polish silicon wafer of 500 microns thickness is used as the substrate to create the mould.

The photoresist is gently poured onto the substrate of approximately 3 ml in portion. The sample is spun initially at 500 rpm for 10 seconds to cause an even distribution across the centre of the wafer. The sample is then spun at about 2500 rpm for 30 seconds with ramp of about 400 rpm/sec to achieve 100 micron thickness along the substrate. Next, the sample is pre-baked at 65^0C for 10 minutes followed by a soft bake at 95^0C for 30 min. The temperature is ramped up by 10^0C per minute and is held at the interval for 10 minutes. The sample then undergoes a photolithography process to initate the cross-linking of the photoresist in the desired regions. About a 600 mJ/cm^2 exposure is required for the cross-linking. Once this process is completed the sample is taken for a post-exposure bake. The temperature is initially set at 65^0C for 1 minutes and taken up to a final temperature of 95^0C and is held there for 10 minutes. The ramping of the temperature is again carried out at 10^0C per minute. The sample is then developed using SU-8 Developer by Microchem Corp. The time required to develop the sample is approximately 10 minutes. In order to check that the photoresist is developed the sample is rinsed with Isopropanol (IPA) to check if any white residue is present, where at this point the sample is placed back into the developer solution. If no residue is present the sample can be rinsed with DI water and then dried off with Nitrogen. Paraleyne is deposited on the mould to ensure there is no adhesion between the mould and PDMS when it is cured, making it more durable. The next step is to develop the channel and integrate it to the electrode substrate.

The mould is used to cast the channel, and the channel is integrated to the electrode substrate is a shown schematically in figure 4.8. The PDMS mixture that is used for the channel is 1 part curing agent to 10 parts elastomer. The mixture is poured over the microchannel mould and cured for approximately 1 hour at a temperature of 65^0C (figure 4.8 (a)). The channel is then removed from the mould and holes are punched into the channel to create an inlet and outlet. It is subsequently plasma oxidized at 50 W for 20 minutes (figure 4.8 (b)). Plasma oxidation causes free radicals to be created which helps in creating strong covalent bonds with molecules on surfaces. However, due to limitation of the equipment, the conditions required to create such bonds is difficult. Alternatively, the channel is partially treated by plasma oxidation and is also given an adhesive layer to create a strong bond between the electrode substrate. The use of the adhesive layer for bonding is known as micro-contact printing. Plasma oxidization is carried out of the channel in order to ensure that there is good contact between the edges and the layer. The adhesion material used is PDMS glue and its mixing ratio is 1 part curing agent to 3 parts elastomer. This mixture is then spun onto a surface at 8000 rpm for two minutes to create a thin layer (figure 4.8 (a*)). The oxidized channel surface is then brought into contact with the layer and is left to rest for 15-20 minutes (figure 4.8 (c)).

The electrode substrate is plasma oxidized under the same condition as the microchannel (figure 4.8(b*)). Once this process is completed the channel is removed (figure 4.8 (d)) and attached to the electrode substrate (figure 4.8 (e)), while carefully aligning the edges of the channel to enclose all the electrodes. The sample is then heated at 80^0C for 10 minutes to allow the PDMS glue to cure onto the substrate. The temperature is then increased to 150^0C where PDMS cures instantly. PDMS glue is then poured around the perimeter of the channel to create a further seal (figure 4.8 (f)).

Inlet and outlet glass tubings of 1.8 mm outer diameter are plasma oxidized at 50 W for 20 minutes (figure 4.8 (g) and (c*)). The tubings are attached to the inlet and outlet of the channel and then are heated at 150^0C for 5 minutes. PDMS glue is poured around the outer edge of the glass tubings to ensure a stronger contact with the edges of the channel holes (figure 4.8 (h)).

4.5 Working Fluid Selection

The working fluid has a significant effect on the stability, durability, and overall performance of ion-drag EHD micropumps. Ideally for EHD pumping the working fluid should have a high dielectric constant as the electric body force generated is proportional to it. The fluid should have a low viscosity so that wall shear stress is reduced. Based on Walden's rule (Bockris and Reddy, 1998) viscosity is inversely proportional to the ionic mobility. Higher ionic mobility will cause charges to move a lot quicker, which will make the pump breakdown voltage to be lower. In addition a low conductivity will result in a better efficiency of the pump. A summary of fluid properties of commonly available fluids are given in table 4.3.

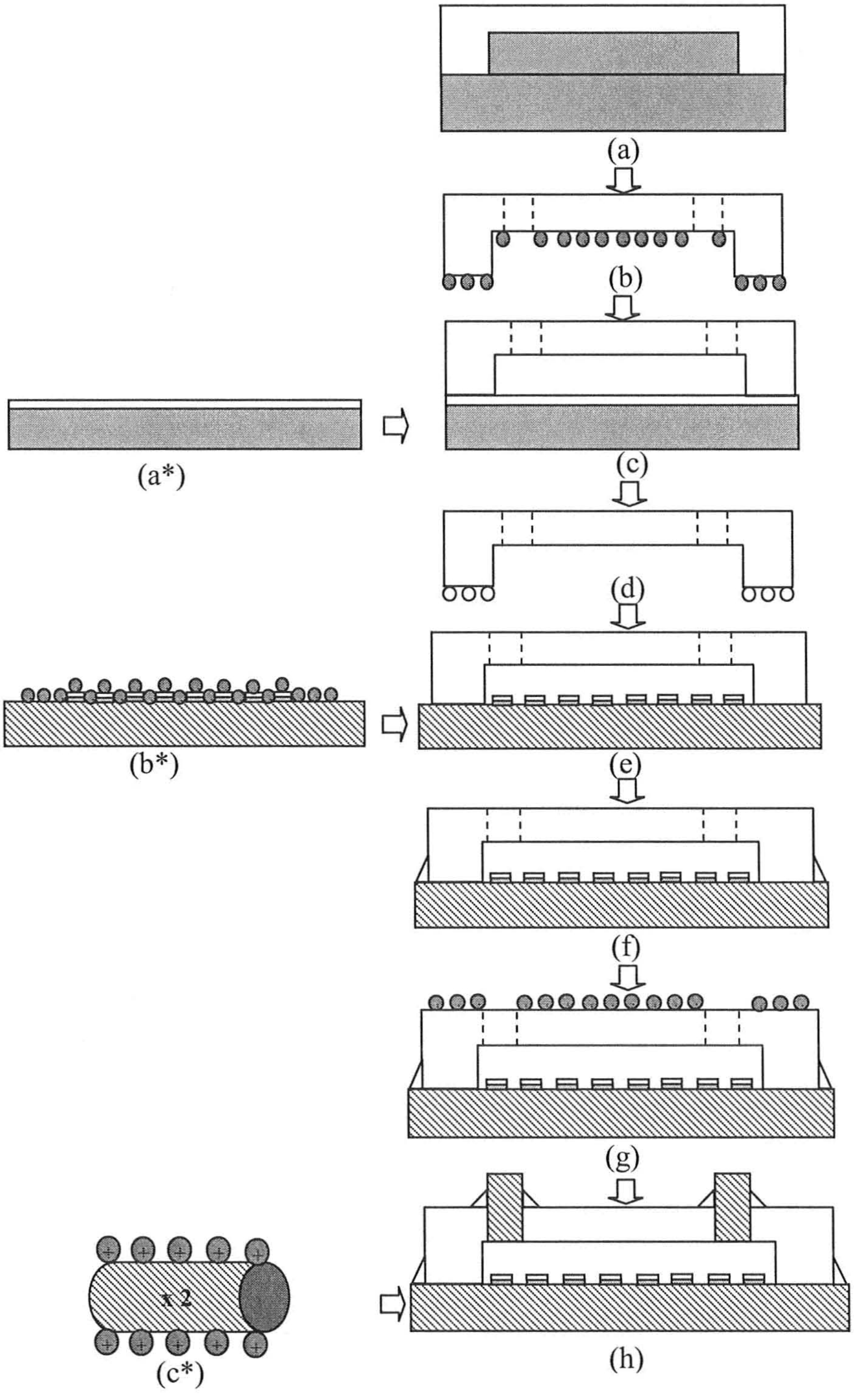

Figure 4.8: Process flow for channel and electrode substrate integration

HFE-7100 (Methoxynonafluorobutane) manufactured by 3M® is selected as the working fluid for this study. It is a low conductivity fluid with a low viscosity while having a relatively high dielectric constant. It is clear, non-flammable, and has a weak odour with the chemical formula of $C_4F_9OCH_3$. Primarily it is used as an industrial refrigerant and is preferred as it is more environmentally friendly when compared to CFCs. Figure 4.9 shows the molecular structure of HFE-7100.

Properties	**Water**	**Ethanol**	**R-123**	**HFE-7100**
Density (kg/m^3)	1000	798	1464	1480
Dynamic Viscosity (mPa.s)	1	1.2	0.409	0.651
Boiling Point (^{0}C)	100	78.3	27.8	61
Molecular Weight (g/mol)	18	46	152.9	250
Thermal Conducivity (W/m.K)	0.595	0.14	0.077	0.069
Specific Heat (kJ/kg.K)	4.184	2.845	1.035	1.18
Heat of vaporization (kJ/kg)	2260	855	229.6	111.6
Dielectric Constant	80	25.8	4.5	7.39
Ionic Mobility (m^2/V.s)	2.08e-8	1.70e-6	1.46e-8	1.31e-8

Table 4.3: Properties of commonly used fluids in EHD micropumps

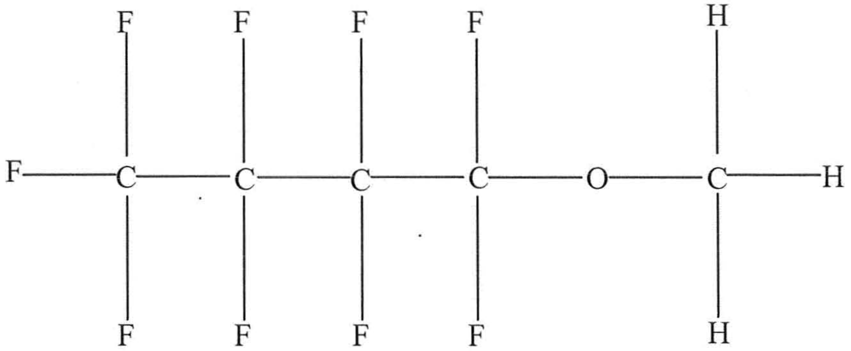

Figure 4.9: Molecular structure of HFE-7100

4.6 Conductive Agent

One of the common problems with EHD micropumps is the rapid degradation in the pump performance. In previous work the pumps operated for approximately 10 hours, while significant current decay was observed after 4 hours (Benetis 2005). The deterioration in the performance was attributed to degradation of the working fluid, HFE-7100, since the electrodes were found to be intact. HFE-7100 decomposes to form bi-products such as Hydrogen Flouride (HF) and Perfluoroisobutylene (PFIB), under elevated temperature conditions. Although the condition inside the pump is assumed to be isotropic, little is known about its electrochemical behavior. Interaction with moisture and other impurities in the atmosphere can result in the loss of dielectric strength of the fluid.

A possible solution is to dope the HFE-7100 with a conductive agent. This will reduce the dependency of charged species to be introduced from the electrode surface through corona discharge. Some of the agents available to use and their properties are shown in table 4.4.

Conductive Agent	Type	Form	Conductivity (S/cm)	Density (Kg/m^3)	Molar Mass (g/mol)	Molecular Formula
Nickel	Nanoparticles, <100 nm	Powder, black	1.43×10^5	8900	58.71	Ni
Carbon	Nanoparticles, <100 nm	Powder, black	727.27	336	12.01	C
Ferrocene	Compound	Powder, orange	6×10^{-3}	2690	186.04	$Fe(C_5H_5)_2$
Pottasium Ferrocyanide	Compound	Powder, white	$\approx 10^{-7}$	1850	368.35	$K_4Fe(CN)_6$

Table 4.4: Conductive agents and corresponding properties

Out of the conductive agents shown in table 4.4, only Ferrocene dissolves homogenously into HFE-7100. Therefore, Ferrocene was selected as the conductive agent. Ferrocene is an organometallic compound with a molecular structure comprising of Iron (Fe) in the centre bounded by two cyclopentadienyl ($C_5H_5^-$) rings as shown in figure 4.10. Compounds with such structure are known as 'Sandwich' compounds. One of the unique characteristics of the Ferrocene molecule is its ability to lose electrons without destroying the molecular bond. When an electric field is applied the Ferrocene undergoes a redox reaction to Ferrocenium (Zanello, 2003):

$$Fe(C_5H_5)_2 \leftrightarrow \left[Fe(C_5H_5)_2{}^+ \right] + e^- \qquad \text{[Eq. 4.2]}$$

The charged Ferrocenium molecule is then caused to move in the direction of the applied electric field, and hence the ion-drag process is caused by an electrochemical process rather than charge injection into the HFE-7100 molecule. In this study the effect of Ferrocene doped into HFE-7100 by 1%, 2%, and 5% by weight is investigated.

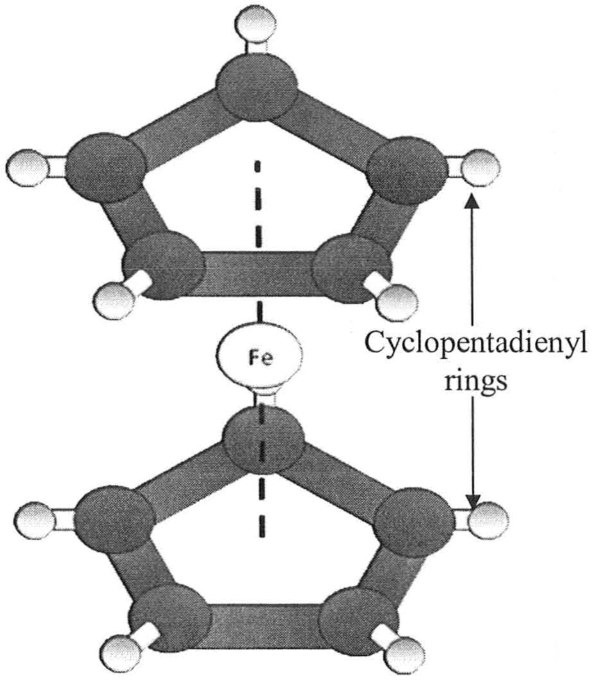

Figure 4.10: Molecular structure of Ferrocene

Two types of current response occur in a redox reaction (Cazes and Ewing 2005), one of which is known as the Faradaic current. This occurs at the interface between the electrode and the hetrogenous liquid solution electrons are transferred via the redox process. Faradaic current is achieved when a certain potential is applied to overcome the activation energy required to cause the reaction. However, the Faradaic current is not constant and decreases over time, as the reactant is consumed at the electrode surface and causes concentration polarization. Mass-transport of Ferrocene due to the migration of Ferrocenium allows more reactant to be present at the surface. As this is also consumed the current will decay to zero. The other is known as the non-Faradaic, or

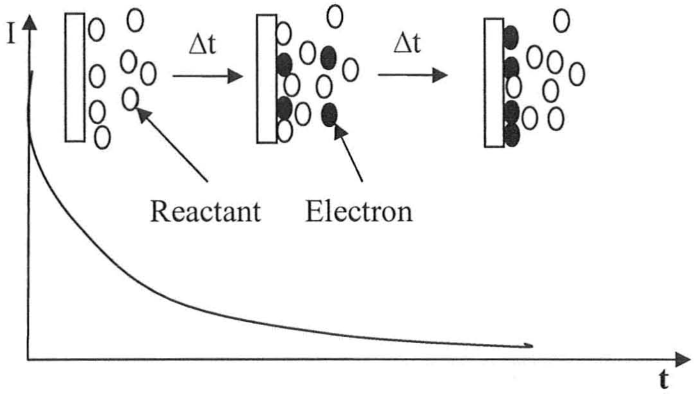

Figure 4.11: Current vs. Time response in the redox process

charging current. This contributes to the overall current response in the system. Non-Faradaic current occurs due to the rearrangement of ions in the solution to compensate for the charge development at the electrode surface. This also eventually decays with time due to the saturation of charge at the electrode surface, due to the Faradaic current. This saturation is referred to as charge polarization. Figure 4.11 shows an Illustration of the Faradic process.

4.7 Summary

In this chapter the rationale is provided for the selection of the geometric configuration of the micropump, the selection of material for the fabrication of the pump, along with the working fluid and the corresponding conductive agent. An asymmetric planar electrode pump geometry with the inter-electrode spacing of 40, 80, and 120 microns is selected for the investigation. The microfabrication process is done in three stages: (1) electrode development, (2) channel development, and (3) electrode substrate-channel integration. The electrodes are fabricated using Gold with Chromium as the adhesive layer between the Glass and Gold. HFE-7100 is used as the working fluid. It is a clear, low odour fluid, with a low viscosity, and high dielectric strength. Ferrocene is an organo-metallic compound that is used as the conductive agent. Other conductive agents that were considered were Nickel nanoparticles, Carbon nanoparticles, and Pottasium Ferrocyanide. However, none of them were able to diffuse properly into HFE-7100, except for Ferrocene.

Chapter 5: Experimental Results and Discussion

5.1 Introduction

In this chapter the results from the experiments with HFE-7100 doped with Ferrocene are presented and discussed. Micropumps with asymmetric planar electrode configuration are used in this investigation with inter-electrode spacings of 40, 80, and 120 microns. The characteristics of the pump are presented in terms of back pressure generation, and the current-voltage characteristics. The results are also compared to previous investigations using pure HFE-7100 as the working fluid. The pump performance under an applied DC voltage and pulse voltage is presented. The effect of pulse repetition rate, duty cycle, and amplitude on the performance are presented and discussed.

5.2 Experimental Facilities and Procedure

The DC steady voltage was applied using a Keithley 2410 power supply. The leads from the power supply were connected to the base of the pump electrodes via copper wires which had been soldered onto it. The power supply has a source range of 1 μV to 1100 V and a current range of 10 pA to 1 A. The inlet and outlet glass tubings of the micropump are attached to two Tygon® plastic tubings that are held vertical. The working fluid is filled into the channel and the tubings to a sufficient height so that the meniscus can be viewed at eye level. The fluid height in the tubings is checked to be equal to ensure that there is no pressure influencing the fluid by trapped bubbles. Any pressure difference results in a height difference at the liquid interfaces in the two tubings. The height difference is measured using a height gauge with an uncertainty ± 0.02 mm which corresponds to ± 0.29 Pa. A schematic of the test set-up is shown in Figure 5.1.

The pulse voltage was applied using a function generator (Tektronix AFG-3022B). The voltage output from this device is 10V peak to peak and can provide a maximum frequency of 25 MHz. The voltage output from the function generator is amplified using a voltage amplifier (Trek 677B) where the maximum gain is 400V/V. A Keithley 2636 source-measure unit is used to measure the current via a data acquisition system. Figure 5.2 shows a circuit diagram of the experimental set-up. The pressure is measured the same way as mentioned in the test set-up for the DC voltage case and are taken at different time intervals to account for any variation due to the changing potential. The effect of the different independent parameters of the pulse voltage on the pump performance was determined. The parameters that were changed are the voltage value at both high (V_H) and low (V_L) values, the duty cycle (D_C) which is the percentage of time that V_H is applied over one cycle, and the pulse repetition rate (*f*). A schematic of the pulse voltage with the defined parameters are shown in Figure 5.3.

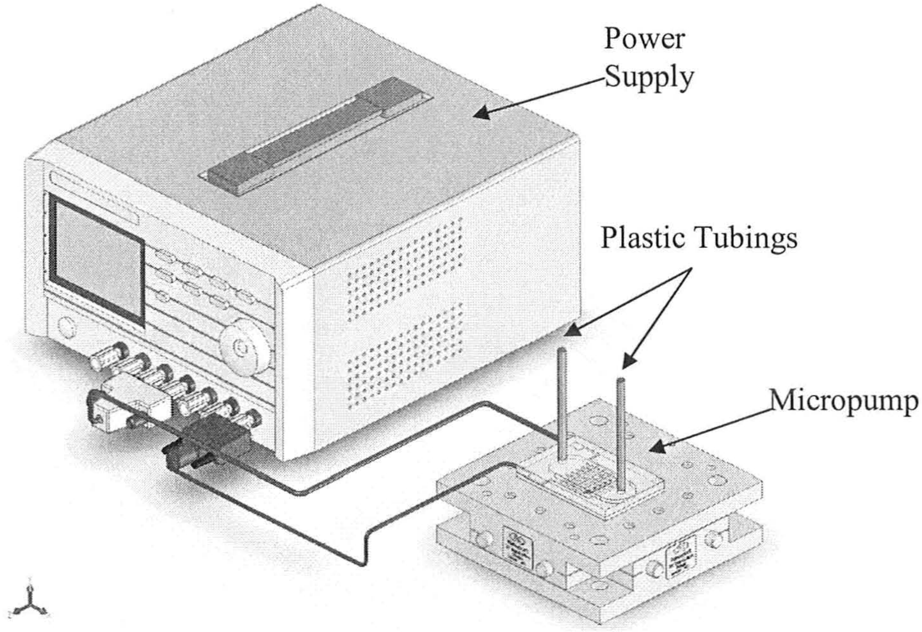

Figure 5.1: Experimental Set Up for Constant Voltage

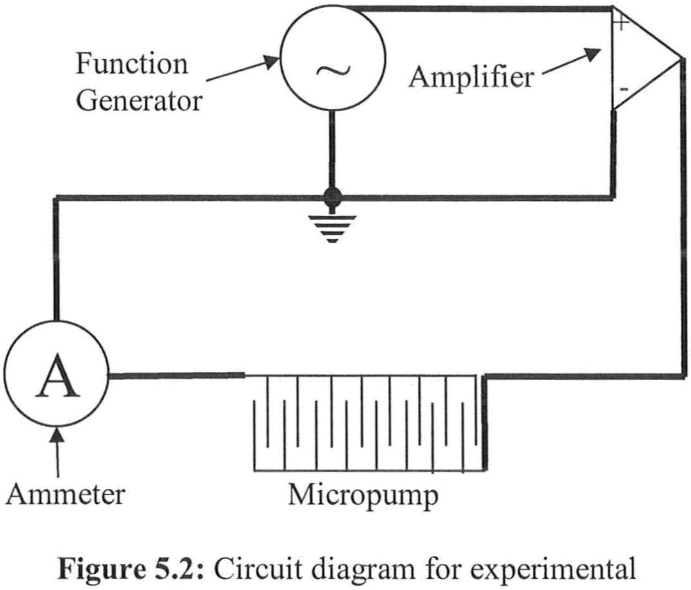

Figure 5.2: Circuit diagram for experimental set-up with voltage waveform

Test #	**1**			**2**			**3**			**4**		
Pump	**f (Hz)**			**D_c (%)**			**V_L**			**V_H**		
A-40	0.005	0.5	V_H=500V	20	60	V_H=500V	400	0	V_H=500V	500	700	V_L=400V
	0.01	1	V_L=400V			V_L=400V	300	-100	f=Test #1			f=Test #1
	0.05	5	W_p=50%	40	80	f=Test #1	100	-	W_p=Test #2	600	800	W_p=Test #2
	0.1	-										
A-80	0.005	0.5	V_H=600V	20	60	V_H=600V	500	0	V_H=600V	600	800	V_L=500V
	0.01	1	V_L=500V			V_L=500V	400	-100	f=Test #1			f=Test #1
	0.05	5	W_p=50%	40	80	f=Test #1	200	-	W_p=Test #2	700	900	W_p=Test #2
	0.1	-										
A-120	0.005	0.5	V_H=700V	20	60	V_H=700V	600	0	V_H=700V	700	900	V_L=600V
	0.01	1	V_L=600V			V_L=600V	500	-100	f=Test #1			f=Test #1
	0.05	5	W_p=50%	40	80	f=Test #1	300	-	W_p=Test #2	800	1000	W_p=Test #2
	0.1	-										

Table 5.1: Test Matrix for Pulse Voltage

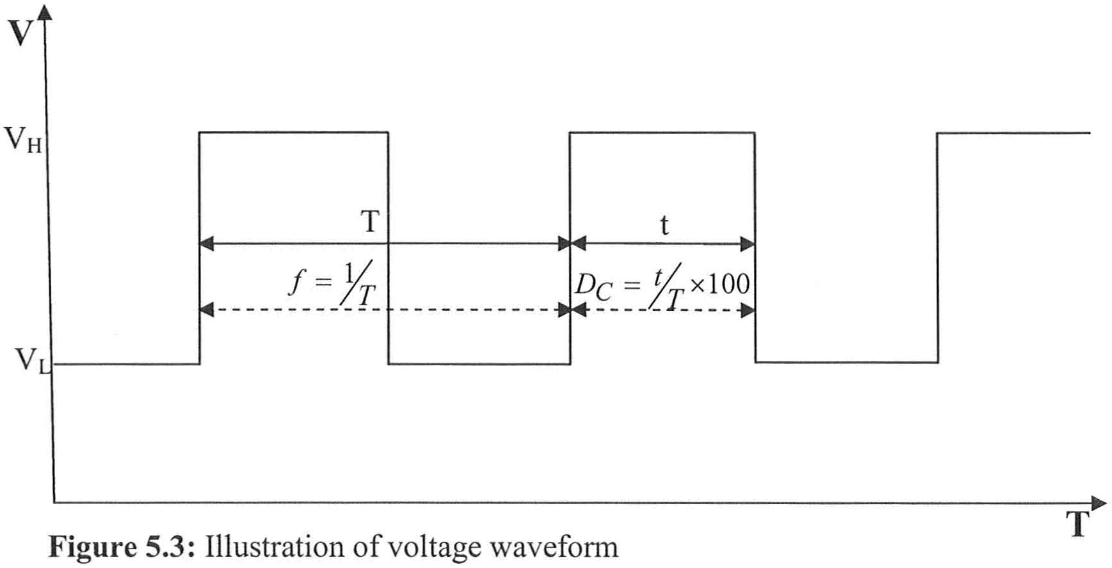

Figure 5.3: Illustration of voltage waveform

The range of the test parameters for the three different pump configurations A-40, A-80, and A-120, are shown in table 5.1. The range for the pulse repetition rate was determined by estimating the charge relaxation factor (τ_C) and the limitation of the sampling rate of the data acquisition system. The charge relaxation factor indicates the time required for the charges to reach equilibrium and is calculated as:

$$\tau_c = \frac{\varepsilon_o \varepsilon_r}{\rho_r} \quad \text{[Eq. 5.1]}$$

where ε_o, ρ_r are the permittivity of free space and resistivity of the fluid. Since little is known about the electrical properties of HFE-Ferrocence, this factor was calculated for pure HFE-7100. The value was calculated as 21 seconds, which corresponds to a pulse repetition rate of 0.05 Hz. Hence the pulse repetition range was set from 0.005 Hz, which is 10 times slower than the rate for the relaxation period, to 5 Hz which equates to 100 times faster. The voltage amplitude for each configuration was determined based upon the charge injection voltage and the voltage breakdown threshold, as seen with HFE-7100 (Kazemi, 2009). A smaller inter-electrode spacing results in a lower breakdown voltage. However, a higher current and pressure is achieved in comparison to larger inter-electrode spacing for the same applied voltage. A negative offset voltage was also studied to determine if this would help convert more Ferrocenium into Ferrocene, hence giving a better current performance.

Even though a pulse waveform allows control of different parameters, there are certain limitations with its application. Firstly, the time constant (τ) associated with ramping up and ramping down the voltage will result in a waveform as illustrated in figure 5.4. However, if the time constant is significantly faster than the duration that the potentials are being applied then this factor can be neglected. This was determined from the slew rate, which was found to be 15V/μs. There is a displacement current associated with an applied pulse voltage (Siegel, 1991). This is caused by the time variation of the electric field, rather than charge motion. Due to the step changes in the applied potential, the displacement current can be significant but for a very short duration. If this was current caused by charge motion, the pressure generation would be significantly high. To evaluate the magnitude and confirm the presence of displacement current a fixed resistor is placed in series with the micropump as shown in figure 5.5.

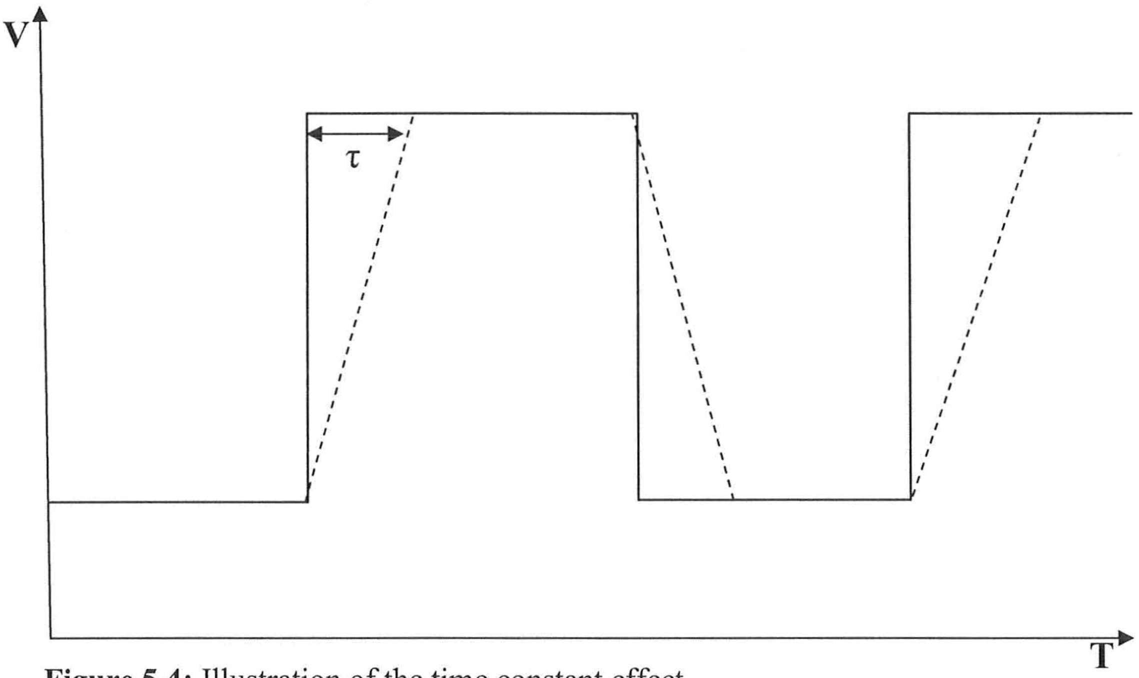

Figure 5.4: Illustration of the time constant effect

An Agilent 54624A oscilloscope was connected in parallel to record the voltage across the resistor with a sampling rate up to 100 MHz. The current traces recorded by the oscilloscope for both an applied pulse and sine wave are shown in figure 5.6. For the applied pulse voltage, sudden spikes in the current are observed at the step changes in the voltage. The current spikes are not observed when the sine waveform is applied, which suggests that the spikes are due to displacement current rather than charge motion.

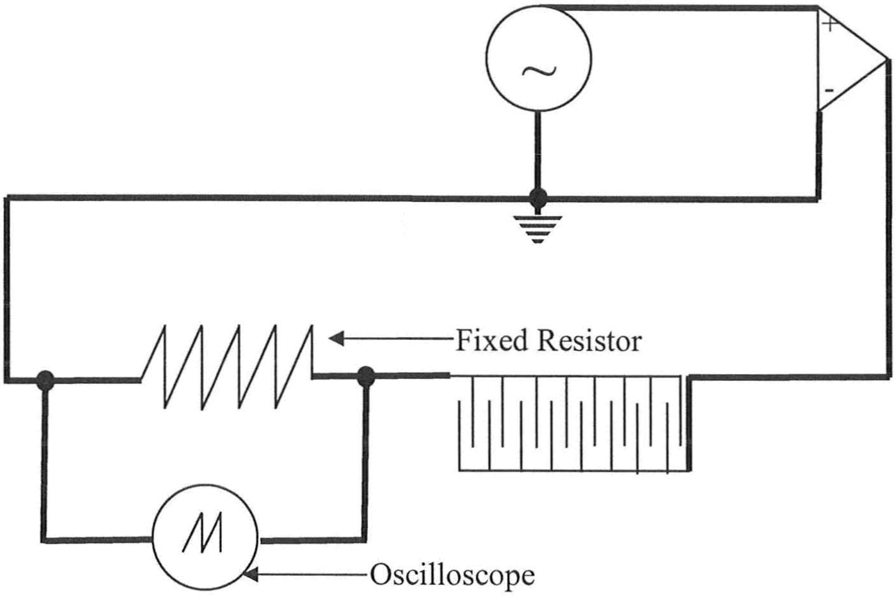

Figure 5.5: Circuit diagram for experimental set-up to capture displacement current

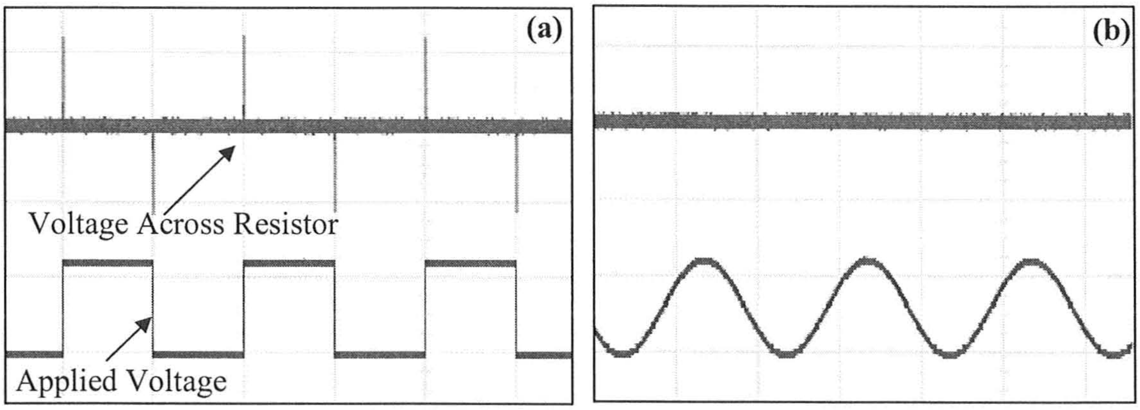

Figure 5.6: Voltage trace across resistor by applying (a) square (b) sine waveform signal.

5.3 Results and Discussion

Applied DC Voltage

The results obtained with HFE-Ferrocene at 1% concentration by weight, was compared with the performance obtained with HFE-7100 by Kazemi et al. (2009a) for the same pump configuration. The variation in the pressure with the applied voltage for HFE-Ferrocene and HFE-7100 is shown in figure 5.7 for A-80. The corresponding voltage-current characteristics are shown in figure 5.8 (a) and (b). The pressure generated with HFE-Ferrocene is significantly higher than with HFE-7100 for the same applied voltage. A maximum pressure of 871 Pa was generated at 400V with HFE-Ferrocene, compared to 114 Pa with HFE-7100 for the same applied voltage. At 400V, a current of 5.1 μA was obtained with HFE-Ferrocene, while with HFE-7100 this current was achieved only at 700V. For this particular configuration it is thought that charge injection into HFE-7100 due to corona discharge occurs at around 400V as that is where a non-linear rise in current is observed with the increase in applied voltage. However, with HFE-Ferrocene current is seen at voltages as low as 1V (figure 5.8 (b)) which suggests that the presence of charged species is caused by the electrochemical behavior of Ferrocene, rather than charge injection due to corona onset.

Although the pressure generation with HFE-Ferrocene is better, it is difficult to sustain this at higher voltages. This is due to the decrease in the current that occurs over time as shown in figure 5.9. There are three possible reasons for the decrease. The first one could be due to the depletion of Ferrocene as the solution becomes saturated with Ferrocenium and no new charged species are formed. In order to evaluate this, Faraday's law of electrolysis is used to determine the time that is required to deplete the amount of Ferrocene present in the microchannel. This is estimated as:

$$n = \left(\frac{It}{F}\right)\left(\frac{1}{z}\right) \qquad \text{[Eq. 5.2]}$$

where n, I, F, t, and z represent the number of moles of Ferrocene, current, Faraday's constant (96485 $\mathrm{C.mol^{-1}}$), time, and the valency of electrons from the reaction. From equation 5.2, the time is estimated at over 24,000 seconds. Therefore, this suggests there is still sufficient Ferrocene present in the working fluid for the time duration of the experiment. The second possibility is the diffusion of the Ferrocenium. As Ferrocenium that is produced near the electrode moves into the bulk liquid due to its opposing polarity a concentration gradient is created (Cazes and Ewing, 2005) and Ferrocene near the electrode decreases. The diffusion layer is defined as the distance from the electrode where the concentration of Ferrocene is equal to that in the bulk solution. The current decreases as the diffusion layer grows as it is inversely proportional to it. To determine the time that is required for the diffusion layer to be established in the entire channel, Cottrell's equation is used.

$$I = zFAD^{1/2}\frac{C_A^{\delta}}{t^{1/2}} \qquad \text{[Eq. 5.3]}$$

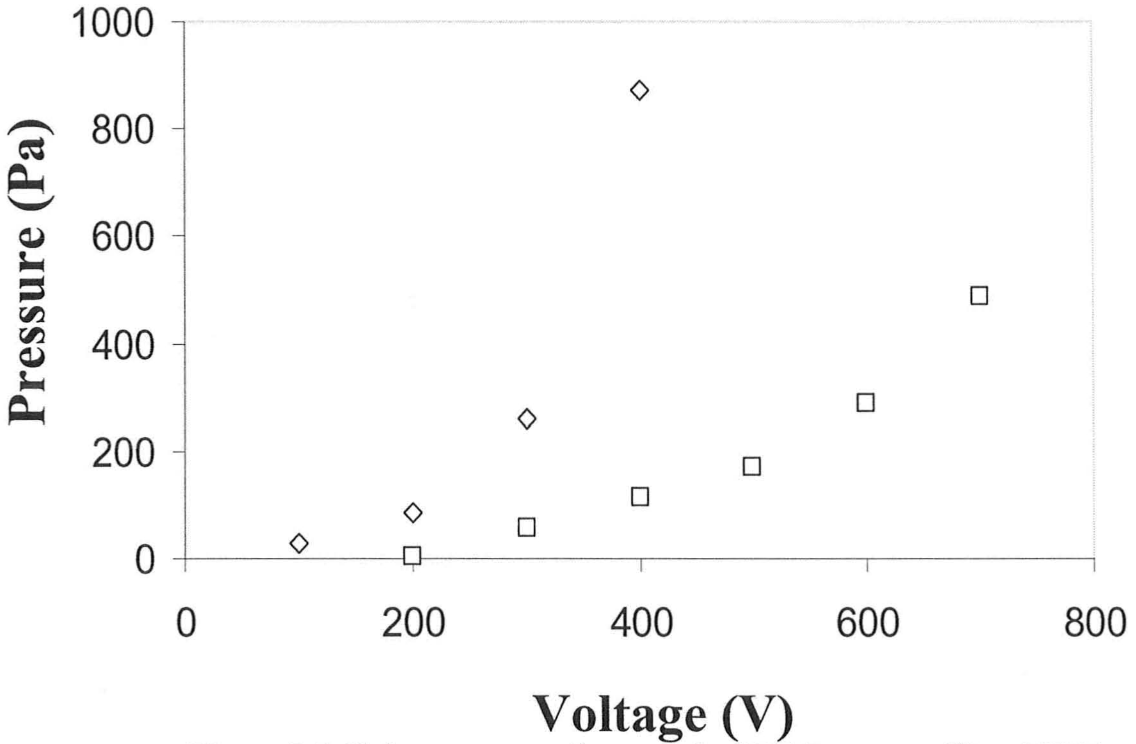

Figure 5.7: Voltage versures Pressure for HFE-Ferrocene (◊) and HFE-7100(□) from work of Kazemi (2009) for A-80.

where *A, D,* and C_A^{δ} represent the surface area of the electrodes, diffusion coefficient, and concentration. At peak current it can be assumed that there is uniform concentration. The diffusion coefficient for Ferrocenium was found to be 2.35x10^{-5} cm^2.s^{-1} (Olsen and Tallman, 1994). The concentration of Ferrocene in A-80 was calculated using the molar mass of Ferrocene (186 g.mol^{-1}) and the dimensions of the microchannel. The concentration was estimated to be 7.95x10^{-5} mol.cm^{-3}. The time required for the diffusion layer to be established in the entire micropump was estimated to be in the order of 10^7 seconds. This far exceeds the elapsed time of the experiment and can also be ruled out as a factor.

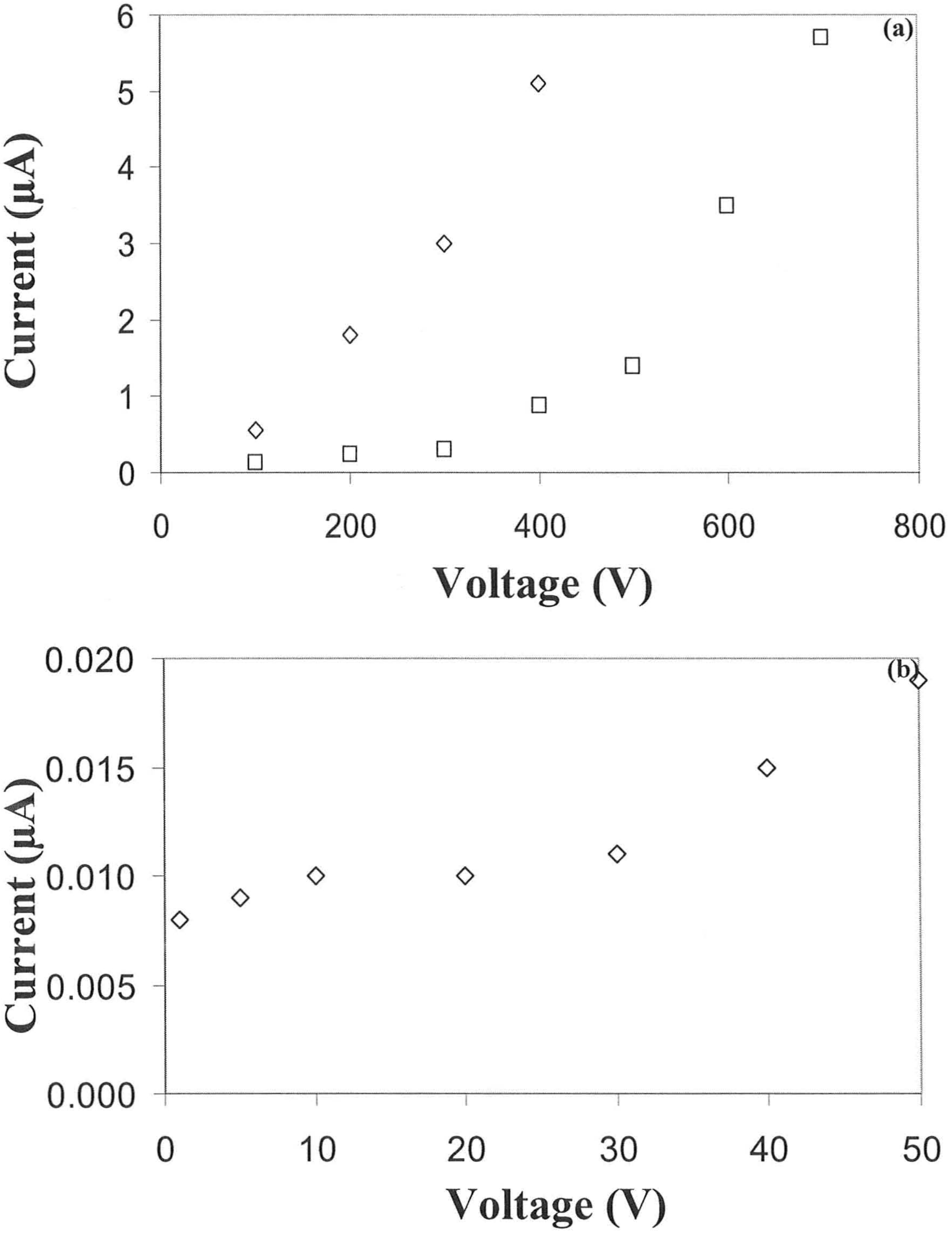

Figure 5.8: Voltage versus Current at (a) High Voltage and (b) at Low Voltage for HFE-Ferrocene (◊) and HFE-7100 (□) from work of Kazemi (2009) for A-80.

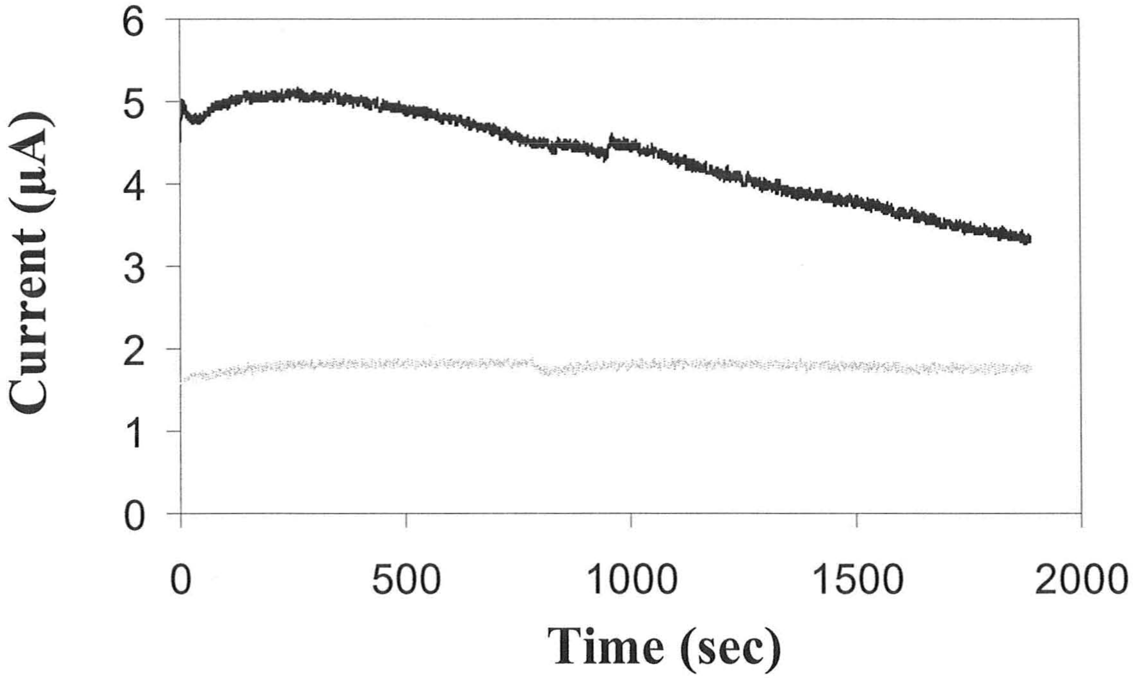

Figure 5.9: Current vs. Time at 200V (▨) and 400V (■) for A-80.

The final possibility can be that since charge injection from the electrode for A-80 occurs around 400V, that the HFE-7100 molecules are ionized. The ionized HFE-7100 molecules will have an opposing charge polarity to the Ferrocenium molecule, and hence the direction of migration will be different. Initially the current is high to due to the conversion of Ferrocene to Ferrocenium. However, as the potential is applied for longer durations the existence and migration of bipolar charged species occurs resulting in a fall in the net current and pressure generation. A possible solution to address this issue is to use pulse voltage, where the potential is applied for short durations and will reduce the probability of charge injection to be initiated.

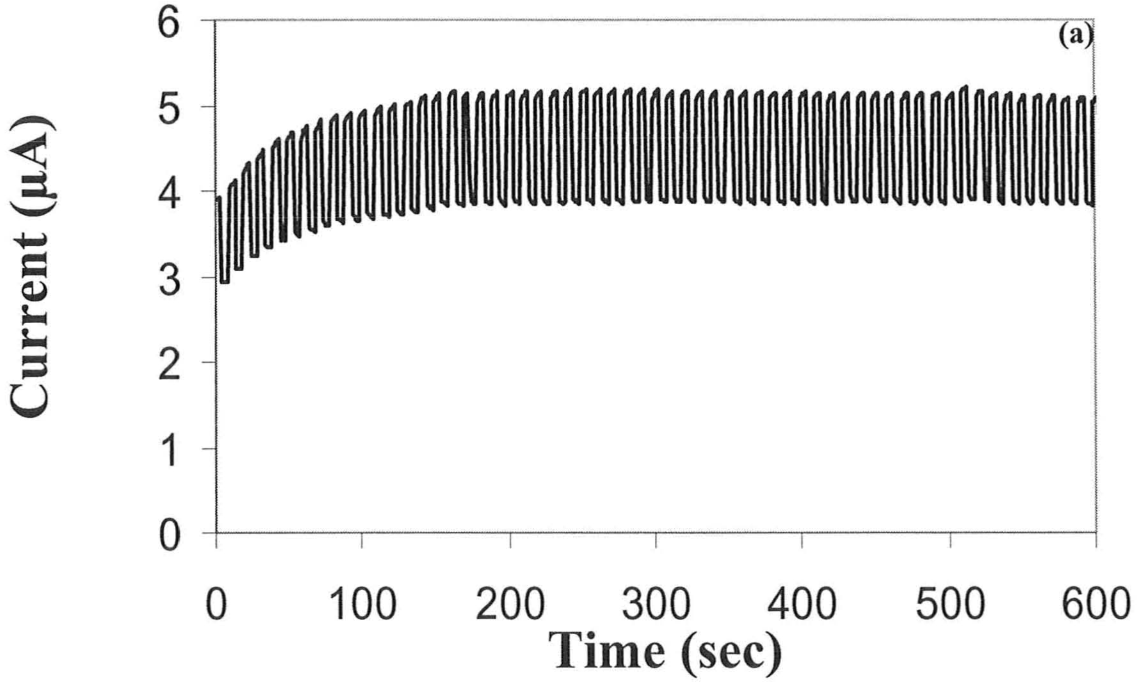

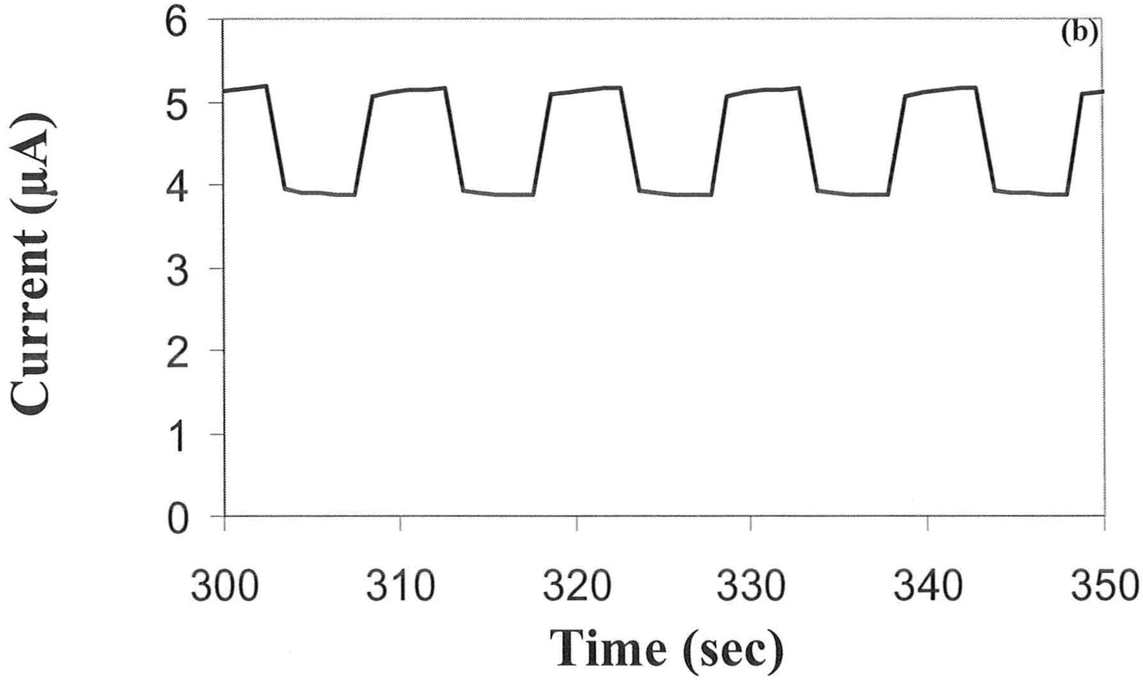

Figure 5.10: (a) Current-Time trace for A-80 at voltage amplitude 500V to 600V, pulse width of 50%, and frequency of 0.1 Hz. (b) section of trace.

Applied Pulse Voltage

In this section the use of pulse voltage in addition to Ferrocene is investigated to overcome current decay. A typical current trace with time for an applied pulse voltage of 500V to 600V, duty cycle of 50%, and pulse repetition rate of 0.01 Hz is shown in figure 5.10 (a) . An expanded section of the trace from 300 to 350 seconds is shown in figure 5.10 (b). Additional sample traces are given in appendix B. The parameters of interest for this study are the effective current (I_{eff}) which represents the mean, the minimum (I_{min}) and maximum current (I_{max}), variation in the initial and final effective current (ΔI), and root mean square current (I_{rms}) which represents the deviation from I_{eff}..

The effect of pulse repetition rate on the pressure generation for a pulse voltage of 400V to 500V for A-40, 500V to 600V for A-80, and 600V to 700V for A-120, at 50% duty cycle is shown in figure 5.11. Different applied voltages were used for each configuration to avoid breakdown as with smaller inter-electrode spacing this can occur at lower potentials. The pressure increases from 161 Pa to 234 Pa for A-40, 138 Pa to 156 Pa for A-80, and 65 Pa to 210 Pa for A-120 as the pulse repetition rate is increased from 0.005 Hz to 5Hz. The larger fluctuations in the pressure at the lower pulse repetition rates are likely due to the system response to the applied voltage. At low pulse repetition rates, the pressure generation can respond to the maxima and minima potential as these are sustained for longer periods. At the higher pulse repetition rates the system pressure generation can not respond to the alternating high and low voltages.

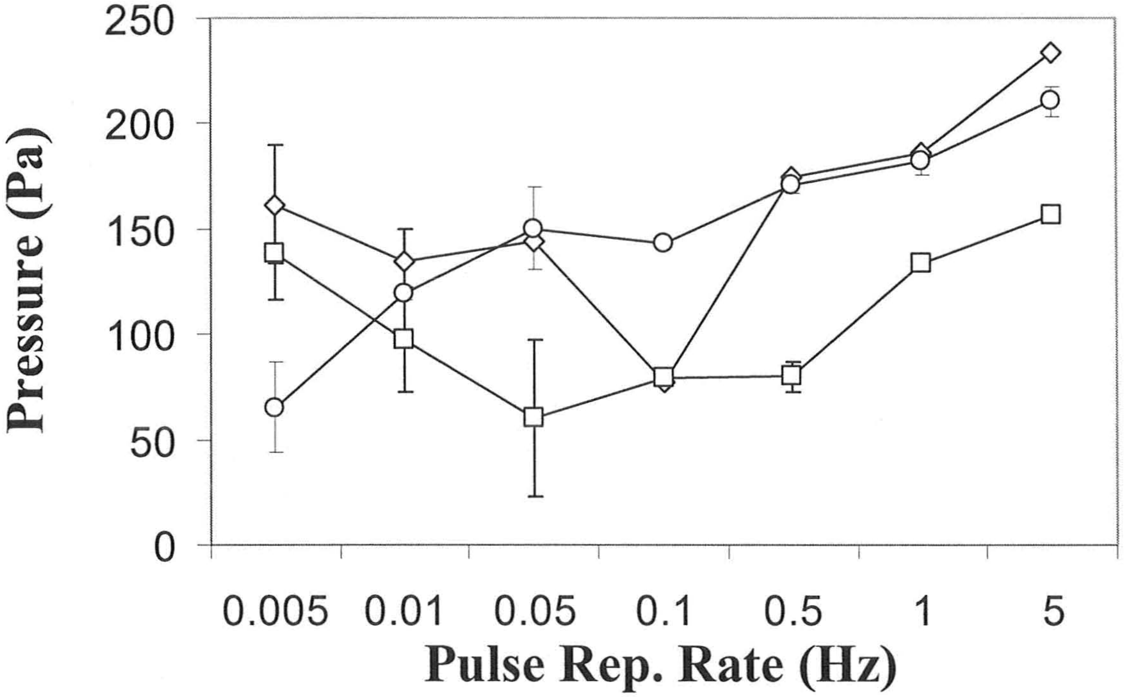

Figure 5.11: Pulse repetition rate effect on back pressure for A-40 (◊), A-80 (□), A-120 (○).

The effect of pulse repetition rate on the I_{eff}, I_{min}, I_{max}, and ΔI is shown in figure 5.12. The effective voltage is calculated to be the same as the pulse repetition rate is increased (figure 5.12 (a)). There is a decrease in I_{eff} with an increase in pulse repetition rate for A-40, while it increases for A-80 and A-120 (figure 5.12 (b)). This is because there is an amplitude variation in the initial period of the tests. This results in different I_{max} to be obtained (figure 5.12 (c)). For A-40 an I_{max} of 30 μA was obtained at 0.005 Hz. For A-80 and A-120 an I_{max} of 16.9 μA, and 1μA was achieved at 5 Hz. However, for other pulse repetition rates the amplitude variation is not as significant which results in a stable current signal. The ΔI is a measure of the difference in the effective current associated to the first and last cycle of the pulse voltage. Figure 5.12 (d) shows the ΔI calculated for different pulse repetition rates.

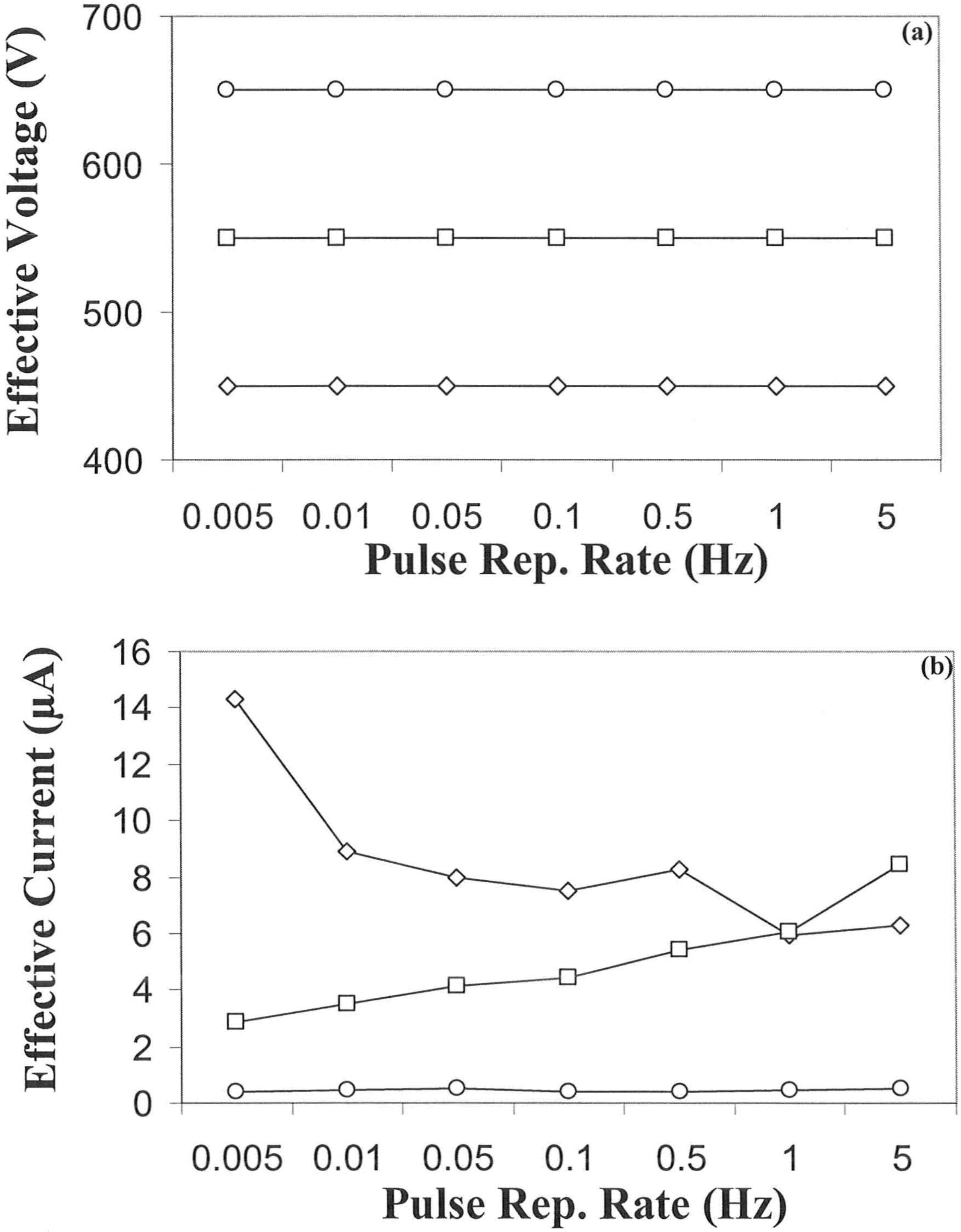
(a)
Effective Voltage (V)
700
600
500
400
0.005
0.01
0.05
0.1
0.5
1
5
Pulse Rep. Rate (Hz)
(b)
Effective Current (μA)
16
14
12
10
8
6
4
2
0
0.005
0.01
0.05
0.1
0.5
1
5
Pulse Rep. Rate (Hz)

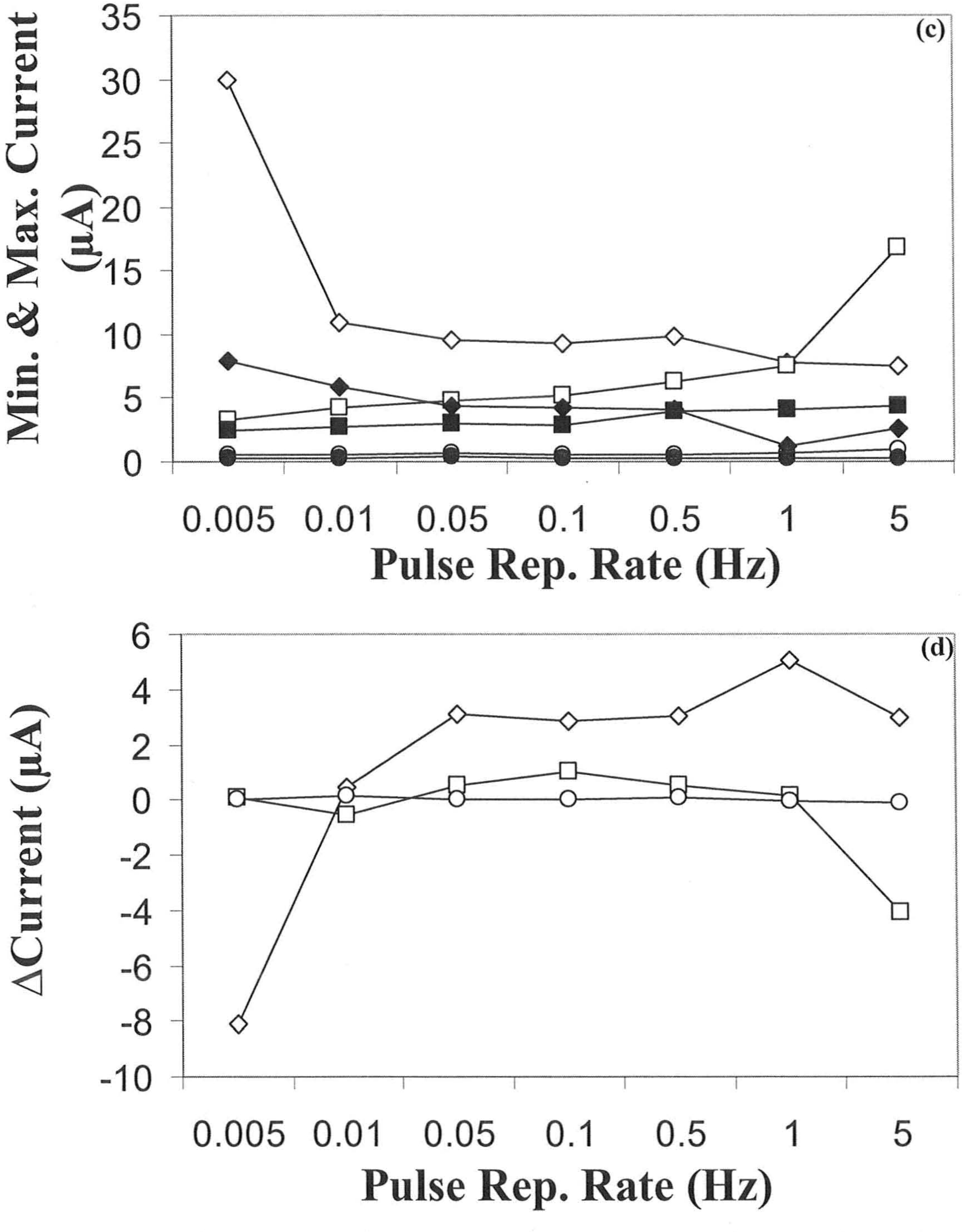

Figure 5.12: Pulse repetition rate effect on (a) Effective voltage, (b) Pressure generation, (c) I_{eff}, (d) I_{min} (filled) and I_{max} (open), and (e) ΔI for A-40 (◊), A-80 (□), and A-120 (○).

It can be seen that ΔI generally remains the same with an increase in the pulse repetition rate. Applying a pulse voltage shows the current amplitude to be sustained, even at low pulse repetition rates. This is because there is a time delay (τ_R) between the applied potential and the charge injection process to initiate which produces ionized HFE-7100 molecules (Shrimpton, 2009). This is represented as:

$$\tau_R = 2T_c \frac{\mu}{\varepsilon E^2} \qquad [5.4]$$

where T_c is a ratio between the stored electrostatic energy and viscous dissipation energy. From the DC voltage case for A-80 it was found that the time required for the current to decay due to charge injection was around 300 seconds for an applied potential of 400V. Even at low pulse repetition rates the system is not given sufficient time to initiate charge injection for the given applied potential. Therefore, Ferrocenium becomes the primary charged species in the fluid domain.

The duty cycle was varied from 20% to 80% for an applied potential of 400V to 500V for A-40, 500V to 600V for A-80, and 600V to 700V for A-120 for a pulse repletion rate of 5Hz. The duty cycle represents the ratio of the duration that the high voltage is applied over one cycle of the pulse voltage. A pulse repetition rate of 5Hz was selected in this instance because the pressure generation was found to be the highest at this pulse repetition rate from the earlier results. The effect of increasing the duty cycle on the pressure generation is shown in figure 5.13.

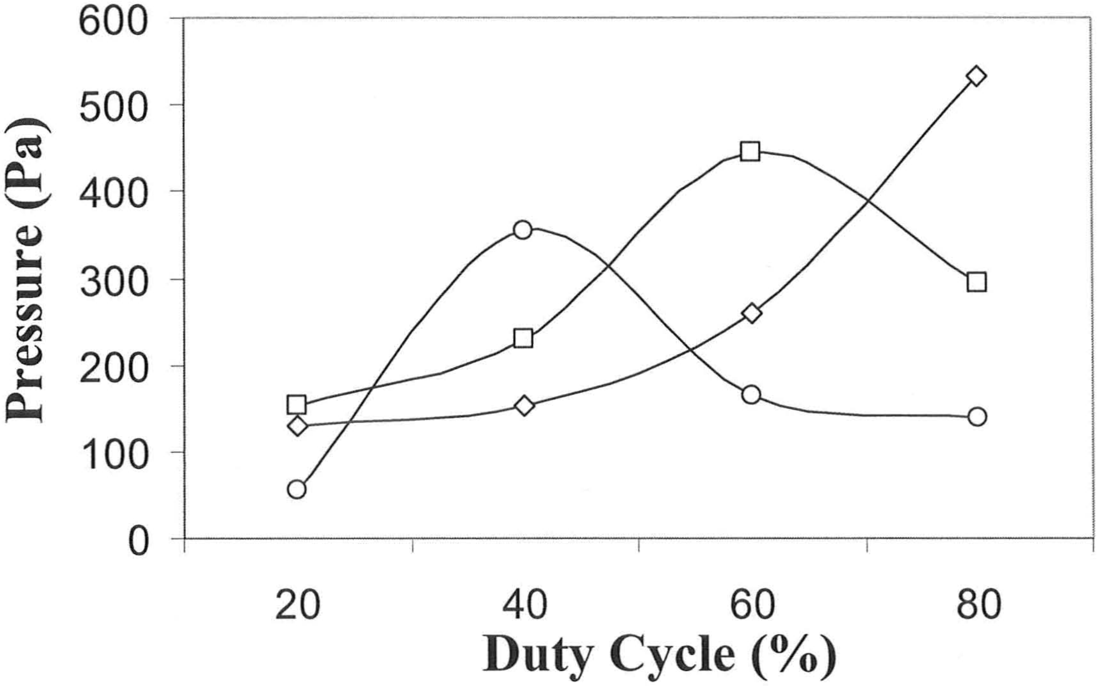

Figure 5.13: Duty cycle effect on back pressure for A-40 (◊), A-80(□), A-120 (○).

For A-40 a maximum pressure of 532 Pa was obtained at 80% duty cycle, for A-80 a maximum of 444 Pa occurred at 60%, and for A-120 a maximum of 354 Pa was generated at 40% duty cycle. Increasing the duty cycle increases the effective voltage (figure 5.14 (a)), since the duration that the high voltage is being applied is increased. However, this will also promote corona discharge at the electrodes which can result in more ionized HFE-7100 molecules being present in the fluid domain. If the transient part of the applied voltage is neglected, then the charge continuity equation reduces to:

$$\nabla . J = 0 \qquad [5.5]$$

where J is the current density. If it is assumed that migration is the dominant component then it is a function of mobility (μ_e), charge density (ρ_e) and the applied electric field (E).

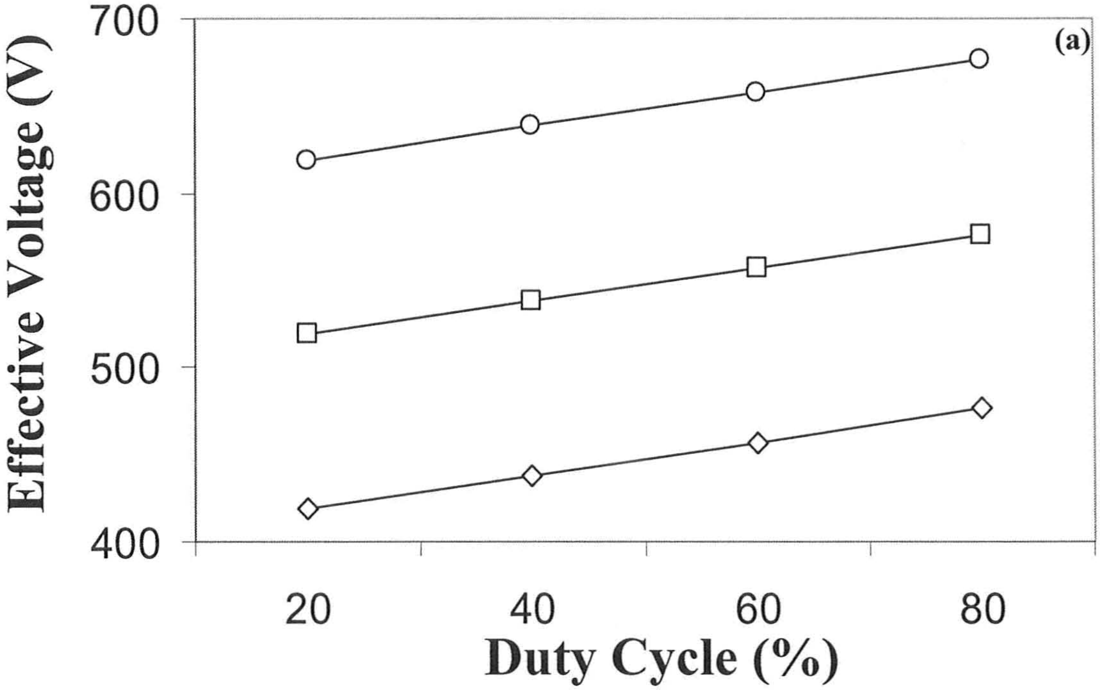
(a)
Effective Voltage (V)
700
600
500
400
20
40
60
80
Duty Cycle (%)

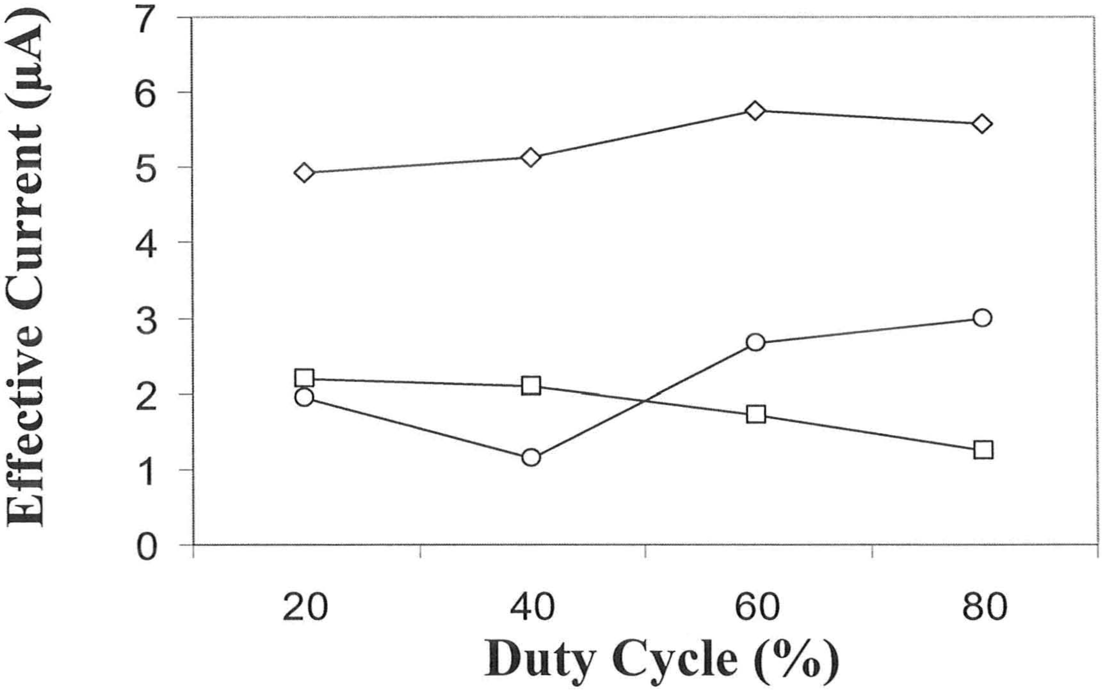
Effective Current (μA)
7
6
5
4
3
2
1
0
20
40
60
80
Duty Cycle (%)

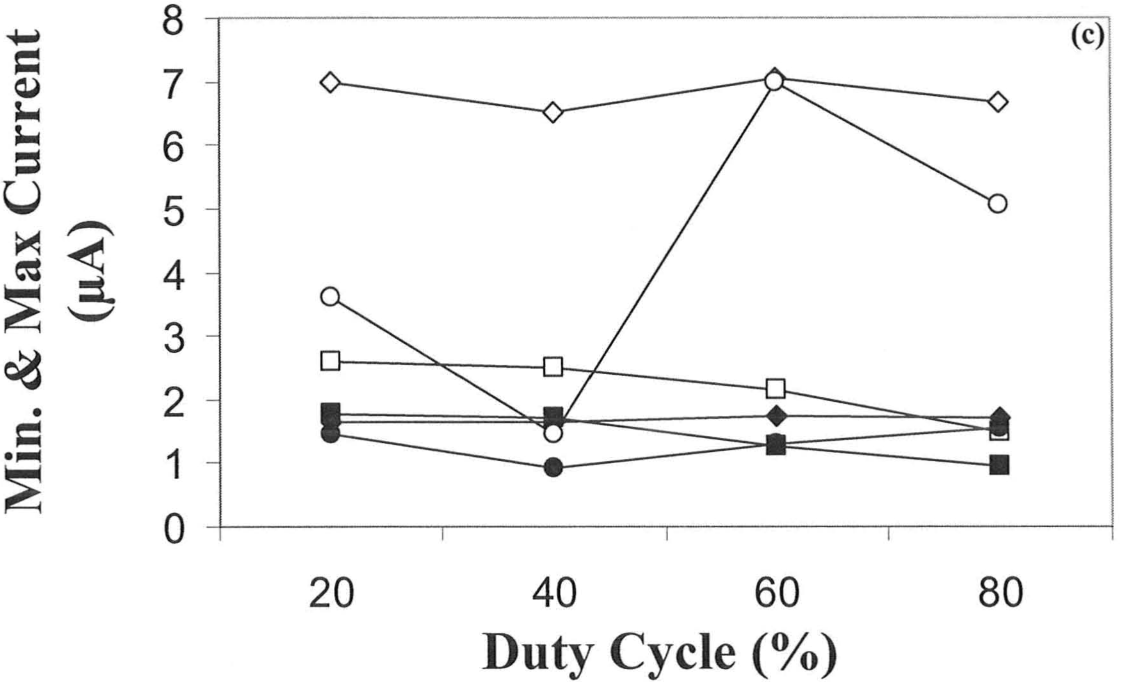

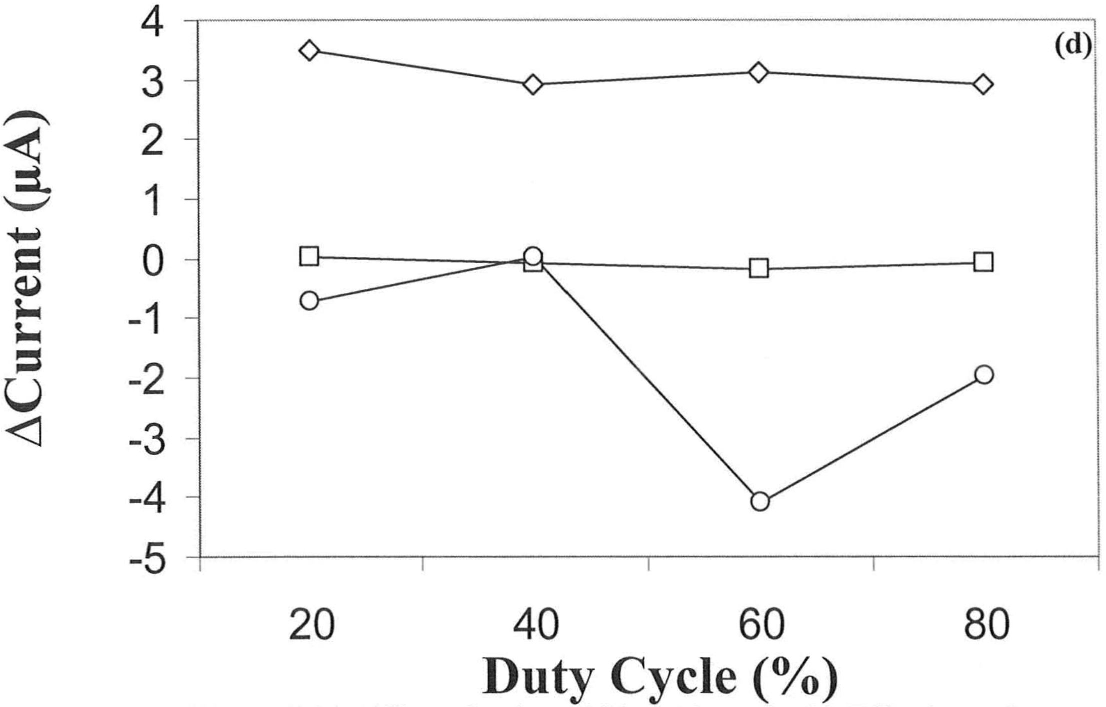

Figure 5.14: Effect of pulse width (W_p) on the (a) Effective voltage, (b) I_{eff}, (c) I_{min} (filled) and I_{max} (open), and (d) ΔI, for A-40 (◊), A-80 (□), A-120 (○).

Equation 5.5 can be simplified for the 1D case as:

$$\nabla . J = \frac{\mu_e \rho_{e2} E_2 - \mu_e \rho_{e1} E_1}{x_2 - x_1} = 0 \qquad \text{[Eq. 5.6]}$$

where x_1 and x_2 represents spatial locations from the emitter electrode along the x-axis. If x_1 represents a location closer to the emitter electrode than x_2, then in order for the condition in equation 5.6 to be satisfied $\rho_{e2} > \rho_{e1}$, since $E_1 > E_2$ through Gauss law. This can only occur if migration of charges takes place. In previous work it has been shown that increasing the duty cycle results in an increase in the eletrophoretic force (Zaharoff and Yuan, 2002; Li, 2005) due to an enhancement in the migration of charges. However, with large inter-electrode spacing there is a more substantial variation in the electric field strength with respect to distance from the emitter electrode. Therefore in order to satisfy equation 5.6 migration of charges would be higher for pump configurations with larger inter-electrode spacing. If the presence of ionized HFE-7100 is promoted with the increase in the duty cycle, bipolar charge migration will occur resulting in a fall in net current and pressure generation. Figure 5.14 (b) shows the I_{eff} for A-80 is decreasing from 2.18 μA to 1.24 μA with the increase of the duty cycle, while for A-40 it remains at approximately 5μA. Therefore, for A-80 there is an optimum duty cycle in which a maximum effective potential and I_{eff} can be achieved to develop the body force, while with A-40 since the current remains the same with the duty cycle then increasing it will result in a higher electrophoretic force. A-120 shows a decreasing I_{eff} from 20% to 40% duty cycle, after which an increase is seen. This is due to the amplitude variation that occurs in the initial periods of the test resulting in a high I_{max} to be obtained (figure 5.14

(c)). However, the high I_{max} is not sustained which leads to a drop in ΔI of -4 μA for 60% duty cycle, and -2μA for 80% (figure 5.14 (d)). At 40% duty cycle the ΔI is at minimal value of 0.03 μA as I_{eff} is maintained at 1.15 μA. Therefore, the 40% duty cycle provides stability in the current, and an effective potential that provides optimum pressure generation.

The effect of the offset voltage was determined for each configuration at a pulse repetition rate of 5 Hz. The duty cycle was set at 80%, 60%, and 40% for A-40, A-80, and A-120. The duty cycles were selected based upon the previous test results which gave the highest pressure generation for the given configuration. The high voltage was maintained at a constant value as in the previous tests. The effect of the offset voltage on the pressure generation is shown in figure 5.15. Each pump configuration shows a decrease in the pressure generation with a reduction in the offset voltage. For A-40 the pressure generation drops from 532 Pa to 325 Pa as the offset voltage is changed from 400V to -100V. The pressure generation for A-80 decreases from 444 Pa to 48 Pa as the offset voltage is decreased from 500V to -100V, while for A-120 it decreases from 354 Pa to 19 Pa for 600V to -100V. With a reduction in the offset value, the effective voltage is reduced (figure 5.16 (a)), which also results in a decrease in I_{eff} (figure 5.16 (b)). Figure 5.16 (c) shows that I_{min} and I_{max} drops from 6.67 μA and 1.69μA to 2.98 μA and -1.42 μA for A-40 as the offset voltage is lowered from 400V to -100V. For A-80, I_{max} remains around 2 μA for offset voltages of 500V to -100V while I_{min} drops from 1.26 μA to -0.73 μA.

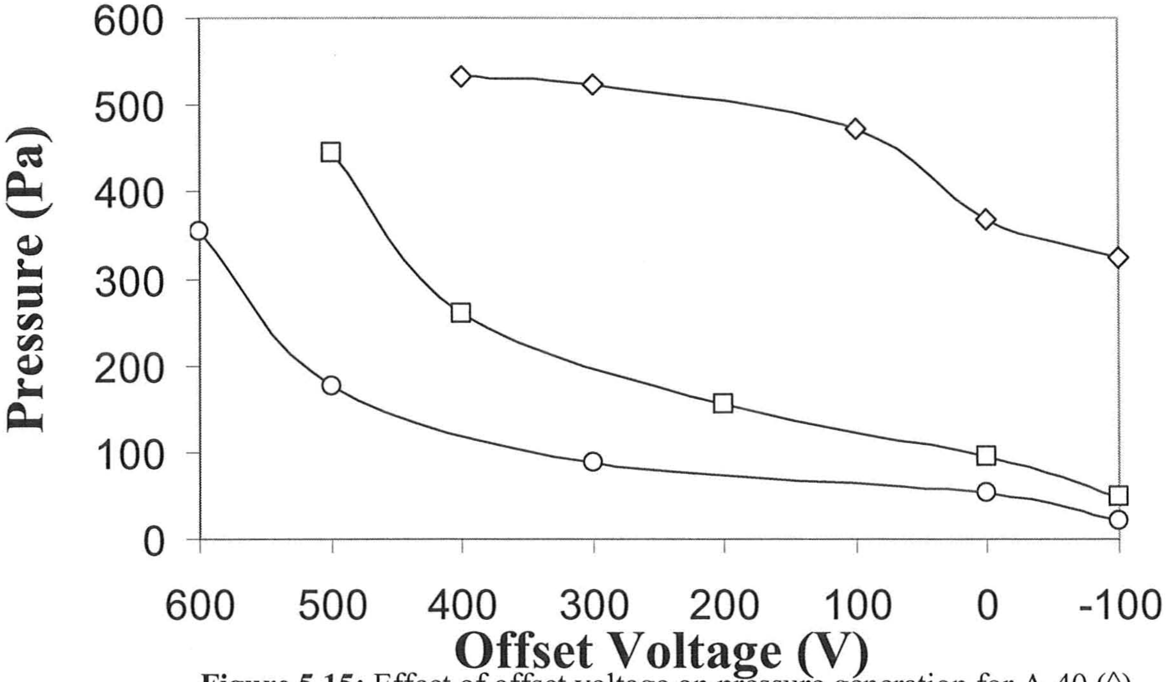

Figure 5.15: Effect of offset voltage on pressure generation for A-40 (◊), A-80 (□), and A-120 (○)

The decline in I_{eff}, I_{min}, and I_{max} is due to the decrease in the number of charged species, as less HFE-7100 molecules are ionized as a result of the effective voltage being reduced. There is also a fall in the pressure generation as the electric field strength is less lowered, which results in a lower electrophoretic force. However, there is more stability that is seen with applying lower offset voltages as ΔI approaches zero (figure 5.16 (d)). This could be the result of the enhancement in unipolar charged species existing in the fluid as less charge injection would occur at the electrode to create ionized HFE-7100 molecules, while Ferrocene will transform into Ferrocenium at lower potentials.

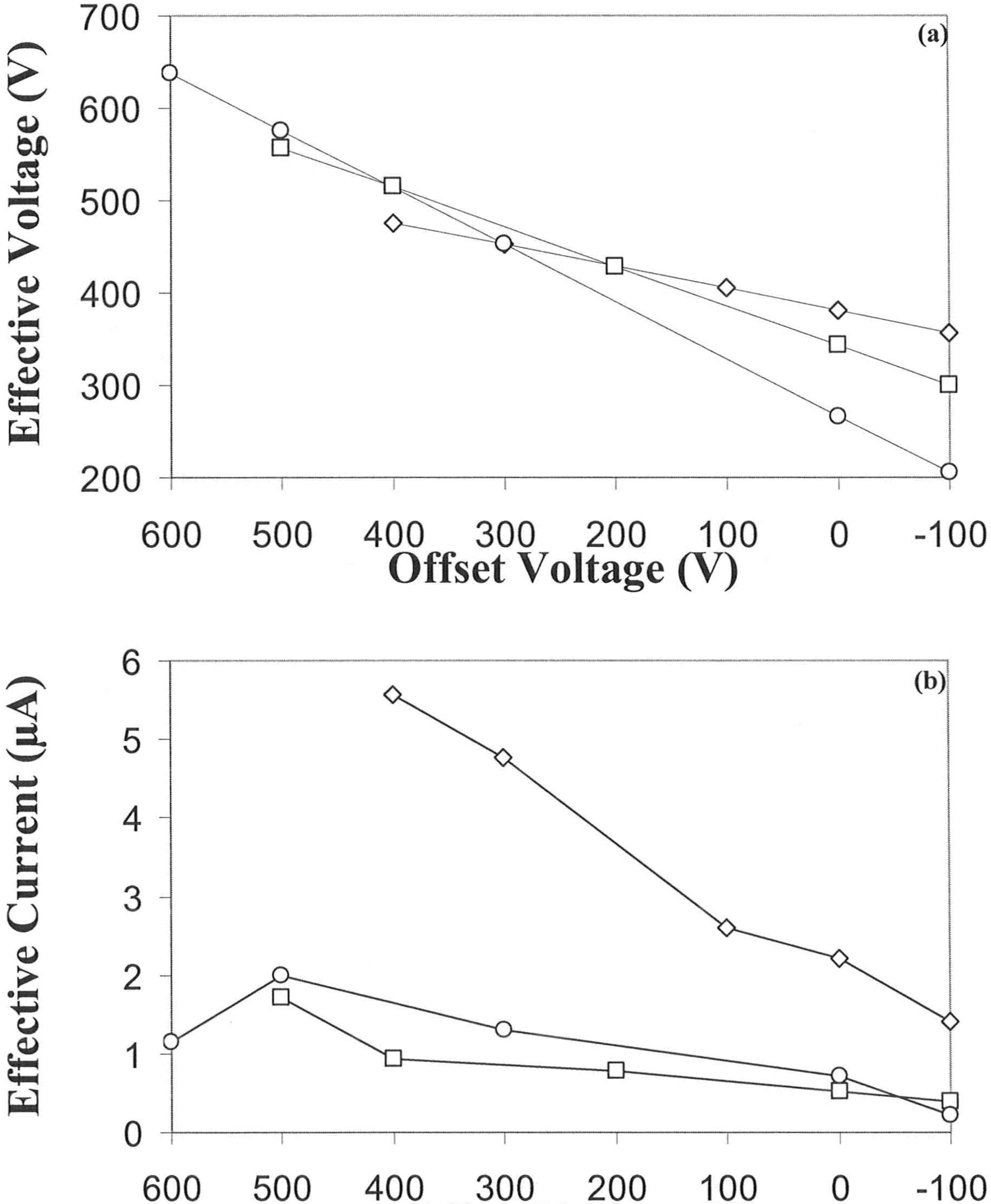
(a)
Effective Voltage (V)
700
600
500
400
300
200
600
500
400
300
200
100
0
-100
Offset Voltage (V)
(b)
Effective Current (μA)
6
5
4
3
2
1
0
600
500
400
300
200
100
0
-100
Offset Voltage (V)

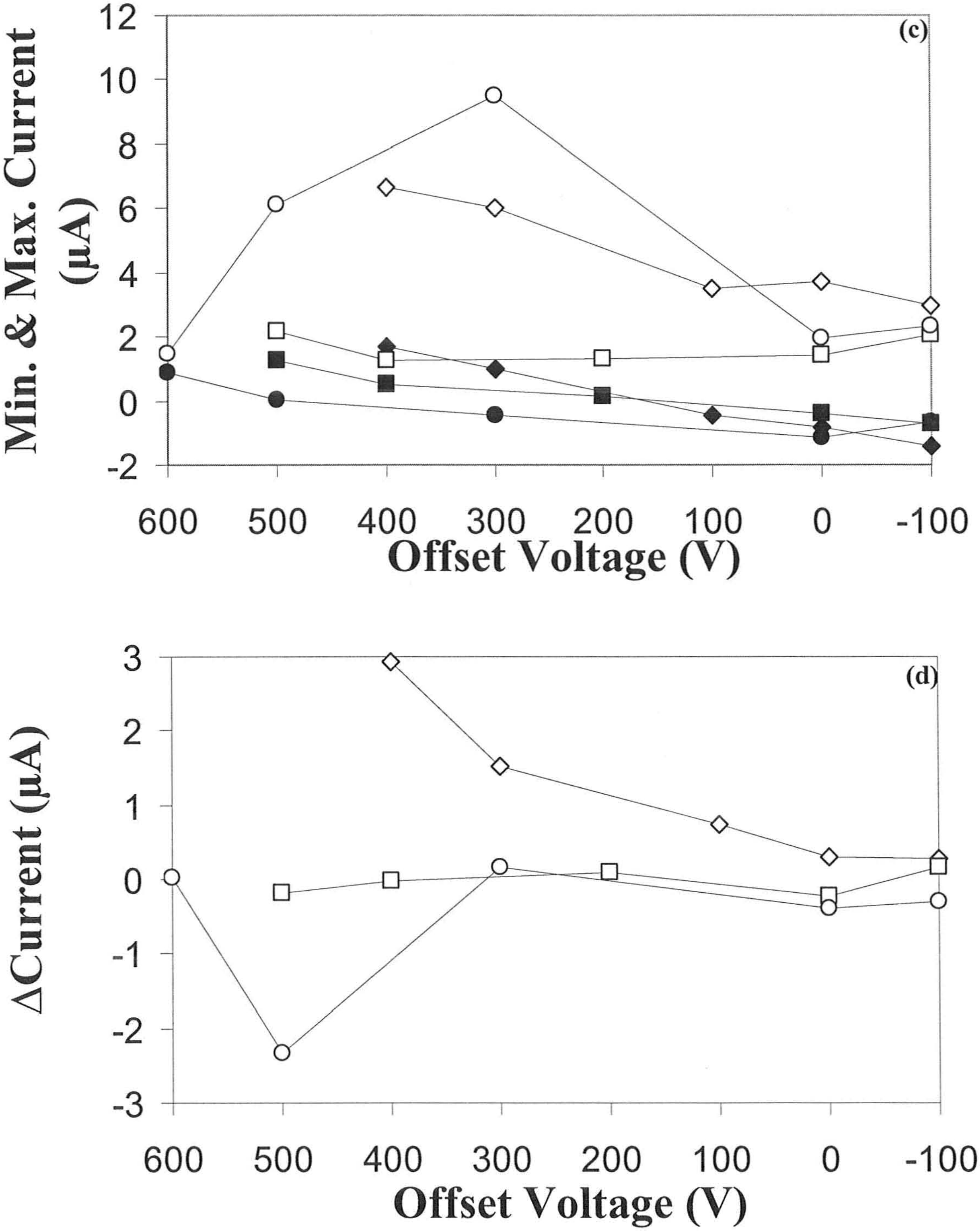

Figure 5.16: Effect of Offset Voltage on (a) Effective Voltage, (b) I $_{eff}$, (c) I_{min} (filled) and I_{max} (open), and (d) ΔI for A-40 (◊), A-80(□), and A-120 (○).

For A-120 a rise in I_{eff} was observed when changing the offset voltage from 600V to 500V and 300V (figure 5.16 (b)). This can be due to high I_{max} values of 6.11μA and 9.52 μA that was obtained for 500V and 300V at the interim period of applying the pulse voltage (figure 5.16(c)). However, from figure 5.16 (d) it can be concluded that there is more stability that is achieved with lowering the offset voltage as ΔI becomes closer to zero.

This section analyzes the effect of varying the high voltage with a fixed offset voltage of 500V and 600V for pump configurations A-80, and A-120. The test are performed for the duty cycles that were used in previous test as they provided optimum pressure heads, and the pulse repetition rate was set at 5Hz. The tests with A-40 resulted in break down when the amplitude between the high and offset voltage was 300V peak to peak. Therefore the test data for this configuration was inconclusive and are not presented here. Increasing the high voltage increases the pressure generation till it reaches an optimum level and then decrease with a further increase (figure 5.17). Increasing the high voltage causes the effective voltage to rise (figure 5.18 (a)). A maximum pressure of 3512 Pa and 2113 Pa was achieved for A-80 and A-120 when the voltage amplitude was 300V peak to peak. An optimum I_{eff} of 62.5 μA was achieved when the high voltage was set at 800V for A-80 while for A-120 6 μA was obtained at 900V (figure 5.18 (b)). This is due to rapidly increasing current amplitude variation, which as a result leads to an optimum I_{max} of 0.26 mA for A-80 and 8.52 μA for A-120 to be obtained (figure 5.18(c)).

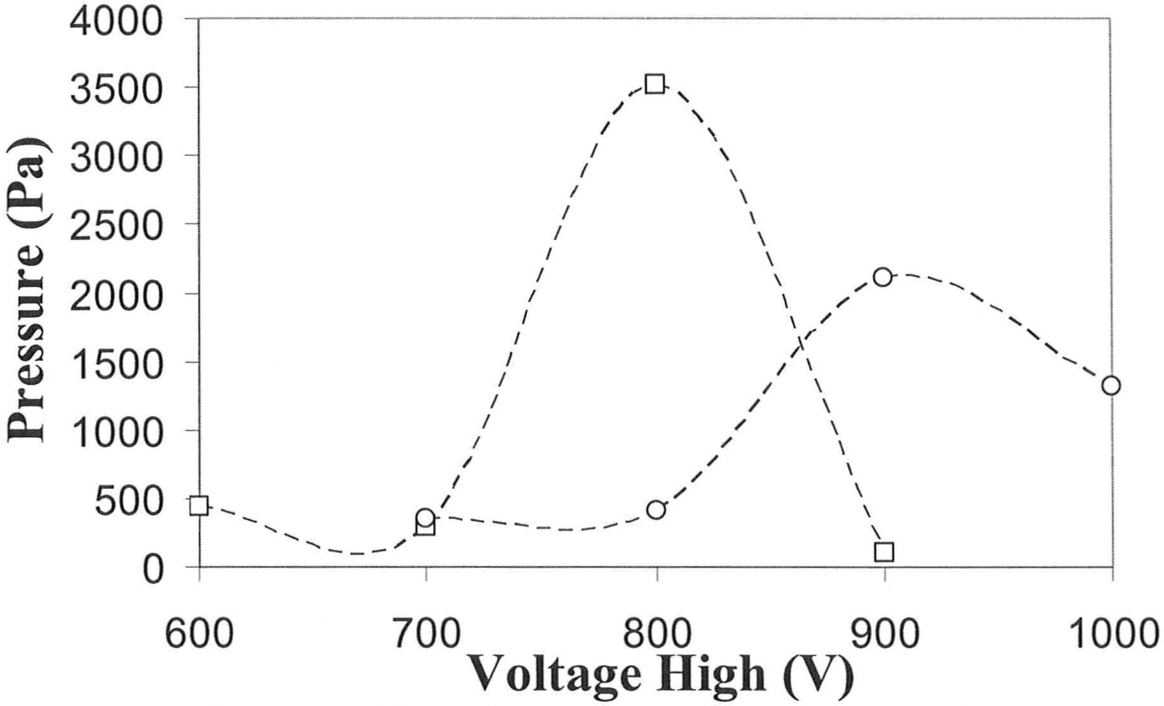

Figure 5.17: Effect of high voltage on the pressure generation for A-80 (□), and A-120 (○).

However, instabilities observed in the current when the voltage amplitude is increased from 300V peak to peak. The high current that is achieved begins to decay which results in a drop in the pressure generation. Figure 5.18 (d) shows the I_{rms} that is calculated for the different high voltage. The I_{rms} represents the deviation in the current signal from the I_{eff} that is calculated. When I_{eff} of 62.5 μA is obtained for A-80, the corresponding I_{rms} was 58 μA and for A-120 for I_{eff} of 6 μA it was 1.6 μA. The rapidly changing potential for the set pulse repetition rate encourages charge injection from the electrode, increasing the presence of bipolar charged species.

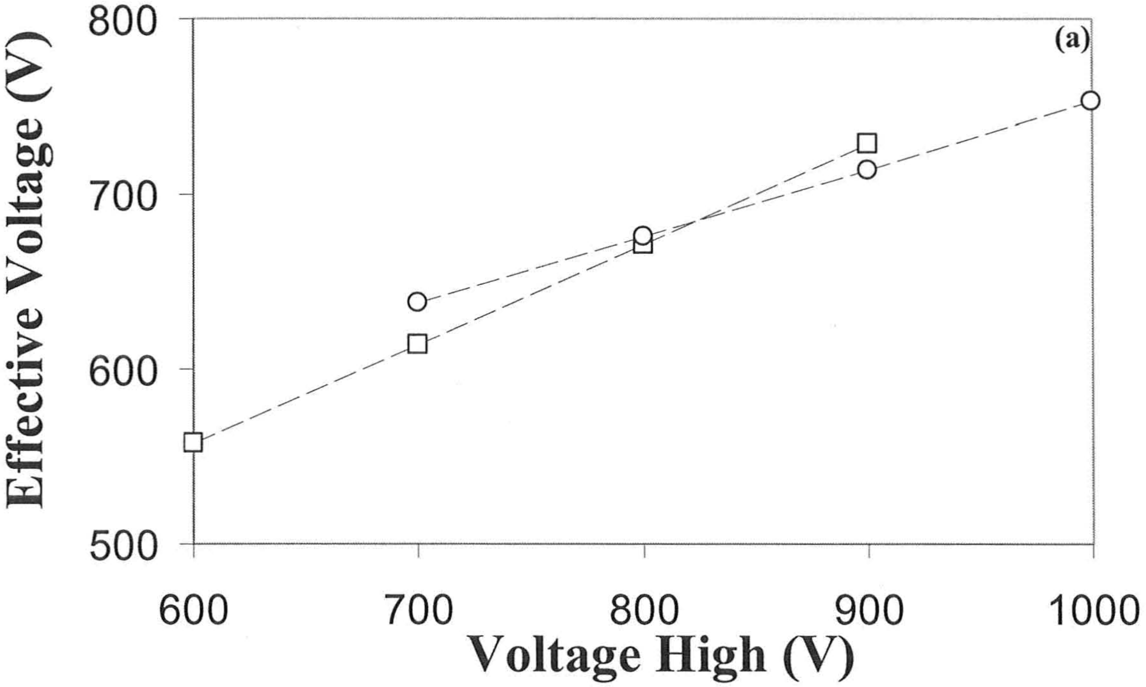
(a)
Effective Voltage (V)
800
700
600
500
600
700
800
900
1000
Voltage High (V)

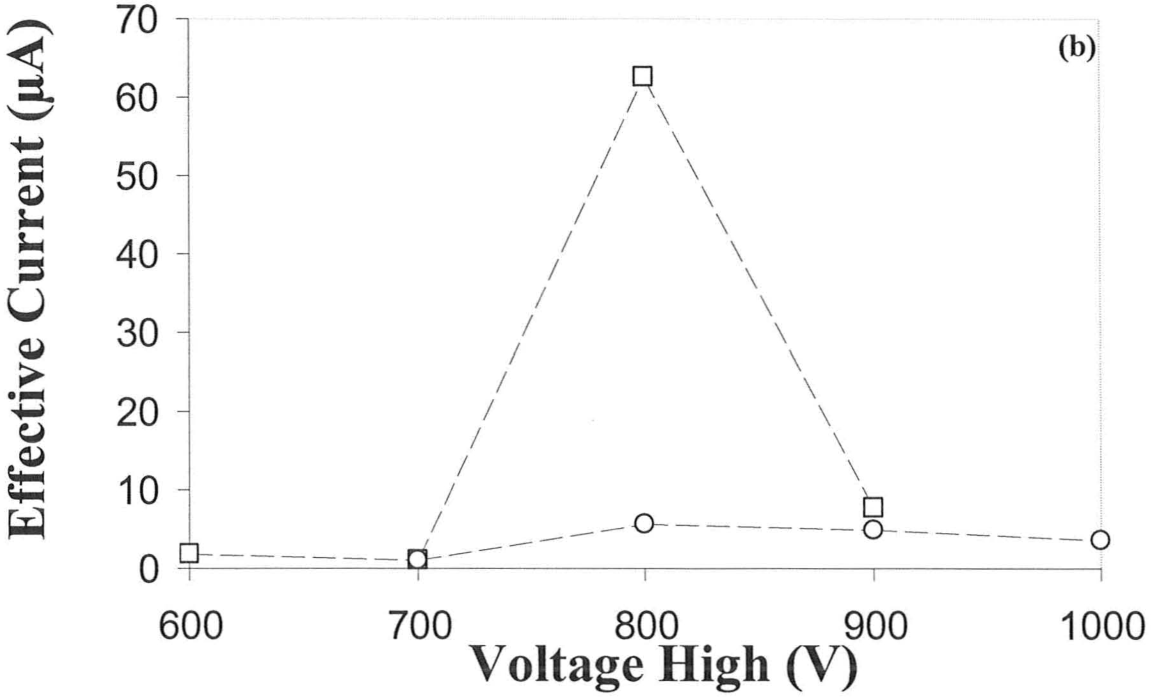
(b)
Effective Current (μA)
70
60
50
40
30
20
10
0
600
700
800
900
1000
Voltage High (V)

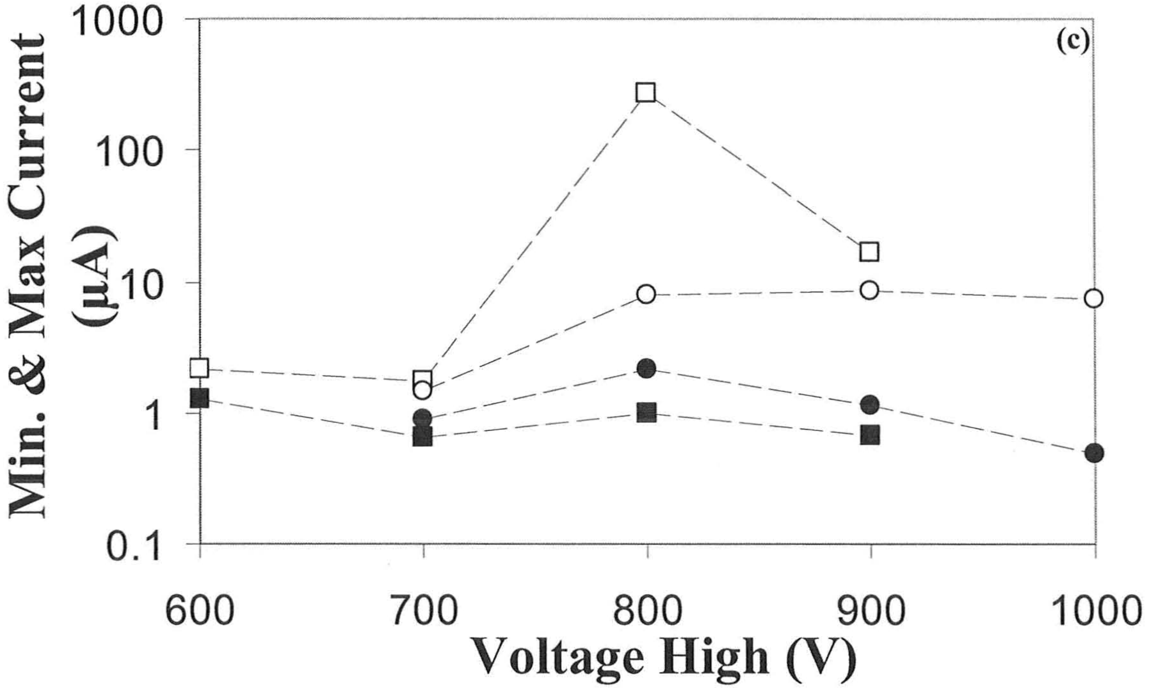

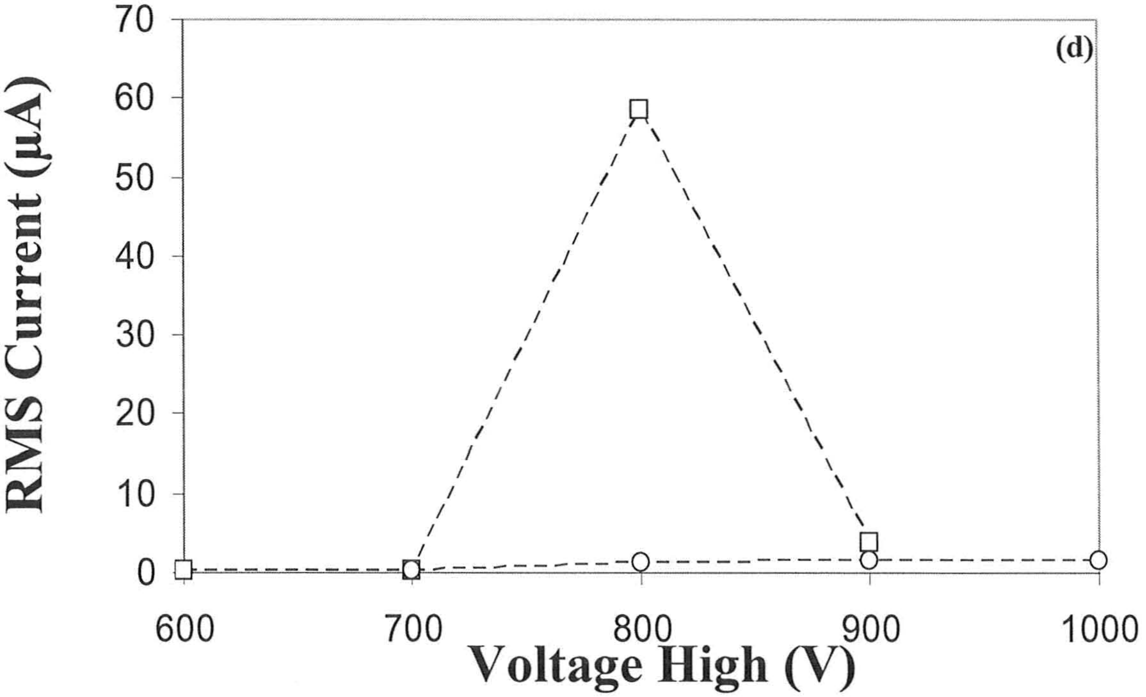

Figure 5.18: Effect of High Voltage on (a) Effective voltage, (b) I_{eff}, (c) I_{min} (filled), I_{max} (open), and (d) I_{rms} for A-80(□), and A-120 (○).

This enhanced presence increases the current initially but then a decline is observed due to charge migration occurring in opposing directions. Comparing the 400V DC case to the 500V to 800V pulse voltage for A-80, it can be observed that the time taken for the current to drop from the peak value is around 300 seconds. Therefore, from both experiments it can be deduced that elapsed time for ionized HFE-7100 molecules to be established and migrate is approximately 300 seconds. For A-120 the decline in the peak current occurs around 500 seconds for a pulse voltage of 600V to 900V. This is due to the larger inter-electrode spacing which results in a longer migration time.

A 12 hour test was performed with A-80 with 1%, 2%, and 5% (by weight) concentration of Ferrocene to test the stability of the pump. The applied pulse waveform was 700V for the high voltage, 600V for the offset, 50% duty cycle, and a pulse repetition rate of 0.01 Hz. This was selected due to the limitation of the sampling capacity of the data acquisition system and the duration of the test. The pressure was measured at the beginning and the end of the test. For 1% concentration the pressure at the beginning and the end of the test was found to be 100 Pa, while for 2 % concentration this was initially 370 Pa and then declined to 98.72 Pa. The 5% concentration also showed a pressure initially of 278 Pa and at the completion of the test cycle no significant pressure could be recorded. Figure 5.19 shows the effective current calculated for the each test. It can be seen that 1% concentration shows a steady current over the entire test while 2%, and 5% show a high current initially and then begin to decline.

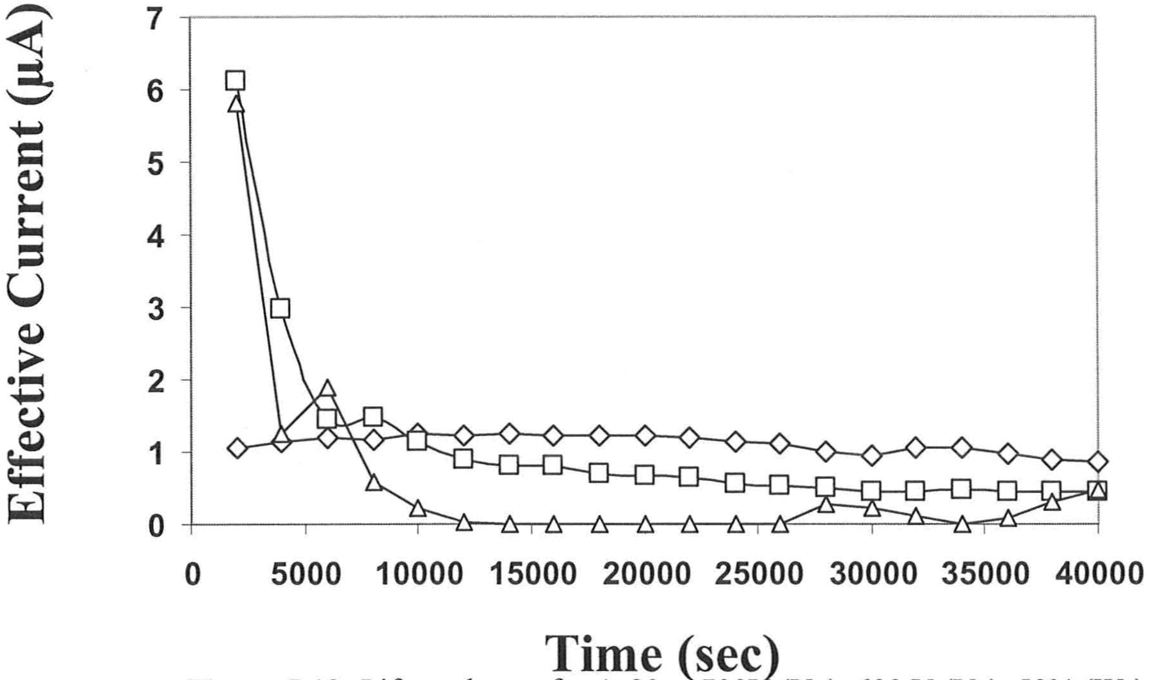

Figure 5.19: Life cycle test for A-80 at 700V (V_H), 600 V (V_L), 50% (W_p), 0.01 Hz (f), for 1% (◊), 2%(□), 5% (Δ)

This could be attributed to bubble generation as evidenced by the bubbles trapped inside the microchannel. Bubble generation can occur due to liquid decomposition through joule heating. Since joule heating is function of the applied potential, current and time, the high I_{eff} that is achieved in the initial periods of the test would accelerate the decomposition. Also since static pressure head is being measured there is no circulation of new fluid, therefore the same volume is exposed to the electric field, enhancing the joule heating effect. Another reason for the trend could be loss of volume of fluid due to evaporation at the liquid-air interface, as HFE-7100 has low evaporating temperature. The pump was also used prior to this test therefore there would be some electrode deterioration associated with these tests. However, employing HFE-Ferrocene and applying pulse voltage proves to enhance the durability of the pump unlike in previous works where the pump showed degradation in performance after 4 hours (Benetis, 2005). The A-80 pump was used for an aggregate of 104 hours after which no measurable pressure head could be observed and the current signal showed significant decay.

5.4 Summary

In this chapter the effect of doping pure HFE-7100 with Ferrocene on the performance of EHD micropumps is investigated. In addition, the effect of pulse voltage on the pump performance is also investigated using 1% concentration of Ferrocene by weight. The effect of the different parameters of the pulse voltage, such as voltage amplitude, duty cycle, and pulse repetition rate, on the pump performance was studied. The pump electrode geometry that was selected for this test was planar asymmetric with inter-electrode spacing of 40, 80, and 120 microns. The pressure generation increased with an increase in the pulse repetition rate. For A-40 80% duty cycle gave the highest pressure, while for A-80 and A-120 the optimum duty cycle was 60% and 40%. Reducing the offset voltage results in a lower pressure generation, and increasing the high voltage so that amplitude is 300V peak to peak gives optimum pressure. The effect of HFE-Ferrocene and pulsing on the stability of the pumps is also investigated for 1%, 2%, and 5% concentration for A-80.

Chapter 6: Conclusions and Recommendations

6.1 Introduction

This chapter summarizes the conclusions of this research. The rationale, and obstacles faced are presented, along with the results. The investigation dealt with developing a numerical model that incorporates a model for the charge injection process at the electrode, and experimentally investigating the use of dopants and pulse voltage on the pumping performance. This chapter concludes by providing recommendations in order to develop a better understanding of using dopants and pulse voltage, as well as developing the numerical model.

6.2 Summary of Results and Conclusion

The investigation can be categorized into three primary sections. The first was to develop a numerical model for EHD micropumps. Two problems in modeling the EHD mechanism has been faced in the past. The first is that the models are experimentally dependant and secondly since the charge injection process is not well understood, it is assumed to be uniform at the electrodes (Darabi and Rhodes 2006). The charge injection, however, is known to be dependent on the electric field and is generally found to be non-linear at the electrodes. The experimental work of Kazemi (2009a) was used to develop the model initially, and also for validation. Four different experimental configurations were used which were comprised of inter-electrode spacing of 80 and 120 microns with planar symmetric and asymmetric planar electrodes. Parametric studies were also carried out on the channel height and the multi-stage spacing. A summary of the numerical model are as follows:

- The charge boundary condition at the emitter was determined through the experimental current and the electric field. An E^2, E^3, and ∇E relation was used to develop the charge profile at the emitter that is coherent to the electric field distribution. When the back pressure generated from the model was compared to that from the experiment it was found that ∇E gave the best approximation for the planar symmetric configuration. For the asymmetric configuration the pressure estimated was lower; however, ∇E gave the closet prediction to the trend that is observed.

- A relation was derived to predict the local charge distribution at the electrode. This is based on both the magnitude and gradient of the electric field. The relation then was used to derive the charge for the different parametric configuration.

- From the parametric study it was found that reducing the channel height causes a reduction in flow rate but increases the pressure head. Increasing the multi-stage spacing causes a reduction in the pressure but an increase in the flow rate. This is because number of electrode stages is reduced to accommodate the pump in the same spatial confinement. However the flow rate is improved as the adverse interaction between the neighboring stages is reduced.

The second part of the research was to experimentally investigate the effect of HFE-7100 doped with a conductive agent on the pump performance. Asymmetric planar configurations were used with inter-electrode spacing of 40, 80, and 120 microns. The electrodes were microfabricated through photolithography and wet-etching techniques. The channel was developed by curing PDMS over moulds of channels created through SU-8 100 photoresist. The channel was integrated to the electrodes by employing plasma oxidization, and micro-contact printing in order to ensure a good seal. Previously it has been reported that liquid degradation plays a substantial role in the durability and repeatability in performance of the EHD micropump (Benetis 2005). This could be due to electrochemical reactions. High electric fields which are needed for the charge injection process, also cause the erosion of the electrodes. Adding a conductive agent would provide stability to the liquid and slow the erosion of the electrodes as the presence of charges will be dependent on the conductive particles. Of the available conductive agents it was found that Ferrocene was the only material that successfully dissolved into HFE-

7100 homogeously. Ferrocene was tested at 1% concentration of HFE-7100 by weight. HFE-Ferrocene provided similar performance seen in the work of Kazemi (2009a) but at lower voltages which are below the corona onset. The reason for this is that Ferroncene undergoes a redox reaction and becomes ionized (Ferrocenium) to create the ion-drag effect, instead of charge injection due to a corona onset. At higher voltages it was difficult to sustain the current. This is likely because at high potential, charge injection takes place which results in two types of charged species being present in the fluid domain with opposing polarities. This results in a decrease in the net current and pressure head.

The third part was to investigate the use of a pulse voltage on the pump performance. The pulse voltage parameters were investigated in terms of pulse repetition rate, duty cycle, high voltage, and the voltage offset. Finally the stability of the pump was tested with 1%, 2%, and 5% concentration of Ferrocene by weight for up to 12 hours. The results for this study are summarized below:

- At low pulse repetition rate it was found that the pressure generation varied with time. This is due to the response of the system, as the pressure head adjusts to change in potential. However, at faster pulse repetition rate the applied potential is changed rapidly so that the system pressure time constant can not adjust and pressure is sustained

- There is an optimum duty cycle to obtain maximum pressure which dependant on the inter electrode spacing. Increasing the duty cycle encourages the migration of charged species (Zaharaff and Yuan, 2002; Li, 2005). However, increasing the duty cycle also enhances the presence of bipolar charges as high voltage is for a predominantly larger duration. This causes a reduction in pressure generation as the duty cycle is increased.

- Reducing the offset voltage causes a reduction in pressure as the effective voltage and current is decreased. This is due to a reduction of charge species being present in the fluid domain as the effective voltage becomes lower than the potential required for corona onset. However, lowering the offset voltage results in more stable current as the Ferrocenium molecules provide unipolar charges to be present to generate the eletrophoretic force.

- An improvement of pressure was seen with an increase in the high voltage. A optimum pressure was achieved when the amplitude was 300V peak to peak. A pressure of 3512 Pa, and 2400 Pa was generated for A-80 and A-120. However, with large amplitudes it is difficult to sustain the current, as the rapidly changing high-potentials enhances charge injection from the electrodes, resulting in both ionized HFE-7100 and Ferrocenium molecules being present.

- Stability test of HFE-Ferrocene was tested with 1%, 2%, and 5% concentration by weight with A-80, for up to 12 hours. It was found that 1% concentration offered the most sustained result in terms of pressure and current. The 2%, and 5% concentration showed high pressures and current initially, but this degraded very quickly.

6.3 Recommendations

The recommendations for future work are based on addressing some of the problems encountered, and also to improve on the current work:

- In the numerical model the electric field is coupled to the fluid and charge equations in a one-way coupling technique. This is perhaps a reason for not resolving the asymmetric electric fields in the model. Simulations need to be performed by incorporating the convective term in the charge conservation

- In order resolve evaporation issues seen with HFE-7100, different dielectric fluids can be used that have higher evaporation temperatures. Also a closed loop system should be used to test with HFE-Ferrocene to preserve the volume of fluid present at the start of each test.

- Investigate the use of nanoparticles such as Carbon, and Nickel by using techniques to induce suspension.

- Testing HFE-Ferrocene with other electrode geometries, such as saw-tooth, 3D micropillars, both with DC and pulse voltage, to determine that the same enhancement in the performance can be obtained with such pump configurations.

- Determining whether high pressures that were achieved using pulse voltage can be sustained, by using low amplitude voltage with higher offset, or faster pulse repetition rates

- Applying other waveform voltages. For example the use of sine, triangular, and sawtooth waveform on the effect on the current and pressure generation.

References

Ahn, S. H., and Kim, Y.-K..,"Fabrication and experiment of a planar micro ion drag pump." Sensors and actuators A (physical), A70(1-2):1-5, 1998.

Asano, K. and Yatsuzuka, K." Fundamental study of EHD pump with needle-cylinder electrodes." Proceedings of the 68th annual conference on electrical insulation and dielectric phenomena,1999.

Atten, P., Seyed-Yagoobi J., "Electrohydrodynamically induced dielectric liquid flow through pure conduction in point/plane geometry." IEEE International Conference on Conduction and Breakdown in Dielectric Liquids, ICDL :231-4,1999.

Becker, H., Hanz, M. , Microsystem technology in chemistry and life science, Springer,1997.

Benetis V., "Experimental and computational investigation of planar ion drag micropump geometrical design parameters",Doctor of Philosophy, University of Maryland, 2005.

Bockris, J. O., Reddy, A. K. N., Modern Electrochemistry Vol. 1, Springer, 1998.

Bologa A. K., Kozhukhar I. A., Malakhov A. V. ,and Balokhin V. L., "Electrohydrodynamic pump service life." Proceedings of the IEEE 11th international conference on conduction and breakdown in dielectric liquids , 1993.

Borkar S.," Design challenges and technology of scaling." Micro IEEE ,19(4):23-29, 1999

Castaneda J. A. and Seyed-Yagoobi J., "Electrohydrodynamic pumping of refrigerant 11." IEEE industry applications society annual meeting, 1992 p.

Cazes, J., and Ewing, G.W., Ewing's analytical instrumentation handbook. 3rd Ed. New York: Marcel Dekker, 2005.

Chang, J.S., Tsubone, H., Chun, Y.N., Berezin, A.A., Urashima, K.,." Mechanism of electrohydrodynamically induced flow in a wire-non-parallel plate electrode type gas pump." J. Electrostatics, 67(2-3):335-339, 2009.

Chang, J., Kelly, A.J., Crowley, J.M., Handbook of electrostatic processes. New York: M. Dekker, 1995.

Chattock, A. P., Walker W. E.. Philosophical Magazine (1):79, 1901.

Chen Chia-Ling, Dokmeci Mehmet R., Selvarasah Selvapraba, Chao Shih-Hsien, Khanicheh Azadeh and Mavroidis Constantinos. "An electrohydrodynamic micropump for on-chip fluid pumping on a flexible parylene substrate." 2nd IEEE international conference on Nano/Micro engineered and molecular systems, 2007.

Crowley, J.M., Wright, G.S., and Chato, J.C., "Selecting a working fluid to increase the efficiency and flow rate of an EHD pump." IEEE Trans Ind. Appl., 26(1):42-49,1990.

Darabi ,J.,and Rhodes C., "CFD modeling of an ion-drag micropump." Sensors and Actuators A (Physical) 127(1):94-103, 2006.

Darabi J., Rada M., Ohadi M., Lawler J., "Design, fabrication, and testing of an electrohydrodynamic ion-drag micropump." J. Microelectromech. Syst., 11(6):684-690, 2002.

Dernovskii, V., Stishkov, Y. K., Statuya, A. A., "Modelling of nonstationary EHD flows in a wire-plane electrode system." Surface Engineering and Applied Electrochemistry, 43(3):182-186,2007.

Felten, M., Geggier, P., Jager, M., and Duschl, C.," Controlling electrohydrodynamic pumping in microchannels through defined temperature fields." Phys. Fluids, 18(5),2006.

Feng,Y., and Seyed-Yagoobi, Y.," Understanding of electrohydrodynamics conduction pumping phenomenon" J. Phys. Fluids, 16:2432-2441, 2004.

Foroughi P., Benetis V., Ohadi M., Zhao Y., and Lawler J., "Design, testing and optimization of a micropump for cryogenic spot cooling applications." 21st annual IEE Semiconductor Thermal Measurement and Management Symposium, 2005.

Fowler RH. "The restored electron theory of metals and thermionic formulae." Royal Society Proceedings, 117(A778):549-552, 1928.

Fuhr, G., Hagedorn, R., Muller, T., Benecke, W., and Wagner B., "Microfabricated electrohydrodynamic (EHD) pumps for liquids of higher conductivity." J. Microelectromech. Syst., 1(3):141-146,1992.

Gerlach, T. and Wurmus, H., "Working principle and performance of the dynamic micropump." Sensors and actuators A (physical), A50(1-2):135-140, 1995.

Hardt S, Schonfeld F., Microfluidic technologies for miniaturized analysis systems, SpringerLink,. 2007.

Jeong, S. and Seyed-Yagoobi, J., "Experimental study of electrohydrodynamic pumping through conduction phenomenon." J. Electrostatics, 56(2):123-133, 2002.

Jiang , M. W. , Yitshak, Z., "Forced convection boiling in a microchannel heat sink." J. Microelectromech . Syst., 10(1):80-87, 2001.

Kazemi, P.Z., Selvaganapathy, P.R., and Ching, C.Y., "Effect of electrode asymmetry on performance of electrohydrodynamic micropumps." J. Microelectromech. Syst.,18(3):547-554,2009a.

Kazemi P.Z., Selvaganapathy, P.R., Ching, C.Y., "Electrohydrodynamic micropumps with asymmetric electrode geometries for microscale electronics cooling." IEEE Trans. Dielectric Electrical Insulation, 16(2): 483-488, 2009b.

Laser, D. and Santiago, J., "A review of micropumps." J. Micromech. Microengineering, 14(6):R35-64, 2004.

Li, J. L., "On the meniscus deformation when the pulsed voltage is applied." J. Electrostatics, (64): 44-52, 2006.

Müller, T., Arnold, W.M., Schnelle, T., Hagedorn R., Fuhr G.,and Zimmermann, U., "A traveling-wave micropump for aqueous solutions: Comparison of 1 g and μg results." J. Electrophoresis 14(1): 764-772, 1993

Malakhov A. V., "The effect of time factor upon the stability of output parameters of electrohydrodynamic converters." Proceedings of IEEE 13th international conference on dielectric liquids (ICDL'99),1999.

Melcher , J.R., Continuum electromechanics. Cambridge, Mass.: MIT Press, 1981.

Nguyen N, Micromixers : Fundamentals, design, and fabrication, Ebooks Corporation, 2008.

Olsen, S. A., and Tallmen, D. E.,"Voltammetry of ferrocene in subcritical and supercritical chlorodifluoromethane." Journal of Analytical Chemistry, 66(4): 503-509, 1994.

Pasechnik, L.P., and Ufatov, I.V., "Investigation of EHD flow based on a numerical solution of the navier-stokes equations." Journal of Engineering Physics, 56(2):148-152, 1989.

Pickard, W.F., "Ion drag pumping theory." Journal of Applied Physics, 34(2):246-250, 1963.

Raj, E., Lisik, Z., Langer, M., Tosik, G., and Wozny, J., "The numerical approach to analysis of microchannel cooling systems." 5th international conference on computational science, 2005.

Rapp, R., Schomburg, W. K., Maas, D., Schulz, J., and Stark, W., "LIGA micropump for liquid and gases." Sensors and Actuators A, 40:57-61, 1994.

Rayne, R. C., Neurotransmitter Methods, Humana Press, 1997.

Richter, A. and Sandmaier H., "An electrohydrodynamic micropump." Proceedings of IEEE micro electro mechanical systems: An investigation of micro structures, sensors, actuators, machines and robots, 1990.

Shrimpton, J., Charge Injection Systems: Physical Principle, Experimental and Theoretical Work, Springer, 2009.

Siegel, D.M., Innovation in maxwell's electromagnetic theory : Molecular vortices, displacement current, and light. Cambridge England: New York : Cambridge University Press,1991.

Stratton, J.A., Electromagnetic theory. McGraw-Hill book company,1941.

Stuetzer, O. M., "Ion drag pressure generation. " J. Appl. Phys., 30: 984-994, 1959.

Tsubone, H., Ueno, J., Komeili, B., Minami, S., Harvel, G.D., Urashima, K., Ching, C.Y., Chang, J.S.," Flow characteristics of DC wire-non-parallel plate electrohydrodynamic gas pumps." J. Electrostatics 66(1-2):115-21, 2008.

Vasilevich, A.E., and Rychkov Y.M, "Study of the operating regimes of a three-electrode electrohydrodynamic pump." Journal of Engineering Physics and Thermophysics, 79(3):625-8, 2006.

Woolley, A.T., Hadley, D., and Landre, P., "Functional integration of PCR amplification and capillary electrophoresis in a microfabricated DNA analysis device." Anal. Chem., 68:4081-4086, 1996.

Yamamoto, T., and Sparks, L.E., "Numerical simulation of three-dimensional tuft corona and electrohydrodynamics." IEEE Trans. Ind .Appl., 22(5):880-885, 1986.

Yang, J. M. W. , Huang ,Y.-L. , "The micro ion drag pump using indium-tin-oxide (ITO) electrodes to resist aging." Sensors and Actuators A (Physical), A111(1):118-122, 2004.

Yazdani M, and Seyed-Yagoobi, " J.. Numerical investigation of electrohydrodynamic-conduction pumping of liquid film in the presence of evaporation." Journal of Heat Transfer 131(1):1-8, 2009.

Yun , I.-J. C. , Bu , J.-U., Kim C.-J. , Yoon, E., "A surface-tension driven micropump for low-voltage and low-power operations." J. Microelectromech. Syst., 11(5):454-461, 2002.

Zaharoff, D. A., and Yuan, F., "Effect of pulse strength and pulse duration on plasmid DNA electromobility." Proceedings of IEEE 2nd joint EMBS/BMES conference, 2002.

Zanello, P., Inorganic electrochemistry : Theory, practice and application. Cambridge: Royal Society of Chemistry, 2003.

Zhao L, Adamiak, K., "EHD flow in air produced by electric corona discharge in pin–plate configuration." J. Electrostatics, 63:337-350,2004.

Appendix A

Microfabrication Process, Fluid preparation, and Mantainence of micropump.

Metal Deposition:

- Deposit 100 Å of Chromium
- Deposit 2400 Å of Gold

Electrode Patterning:

- Dry-rinse the substrate with Nitrogen to ensure no particulates are present on the substrate.
- Centre sample on spinner. Set the spin rate 4000 rpm for 30 second.
- Use syringe with filter to pour S1808 positive photoresist. Then start the spin.
- Place sample on hot plate at 110°C for 2 min
- Take sample and expose to UV light. Exposure time should be set in accordance to the lamp power and to provide 30 mJ/cm^2 of energy to initiate the cross-linking of the photoresist.
- Use 351 solution to develop the photoresist. Dilute in de-ionized (DI) water with a mixing ratio 1 part developer and 5 parts DI water. Developing time should be between 40-60 seconds. After 40 seconds check development continuously every 10 seconds under the microscope.
- Dip and then rinse in DI water for 5 minutes. Then dry-rinse with Nitrogen.
- Hard bake sample at 130°C for 2 minutes

- Etch Gold with Nickel-compatible Gold etchant by Sigma Aldrich. Etch time should be around 45-60 seconds. Check continuously for development under microscope. Dip and rinse with DI water. Then dry-rinse
- Etch Chromium with Sigma Aldrich Etchant. Etch rate (40 Å/s) is too fast for the layer of chromium deposited. Therefore dilute with DI water with mixing ratio of 1 part etchant and 4 part DI water. Etch time should be around 30-45 seconds.
- Dip and rinse with DI water for 5 minutes. Then dry-rinse with Nitrogen.
- Rinse with acetone. Then dip into beaker with acetone. Place beaker in ultra-sonic bath for 5 minutes. Then rinse with methanol and dip into beaker with methanol. Place in ultra-sonic bath for 5 minutes. Dip into DI water and then rinse for 5 minutes. Dry-rinse with Nitrogen.
- Dice glass to isolate the electrode patterns

Channel Mould:

- Dry-rinse silicon substrate with Nitrogen to ensure no particulates are present on the substrate.

- Place on spinner. Pour SU-8 100 positive photoresist of 3 ml in portion. Set spinner at 500 rpm for 10 seconds, to get a more even distribution of the photoresist. Then set spinner to 2500 rpm for 30 seconds. Ramp up speed by 400 rpm/sec.

- Pre-bake sample at 65°C for 10 minutes. Then soft bake at 95°C for 30 minutes, ramping up by 10^0C per minute.
- Expose sampe to UV light. Exposure time should be set according to lamp power and to achieve 600 mJ/cm^2.
- Post-bake sample at 65°C for 1 minute then 95°C for 10 minutes. Ramp temperature by 10°C per minute.
- Develop photoresist using Microchem Corp. SU-8 Developer. Approximate time to develop is 10 minutes.
- Check to see if photoresist is develop by rinsing with isopropanol. If white residue is present then place sample back into the developer solution. If no residue present then rinse with DI water then dry-rinse with nitrogen.
- Deposit paraleyne

Channel Fabrication:

- Pour into plastic beaker PDMS solution. 20 ml of elastomer and 2 ml curing agent. Stir solution for 5 minutes.
- Leave to rest for 5 minutes. Then place into vacuum chamber to degas for 15-30 minutes.
- Place channel mould in plastic petri dish. Make sure it is not close to the edges of the dish.

- Pour PDMS solution over the mould and the place over the hot plate at 65°C. The curing time required is about 1 hour.

Microchannel and Electrode Integration:

- Solder electrode base with copper wires
- Rinse electrode base with acetone. Then dip into beaker with acetone. Place the beaker in the ultra-sonic bath for 5 minutes
- Take sample and rinse with methanol. Dip into beaker with methanol. Again take the beaker into the ultra-sonic bath for 5 minutes
- Dip sample into DI water. Then rinse in DI water for 5 minutes
- Peel channel out of the channel mould and punch 1.5 mm hole using punching tool.
- Plasma oxidize the channel at 50 W for 20 minutes.
- Prepare PDMS glue and spin on silicon wafer 8000 rpm for 2 minutes. PDMS glue has a ratio of 1 part curing agent and 3 part elastomer.
- Gently press channel onto the PDMS glue. Place paper weight to enhance contact with surface.
- Plasma oxidize electrode surface at 50 W for 20 minutes.

- Remove PDMS channel from contact with glue. Apply to electrode surface. Make sure channel edge is aligned to electrode ends correctly. Also make sure pressure is being evenly applied to ensure no seepage of the glue.
- Heat sample at 80°C for 20 minutes. Then ramp temperature to 150°C.
- Pour PDMS glue around the perimeter of the channel. Allow glue to cure for about 2 minutes.
- Plasma oxidize sample and glass tubings at 50 W for 20 minutes.
- Insert tubings into the hole of the PDMS.
- Place sample on hot plate at 150°C for 5 minutes.
- Pour PDMS glue around the edges of the glass tubing.

Fluid Preparation:

- Take HFE-7100 in bottle and degas with Nitrogen for 1-2 minutes.
- Place HFE-7100 in mass-pan balance and weigh.
- According to weight place appropriate percentage of Ferrocene in plastic beaker.
- Pour HFE-7100 into plastic beaker and stir for 5 minutes.
- Pour HFE-Ferrocene into plastic bottle and place the bottle in ultra-sonic bath for 15 minutes.

- Use 0.45 μm filter to remove any undissolved solutes.

Cleaning Micropump:

- Place two plastic tubings in the inlet and outlet
- Attach syringe to one end of tubing and the other end into beaker with acetone.
- Apply suction and then hold with acetone in channel for about 5 minutes
- Discharge acetone and then repeat process with methanol.
- Discharge methanol and repeat process with IPA.
- Remove plastic tubings and place sample on hot plate at 70^0C for 5 hours.

Appendix B

Current vs. Time traces

A-40:

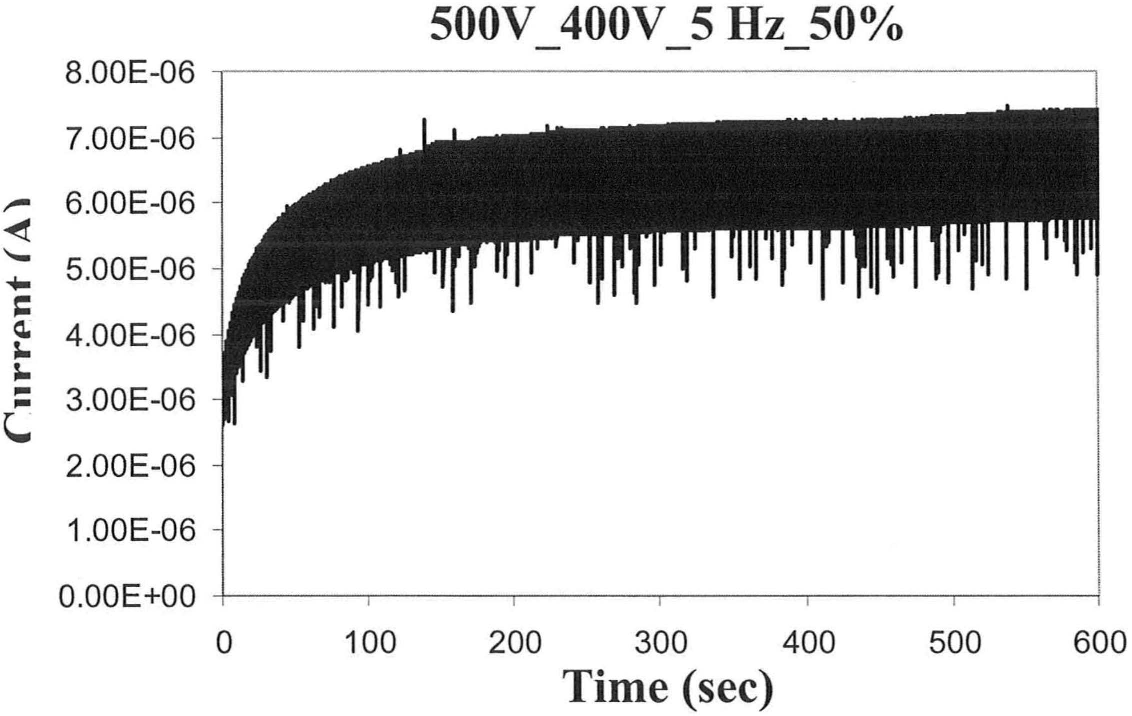

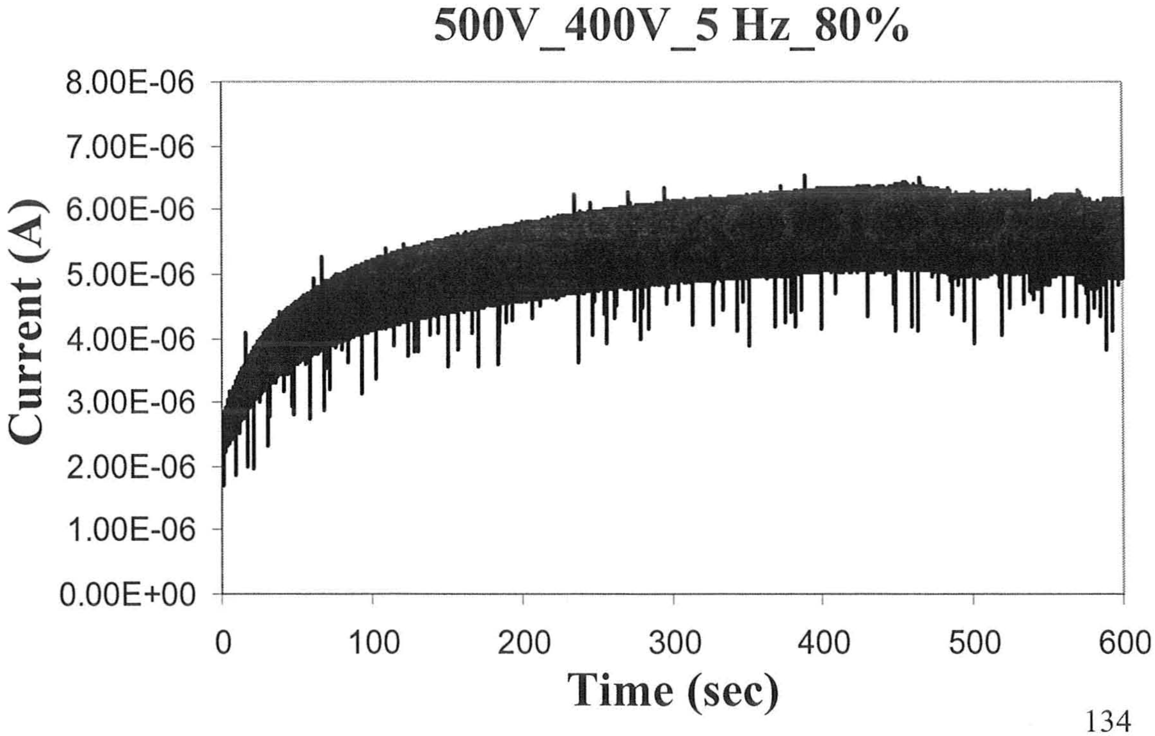

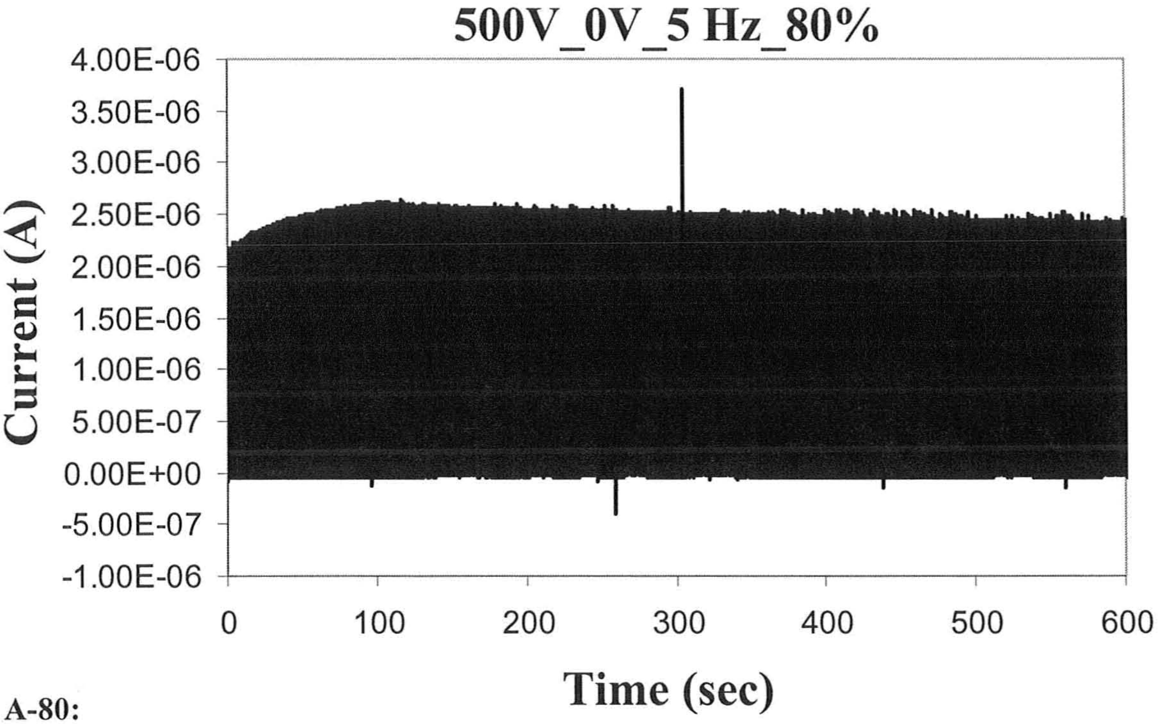
500V_0V_5 Hz_80%
Current (A)
4.00E-06
3.50E-06
3.00E-06
2.50E-06
2.00E-06
1.50E-06
1.00E-06
5.00E-07
0.00E+00
-5.00E-07
-1.00E-06
0
100
200
300
400
500
600
Time (sec)

A-80:

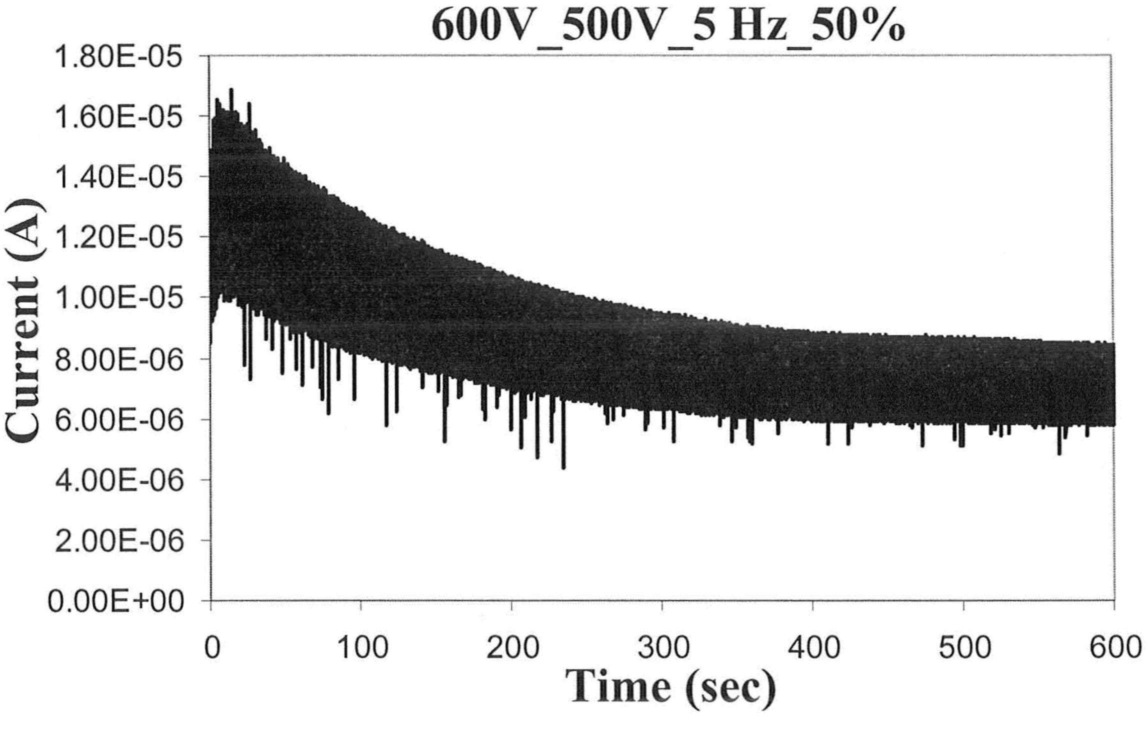
600V_500V_5 Hz_50%
Current (A)
1.80E-05
1.60E-05
1.40E-05
1.20E-05
1.00E-05
8.00E-06
6.00E-06
4.00E-06
2.00E-06
0.00E+00
0
100
200
300
400
500
600
Time (sec)

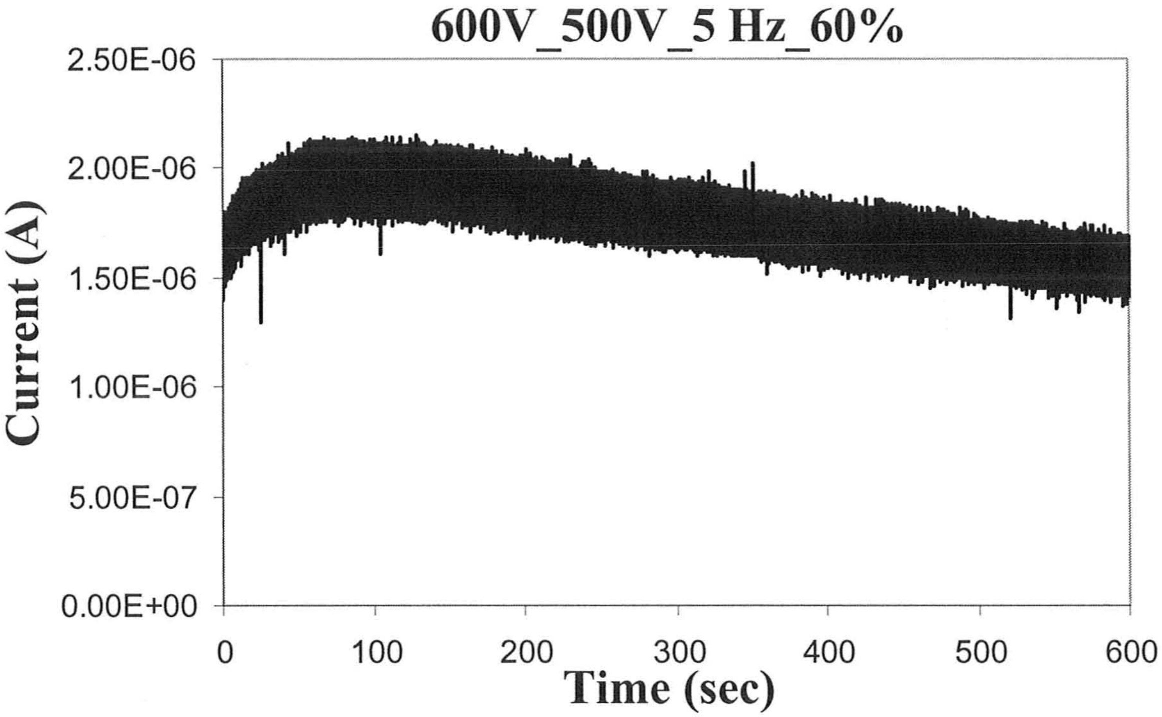
600V_500V_5 Hz_60%
Current (A)
2.50E-06
2.00E-06
1.50E-06
1.00E-06
5.00E-07
0.00E+00
0
100
200
300
400
500
600
Time (sec)

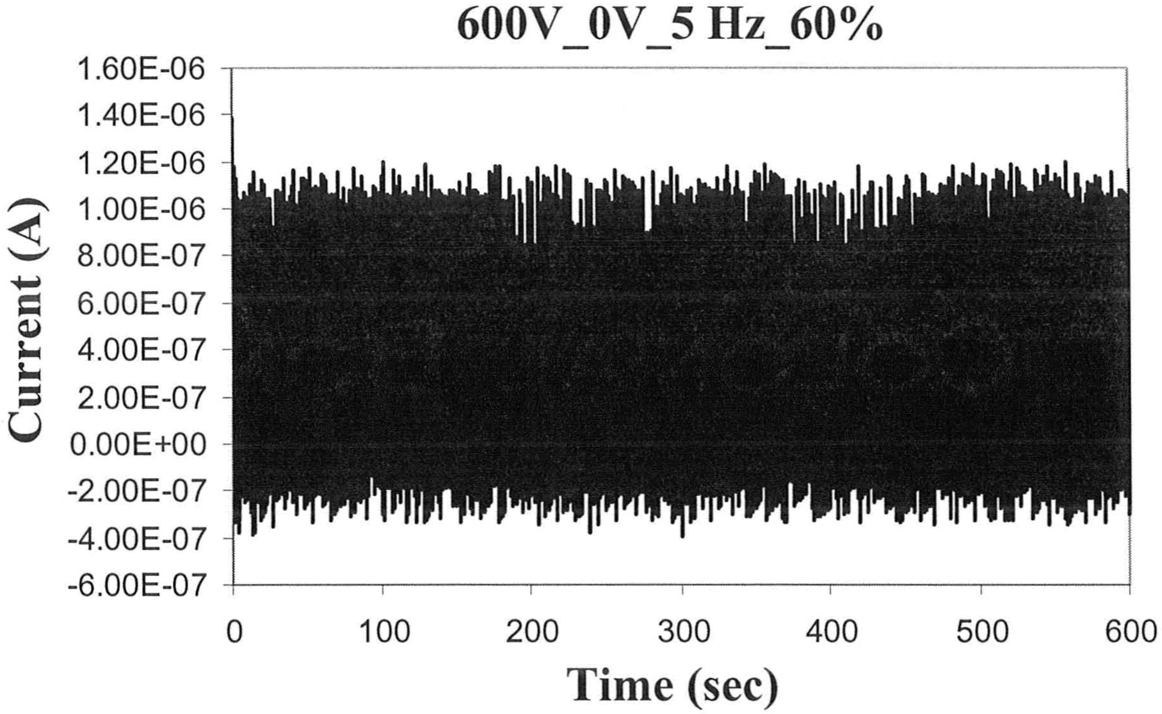
600V_0V_5 Hz_60%
Current (A)
1.60E-06
1.40E-06
1.20E-06
1.00E-06
8.00E-07
6.00E-07
4.00E-07
2.00E-07
0.00E+00
-2.00E-07
-4.00E-07
-6.00E-07
0
100
200
300
400
500
600
Time (sec)

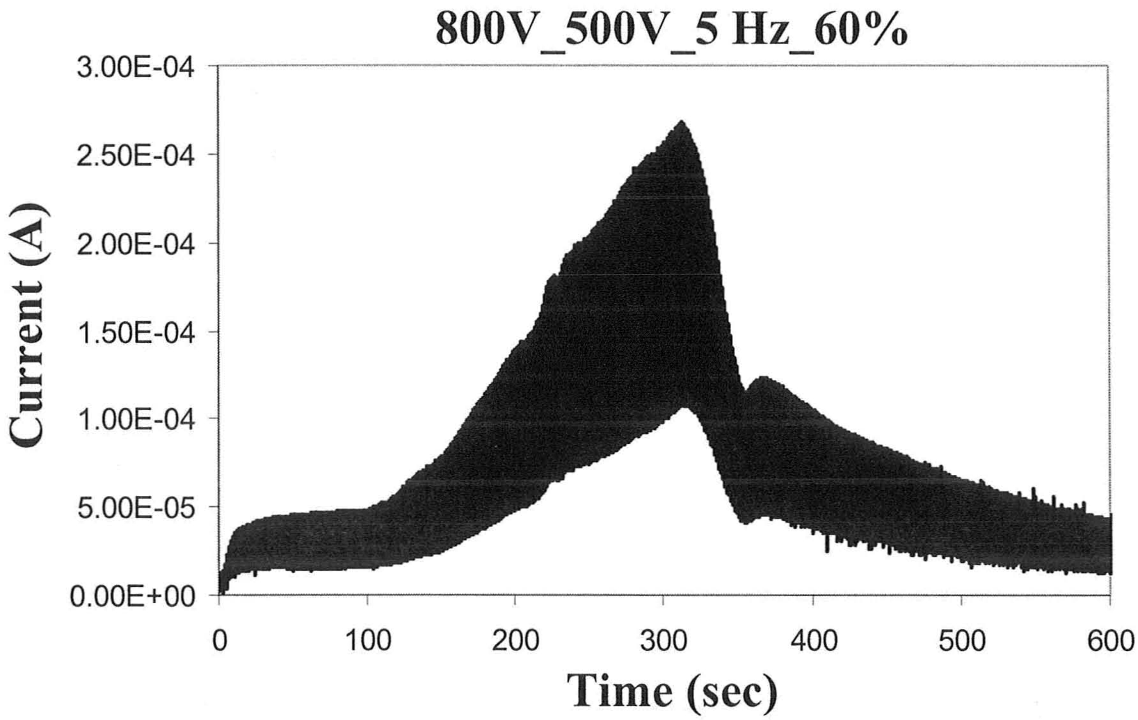
800V_500V_5 Hz_60%
3.00E-04
2.50E-04
2.00E-04
1.50E-04
1.00E-04
5.00E-05
0.00E+00
Current (A)
0
100
200
300
400
500
600
Time (sec)

A-120:

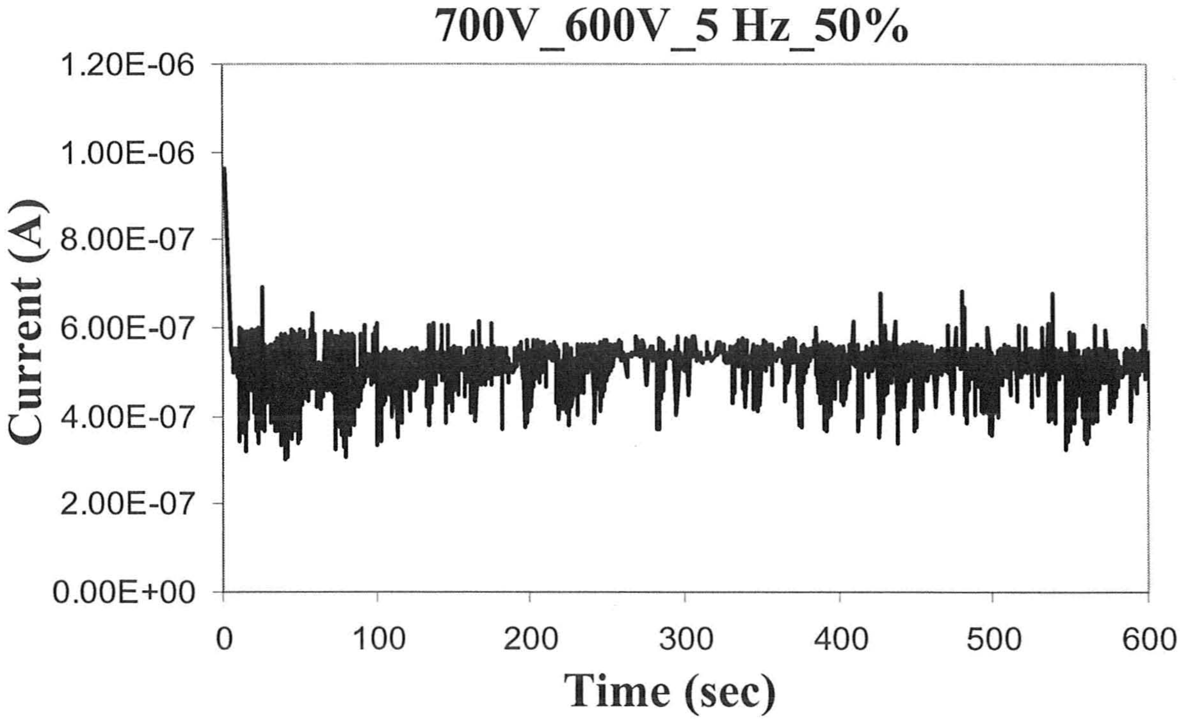
700V_600V_5 Hz_50%
1.20E-06
1.00E-06
8.00E-07
6.00E-07
4.00E-07
2.00E-07
0.00E+00
Current (A)
0
100
200
300
400
500
600
Time (sec)

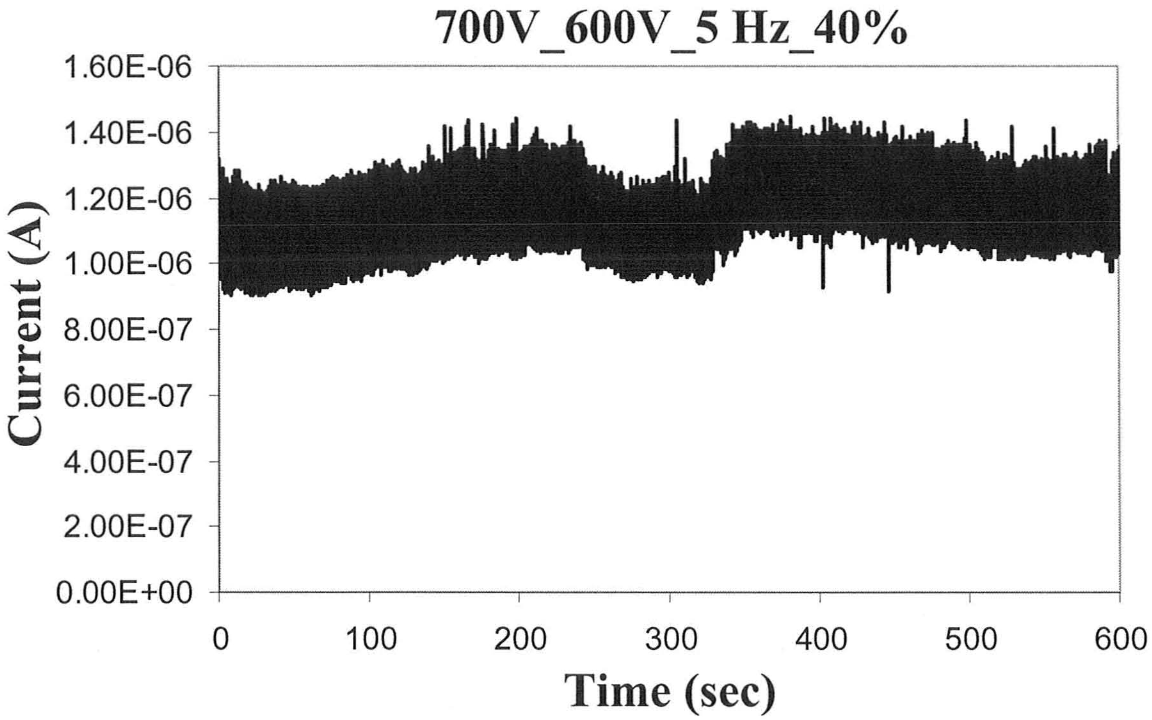
700V_600V_5 Hz_40%
Current (A)
1.60E-06
1.40E-06
1.20E-06
1.00E-06
8.00E-07
6.00E-07
4.00E-07
2.00E-07
0.00E+00
0
100
200
300
400
500
600
Time (sec)

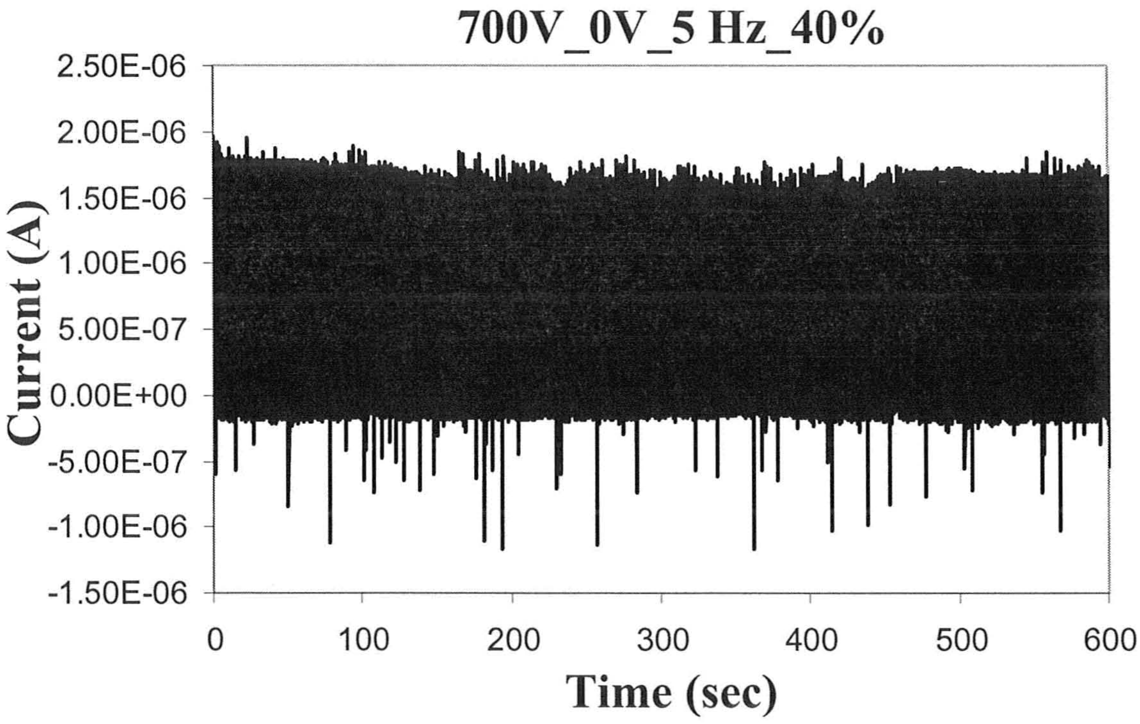
700V_0V_5 Hz_40%
Current (A)
2.50E-06
2.00E-06
1.50E-06
1.00E-06
5.00E-07
0.00E+00
-5.00E-07
-1.00E-06
-1.50E-06
0
100
200
300
400
500
600
Time (sec)

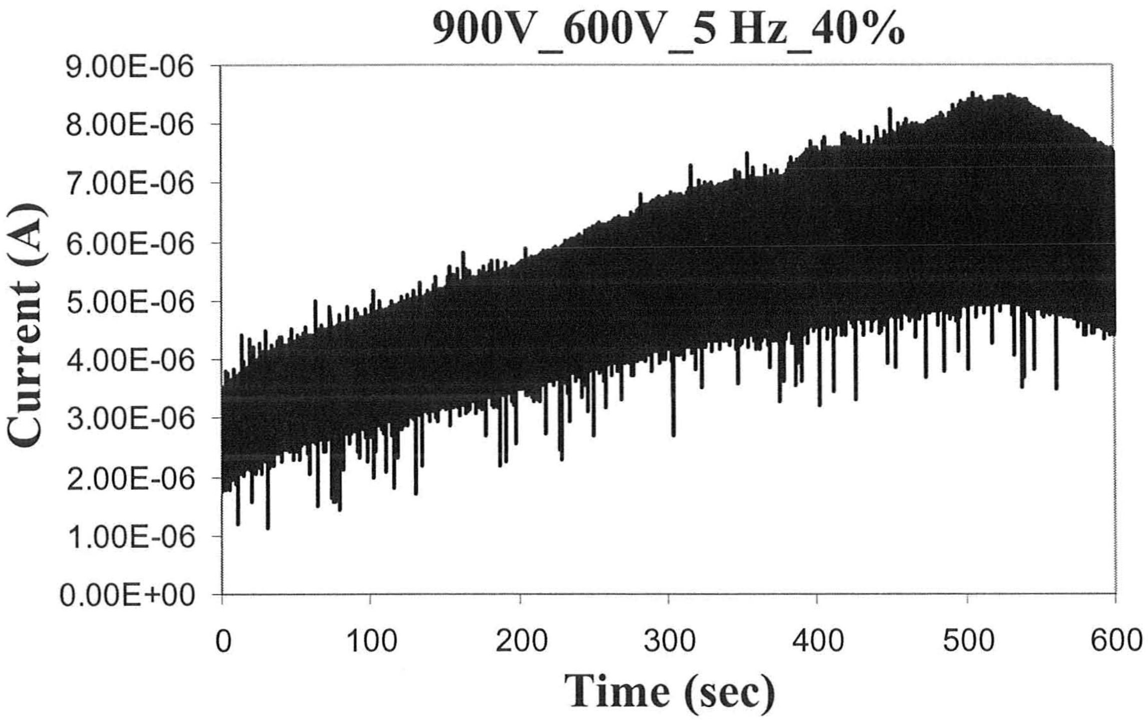
900V_600V_5 Hz_40%
Current (A)
9.00E-06
8.00E-06
7.00E-06
6.00E-06
5.00E-06
4.00E-06
3.00E-06
2.00E-06
1.00E-06
0.00E+00
0
100
200
300
400
500
600
Time (sec)